eXPRESS Polymer Letters Vol.5, No.9 (2011) 753
Available online at www.expresspolymlett.com
DOI: 10.3144/expresspolymlett.2011.73

Editorial corner – a personal view
Polymers to permeate lipid bilayer membranes

*C. Werner**

Leibniz Institute of Polymer Research Dresden, Max Bergmann Center of Biomaterials & Technische Universität Dresden, Center for Regenerative Therapies Dresden, Hohe Str. 06, 01069 Dresden, Germany

Polymers capable of entering cells across lipid bilayer membranes receive increasing attention in various different technological approaches.

Gene therapy, the insertion of genes into the cells of patients to fight diseases, holds great promise. However, safe and effective carrier structures to deliver DNA (desoxyribonucleic acid, the polymer that contains all the genetic instructions) into the cells still present a major challenge. Non-viral systems employ assemblies of DNA and cationic macromolecules. The polymers explored include degradable and non-degradable types, such as chitosan and poly(amidoamine) dendrimers, and are selected for targetability, cellular uptake and minimal toxicity. The primary purpose of introducing genes into cells is the expression of encoded proteins. In parallel to the ongoing related efforts to introduce genes, the direct delivery of proteins across the cell membranes has been investigated successfully for a variety of systems. Arginine-rich, cell-penetrating, peptide tags attached to various proteins have been shown to boost their membrane permeability. The combination of amino acids with cationic and hydrophobic side chains was reported to increase the efficacy of the peptide tags. Recently, this approach has even been applied successfully to cellular reprogramming, i.e., in the generation of human pluripotent stem cells via the delivery of a set of modified transcription factors.

Antimicrobial peptides, a range of naturally occurring and synthetically generated peptide structures, take this even further and not only disintegrate bacteria but also protozoa, fungi and viruses by disrupting their lipid bilayer membranes. The related peptides consist of 12 to 50 amino acids, including at least two – often more – cationic amino acids plus hydrophobic amino acids in varying amounts. Importantly, being effective against microorganisms, the peptides are compatible with tissue cells, facilitating their use in the protection of medical devices against microbial settlement and colonization without triggering microbial resistance mechanisms. These advantages motivate both the immobilization of cationic peptides onto polymeric surfaces as well as the incorporation of related antimicrobial motifs into synthetic polymer structures.

Despite all the recent progress, the targeted development of membrane-penetrating polymer structures requires a more detailed mechanistic understanding of the permeation process, and the required structural and environmental conditions. Joint theoretical and experimental efforts are emerging to resolve these issues in carefully selected model systems.

Prof. Dr. Carsten Werner
Member of International Advisory Board

*Corresponding author, e-mail: werner@ipfdd.de

eXPRESS Polymer Letters Vol.5, No.9 (2011) 754–765
Available online at www.expresspolymlett.com
DOI: 10.3144/expresspolymlett.2011.74

Effect of block composition on thermal properties and melt viscosity of poly[2-(dimethylamino)ethyl methacrylate], poly(ethylene oxide) and poly(propylene oxide) block co-polymers

*A. Vesterinen, S. Lipponen, J. Rich and J. Seppälä**

Aalto University School of Science and Technology, Polymer Technology Research Group, P.O. Box 16100, 00076 Aalto, Finland

Received 23 December 2010; accepted in revised form 1 March 2011

Abstract. To modify the rheological properties of certain commercial polymers, a set of block copolymers were synthesized through oxyanionic polymerization of 2-(dimethylamino)ethyl methacrylate to the chain ends of commercial pre-polymers, namely poly(ethylene oxide) (PEO), poly(ethylene oxide)-block-poly(propylene oxide)-block-poly(ethylene oxide) (PEO-PPO-PEO), and poly(propylene oxide) (PPO). The formed block copolymers were analysed with size exclusion chromatography and nuclear magnetic resonance spectroscopy in order to confirm block formation. Thermal characterization of the resulting polymers was done with differential scanning calorimetry. Thermal transition points were also confirmed with rotational rheometry, which was primarily used to measure melt strength properties of the resulting block co-polymers. It was observed that the synthesised poly[2-(dimethylamino)ethyl methacrylate]-block (PDM) affected slightly the thermal transition points of crystalline PEO-block but the influence was stronger on amorphous PPO-blocks. Frequency sweeps measured above the melting temperatures for the materials confirmed that the pre-polymers (PEO and PEO-PPO-PEO) behave as Newtonian fluids whereas polymers with a PDM block structure exhibit clear shear thinning behaviour. In addition, the PDM block increased the melt viscosity when compared with that one of the pre-polymer. As a final result, it became obvious that pre-polymers modified with PDM were in entangled form, in the melted state as well in the solidified form.

Keywords: *rheology, PDM, DSC, block-copolymer*

1. Introduction

Block co-polymers can have several properties that are not present in comparable statistical co-polymers, and interest in studying their properties has increased considerably during recent decade [1]. Block co-polymers can have, for example, the ability to form self-organized structures [2]. Especially co-polymers consisting of PDM (poly[2-(dimethylamino)ethyl methacrylate]), PEO (poly(ethylene oxide)), and/or PPO (poly(propylene oxide) blocks have found applications in the field of hydrophobizing paper [3] or other hydrophilic surfaces [4], strengthening agents for wood fibre networks [5, 6] and even some biomedical applications [2]. In addition, some special solution properties have been found for copolymers containing cationizable PDM block. E.g. at high pH PEO-b-PDM will aggregate at the temperature where the PDM sequence is totally deprotonated and sufficiently hydrophobic [7]. PDM can also easily be modified into a permanently cationic form by methylation of the tertiary amine group to form a quaternary amine [8, 9].

*Corresponding author, e-mail: jukka.seppala@tkk.fi

One convenient way to polymerize 2-(dimethylamino)ethyl methacrylate, and via that route to synthesize block copolymers containing PDM segments, is to use potassium alcoholate RO^-K^+ as an initiator [10]. This alcoholate synthesis was first introduced by Nagasaki *et al*. [11], and later it was called oxyanionic synthesis when further studies of the mechanism were done [12, 13]. Since then, numerous macroinitiators containing hydroxyl groups have been studied, among them PEO [14], PPO [15], poly(dimethyl siloxane) [16], short aliphatic carbon chains [17] and different combinations of these [14–20]. The oxyanionic method has also been successfully applied to polymerize some other methacrylates, like 2-(trialkylsiloxyethyl) methacrylate [21].

Relatively high concentrations of PEO, PPO, PDM, and their block copolymers can easily be dissolved in water, and their rheological characterization has mainly focused on solution properties [2, 7, 22]. In contrast to the solution properties, their thermomechanical properties have not been studied extensively. Rheological properties of PEO homopolymer have been studied in more detail [23, 24] and some crystallization studies of PEO-polystyrene (PS) block co-polymers have been performed with rheometry [25]. Still, the rheological properties of polymers are of interest, and other types of block co-polymers [26, 27], liquid crystalline polymers [28], and star polymers [29] have usually been analysed thoroughly. Rotational rheometry, often together with scattering techniques [30], has been used for studies on microphase separation [31], crystallinity [25], and order to disorder transitions of block co-polymers [32–36].

In this study a set of PEO, PPO and PEO-PPO-PEO macroinitiators was used to synthesize block polymers with PDM segments using oxyanionic synthesis. Materials were characterized with nuclear magnetic resonance (NMR) spectroscopy as well as with size exclusion chromatography (SEC) using a light scattering detector to confirm block formation. Thermal characterization of the resulting polymers was done with differential scanning calorimetry (DSC) and rotational rheometry (RR). Detailed melt rheology of the polymers was studied and the effect of PDM segment on melt rheology is discussed here.

2. Experimental

2.1. Materials

The molecular structures of the used pre-polymers/macroinitiators are listed in Table 1. PEO and PPO were received from Fluka (Gallen, Switzerland) and PEO-PPO-PEO was from Aldrich (St. Louis, MO, USA). The initiator for PDM homopolymerization was ethylene glycol (EG) from Riedel de Haen (Seelze, Germany). Chemical structures of the different blocks are presented in Figure 1. Other materials and their suppliers were: 2-(dimethylamino) ethyl methacrylate (DMAEMA), potassium hydride (KH) (30 w% suspension in mineral oil), and triethyl amine (TEA) from Aldrich (St. Louis, MO, USA); basic alumina, methanol and methylene iodide from Fluka (Gallen, Switzerland); ethanol from Altia (Rajamäki, Finland); diethylether, hexane and acetone from BHD Prolabo (VWR, Karlskoga, Sweden); sodium chloride from Merck (Whitehouse Station, NJ, USA); chloroform ($CHCl_3$) from VWR (Karlskoga, Sweden). All chemicals used were of reagent grade.

PEO was purified by precipitation from cold ethanol followed by drying in a vacuum oven overnight [37]. PEO-PPO-PEO and PPO were purified by drying in a vacuum oven overnight. DMAEMA was purified by removing inhibitor by filtration through basic alumina. DMAEMA was stored in a refrigerator before use. All the solvents used in oxyanionic synthesis were dried with molecular sieves for several days. Other chemicals were used without further treatment.

Table 1. Block composition and dn/dc values of the pre-polymers (in $CHCl_3$/TEA (2%) solution)

Pre-polymer	Composition [g/mol]			dn/dc
	PEO	PPO	PEO	[ml/g]
PEO	10 000	–	–	0.060
PEO-PPO-PEO-H (PEO High)	6 000	2500	6000	0.050
PEO-PPO-PEO-L (PEO Low)	850	4100	850	0.035
PPO	–	2000	–	0.020

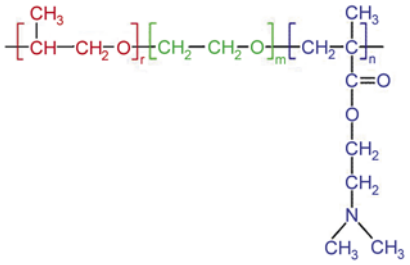

Figure 1. The block structures of PPO (left), PEO (middle), and PDM (right)

2.2. Synthesis of block co-polymers

Amphiphilic water soluble block copolymers were prepared through oxyanionic synthesis. Linear hydroxyl functionalized EG, PEO, PPO or PEO-PPO-PEO were activated with potassium hydride (KH). KH reacted with OH-groups and the resulting activated polymer (e.g. K-PEO-K) was used as a macroinitiator. The synthesis was carried out at 25°C according to the following example procedure: 10 g of PEO and 950 mg of 30% potassium hydride suspension was added to a dry reaction vessel and argon atmosphere was assured with three vacuum cycles. Under argon atmosphere, 50 ml THF was added to the solution. Homogeneity of the solution was achieved by warming the mixture at 45°C for 15 minutes. The vessel was cooled down and the activation reaction was continued for 1.5 hours at ambient temperature (formed H_2 removed through a needle). The polymerization was started by adding 15.8 ml of DMAEMA dropwise and carried out for one hour. The reaction was quenched with methanol and precipitated with diethyl ether and hexane. The yield was 13.4 g. The theoretical molecular weight of the PDM block was 7400 g/mol.

2.3. Nuclear magnetic resonance spectroscopy (NMR)

The NMR spectrum was obtained using a 300 MHz Varian Gemini 2000 (Agilent Technologies, Santa Clara, CA, USA) with deuterated chloroform ($CDCl_3$) as the solvent. Conversion of the synthesis (decrease of vinylidene groups) was followed with ^1H NMR spectroscopy. Polymer structure was identified based on proton peaks of CH_2 (PEO) at 3.64 ppm, $N(CH_3)_2$ (PDM) at 2.27 ppm or CH_3 (PPO) at 1.16 ppm [38]. Reacted end groups were detected in quantitative ^{13}C NMR based on absence of a peak at 61.5 ppm in PEO and at 65.5 and 67.1 in PPO.

2.4. Size exclusion chromatography (SEC)

Purified polymers were analysed with size exclusion chromatography (SEC) using chloroform with 2% triethylamine (TEA) as eluent. Elution speed was 1 ml/min through the following column system: PLgel pre-column and PLgel, 10^4, 10^5, 10^3 and 10^2 Å columns supplied by Polymer laboratories (Agilent Technologies, Santa Clara, CA, USA). Relative changes in molecular weight were determined with a Waters RI-detector (refractive index) (Waters, Milford, MA, USA) against polystyrene standards at 35°C. A Wyatt Dawn 8^+ MALLS (multiangle laser light-scattering) detector (Wyatt Technology, Dernbach, Germany) was used to analyse both molecular weight and size of the polymer. The difference in refractive index between eluent and polymer (dn/dc) was estimated assuming 100% recovery of the known mass concentration through the elution system.

2.5. Differential scanning calorimetry (DSC)

The thermal behavior of polymers was measured with a Mettler Toledo DSC 821^e (Mettler Toledo, Gerifensee Switzerland) differential scanning calorimeter under a nitrogen atmosphere. The sample size was 7–10 mg for crystalline polymers, and 25 mg for amorphous polymers. Before nonisothermal runs the samples were heated to equalization temperature (150°C) followed by immediate determination of the crystallization temperature (T_c) at a cooling rate of –10°C/min (from 150 to –100°C). After this cooling step, the melting endotherm (ΔH), glass transition point (T_g), and the peak melting temperature (T_m) were measured by reheating the sample from –100 to 100°C. The used heating rate was 20 °C/min to improve the detectability of T_g. In addition to this, the PDM-PEO-PPO-PEO-PDM-L polymer was studied in more detail by determining the influence of the different heating (5, 10, 20 and 40°C/min) and cooling rates (–2, –5, –10, –20°C/min) on the cold crystallization. Also the influence of different equalization temperatures (150, 100, 80, 60, 50, 40°C) were studied for the PDM-PEO-PPO-PEO-PDM-L polymer.

2.6. Rotational rheometry (RR)

Thermal behaviour of the polymers was measured with an Anton Paar Physica MRC 301 dynamic rotational rheometer (Anton Paar GmbH, Graz, Austria) operated in strain-controlled mode. Temperature was controlled with a Peltier heating element on the lower plate, and cooling was done with a water circulator. 25 mm plate geometry with gap size of 150 μm was used. The dimensional changes in geometry during measurements were taken into account by controlling the gap size with a normal force, and measuring the gap size with a TruGap induction sensor (gap size decreased from 150 to 138 μm due to the shrinking of the polymer during the cooling

ramp). The sample was stabilized at 100°C for 30 min before the measurement. The measured temperature ramp was cooling from 100 to –30°C at 5 °C/min followed by immediate heating back to 100°C with the same rate. Oscillatory measurement was done at 0.1% strain within the linear viscoelastic region at 10 Hz frequency. Moduli and complex viscosity were recorded. Frequency sweeps for time temperature superposition (TTS) calculations were measured from 300 to 0.03 rad/s with the same gap settings. The TTS measuring temperatures were 40, 30, 20, 10, 5, 0, –5, –10, –15, –20, –25°C (50 s stabilization between the measurements) and shift factors were calculated by the Rheoplus software according to Williams-Landel-Ferry (WLF) equation [39].

Single temperature frequency sweeps were measured with a stress-controlled rheometer (TA Instruments AR-G2,TA Instruments, New Castle, DE, USA). The measurements were done at 60°C or, for polymers without PPO, at 65°C with 25 mm plate geometry using a 250 μm gap. The strain used was 0.1% and the measurement was done with a frequency range of 0.01–100 Hz.

3. Results and discussion

3.1. Synthesis and characterization of block co-polymers

Oxyanionic polymerization can be carried out in two different ways, namely directly from potassium hydride (KH) or through a $DMSO^{-}K^{+}$ complex [16] (DMSO = dimethyl sulfoxide). The $DMSO^{-}K^{+}$ method is assumed to be more accurate since the conversion of macroinitiator into $RO^{-}K^{+}$ can easily be measured with triphenyl methane as an indicator. In this study the initiation from KH was determined adequate for the polymerization. An excess of KH was used to eliminate possible termination reactions caused by residual OH groups [20].

After the synthesis step, all analyses were performed on purified samples as some PDM homopolymer was usually formed in the crude reaction solution. After purification, the formation of block structure was confirmed with ^{13}C NMR, and SEC equipped with MALLS. To obtain reliably molecular weight analysis (using SEC with MALLS detector), the d*n*/d*c* values of the pre-polymers should be available. There was no literature data available concerning d*n*/d*c* values for PEO and PPO in $CHCl_3$/TEA (2%) solution, and therefore the dn/dc values were first determined for the whole set of macroinitiators. The values were determined from chromatographic analysis assuming 100% recovery from the elution system and the scattering data was calculated using a Zimm plot. dn/dc values obtained for pre-polymers (Table 1) varied in line with the molecular compositions, so that a dn/dc of 0.06 ml/g was achieved for pure PEO and 0.02 ml/g for pure PPO. The other macroinitiators gave values between these two depending on block composition. The measured value of 0.02 ml/g for PPO was rather low but still above the resolution limit of the equipment. d*n*/d*c* values for modified polymers are listed in Table 2. PDM had the highest d*n*/d*c* and it was markedly different from the value of 0.02 obtained for macroinitiator PPO. In addition, the experimental dn/dc values were consistent with the theoretical values calculated from macroinitiators and PDM homopolymer as averages based on molecular composition.

The results from SEC/MALLS analysis are presented in Table 2 and the formation of PDM block was supported by the increase in molecular weight compared to pre-polymers in Table 1. In addition, the molecular weight distributions of PDM-PEO-PDM and PDM-PPO-PDM remained narrow whereas a slightly broader distribution for PDM-PEO-PPO-PEO-PDM-H and PDM-PEO-PPO-PEO-PDM-L

Table 2. Molecular weight characterization of the synthesized block polymers using MALLS SEC

Polymer	dn/dc[a] [ml/g]	dn/dc[b] [ml/g]	Molecular weight [g/mol]		
			M_n	M_w	PD
PDM	0.070	0.07	14 600	19 900	1.37
PDM-PEO-PDM	0.064	0.07	26 500	28 300	1.07
PDM-PEO-PPO-PEO-PDM-H	0.057	0.06	32 300	48 400	1.50
PDM-PEO-PPO-PEO-PDM-L	0.055	0.06	11 000	17 000	1.55
PDM-PPO-PDM	0.060	0.06	13 900	14 300	1.03

[a]theoretical values
[b]values from SEC

was observed. Finally, successful initiation of the end groups was detected in ^{13}C NMR as an absence of peaks at 61.5 ppm (PEO, $\underline{C}H_2$–OH) or at 65.5 and 67.1 ppm (PPO, $\underline{C}(CH_3)H$–OH and $\underline{C}H_2$–OH respectively).

3.2. Thermal transition temperatures with DSC

Thermal transition temperatures analysed with the DSC are presented in Table 3 and in Figures 2–4. PPO is completely amorphous, with a glass transition point at –67°C (Figure 2 A), whereas pure PEO is a highly crystalline polymer which melts at 66°C (Figure 3 C). The melting temperatures of the crystalline PEO phases in their block copolymers, PEO-PPO-PEO-H and PEO-PPO-PEO-L, are lower (Figure 3 D and 4 A, 61 and 39°C, respectively) but this is mostly due to the shorter PEO block sizes (Table 1, 6000 and 850 g/mol, respectively: e.g. PEO 1000 g/mol from Fluka, T_m 37–40°C). In addition, the T_g of the PPO phase is only slightly influenced by the amount of PEO. These results indicate that PEO and PPO were phase separated at solid state.

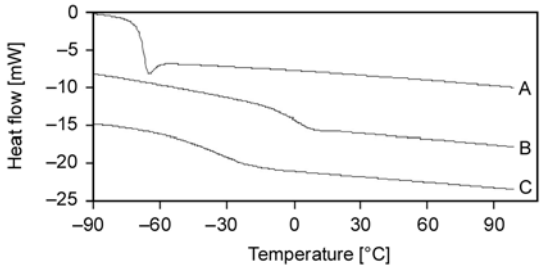

Figure 2. Glass transition points observed in DSC heating sequences for the amorphous polymers, A) PPO pre-polymer, B) PDM reference, and C) PDM-PPO-PDM

The reference PDM homopolymer was found to be totally amorphous with T_g at 1°C which is in consistent with the literature [40]. However, this thermal transition was not as clear as that of the amorphous PPO (Figure 2 B vs. A). This phenomenon was observed also in their amorphous block copolymer, PDM-PPO-PDM, and only a modest T_g at about –20°C (Figure 2 C) could be observed. In addition, no separate T_g from PPO was observed which indicates that the PDM and PPO phases were most likely mixed in the solid PDM-PPO-PDM block copolymer.

Modification of the highly crystalline PEO and PEO-PPO-PEO-H polymers with PDM-blocks affected the transition temperatures slightly (Table 3, Figure 3). T_m and T_c of the crystalline PEO phase were reduced 5–8°C but the crystallinity (ΔH) was remained mostly at the same level in modified polymers. It was clear that the PDM-blocks did not prevent the crystallization of the PEO-segments, which usually indicates that the phases are separated in the solid polymer [29]. Additionally, no glass transition point either due to the amorphous PPO or PDM phase was observed. This is consistent with the results above, which indicated that the T_g is less distinct in polymers containing both PDM and PPO segments.

The most interesting behaviour was found with PDM-PEO-PPO-PEO-PDM-L (Figure 4 B). According to DSC, initially the polymer behaved like a completely amorphous polymer as no crystallization exotherm was observed in the cooling sequence from 150 to –100°C. However, in the heating sequence, a clear crystallization peak (T_c) was found followed immediately by a melting peak. In gen-

Table 3. Thermal transition temperatures and enthalpies (ΔH) of the studied block-copolymers. Values in parenthesis are thermal transitions observed with rheometer.

Pre-polymer	DSC (Rheometer)			
	T_g [°C]	T_c [°C]	T_m [°C]	$\Delta H_{PEO\text{-}phase}$ [J/g]
PEO	–	41	66 (62)	180
PEO-PPO-PEO-H	–61	39	61 (58)	150
PEO-PPO-PEO-L	–65	17	39 (38)	170
PPO	–67	–	–	
Reference				
PDM	1 (5)	–	–	
Polymer				
PDM-PEO-PDM	–	35	58 (53)	220
PDM-PEO-PPO-PEO-PDM-H	–	34	53 (49)	180
PDM-PEO-PPO-PEO-PDM-L	–60	–12 (–15)	14 (10)	48
PDM-PPO-PDM	–20 (–10)	–	–	

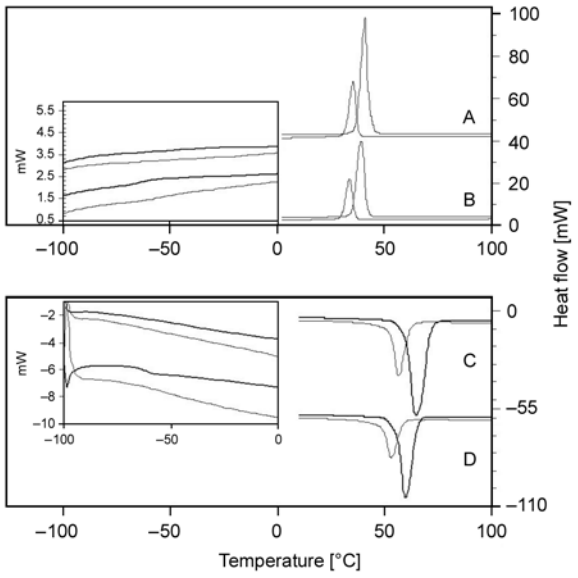

Figure 3. DSC cooling curves of A) PEO, PDM-PEO-PDM B) PEO-PPO-PEO-H, PDM-PEO-PPO-PEO-PDM-H. DSC heating curves of C) PEO, PDM-PEO-PDM D) PEO-PPO-PEO-H, PDM-PEO-PPO-PEO-PDM-H. The thicker curves are for PEO and PEO-PPO-PEO-H.

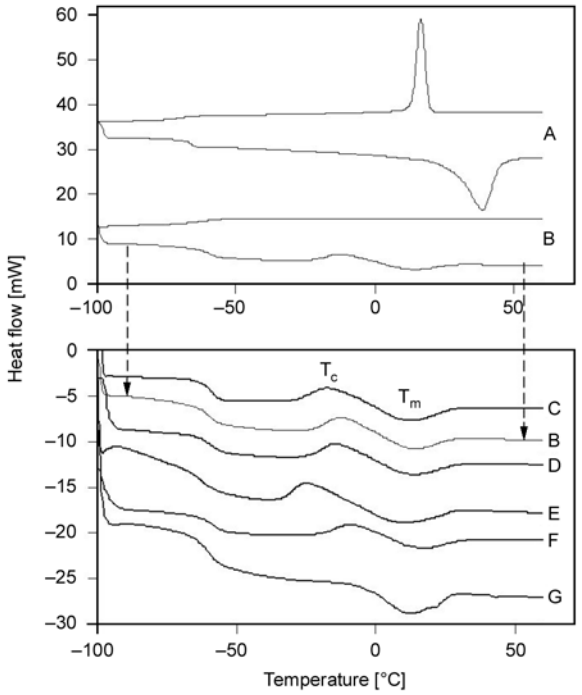

Figure 4. DSC heating and cooling curves of A) PEO-PPO-PEO-L pre-polymer, B) PDM-PEO-PPO-PEO-PDM-L. Heating curves of PDM-PEO-PPO-PEO-PDM-L with varying parameters, C) cooling –2°C/min, heating 20°C/min B) cooling –10°C/min, heating 20°C/min, D) cooling –20°C/min, heating 20°C/min, E) cooling –10°C, heating 5°C/min, and F) cooling –10°C, heating 40°C/min, G) cooling –10°C/min, heating 20°C/min after the thermal history was equalized at 40 °C.

eral, this kind of behaviour is known as cold crystallization [41] and is typical for polymers [42] and blends [43] that contain both soft and hard segments, as is the case for the PDM-PEO-PPO-PEO-PDM-L structure. Cold crystallization is also often dependent on heating/cooling rate [44], which, however, was not clearly the case in this polymer. The influence of cooling rate was minor (Figure 4 B, C, D) whereas the ΔH were slightly affected by varying the heating rate (Figure 4 E ΔH = 10 J/g; 4 F ΔH = 6 J/g). Finally, when the equalization temperature was reduced from 150 to below 50°C, the cold crystallization was absent and only melting endotherm (Figure 4 G, T_m at ~10°C) was observed during heating. Still, this melting endotherm differed largely when compared with the one obtained for unmodified PEO-PPO-PEO-L (T_m ~10°C vs. 39°C; $\Delta H_{PEO\text{-}phase}$ 48 J/g vs 170 J/g).

One explanation to the thermal behaviour of PDM-PEO-PPO-PEO-PDM-L can be the strong phase mixing at melt state (equalization temperature 50°C or higher), which hindered the homogeneous and/or heterogeneous nuclei formation during the cooling sequence. As well known the absence of any nuclei will effectively prevent the crystallization of the polymer phase. However, when the PDM-PEO-PPO-PEO-PDM-L was equalized only at 40°C, the polymer melt contained probably some unmelted domains which then acted as nucleation centres supporting the crystallization during the cooling sequence. This hypothesis can be associated with the results of Hillmyer and Bates [45] where the melted polyalkane-block-PEO copolymer was found to maintain small crystalline PEO fractions.

3.3. Thermal transition temperatures measured by rheometry

Rotational rheometry was also used to analyse thermal transition behaviour. However, crystallization kinetics can cause problems when measuring temperature transitions with rheometry. Strain-induced crystallization can be problem when a stress-controlled instrument is used [46]. That can lead to high strains and differences in the rate of crystallization measured by rheometry versus DSC. In this study the strain-controlled measurement was performed at very low strain, hence mitigating the risk

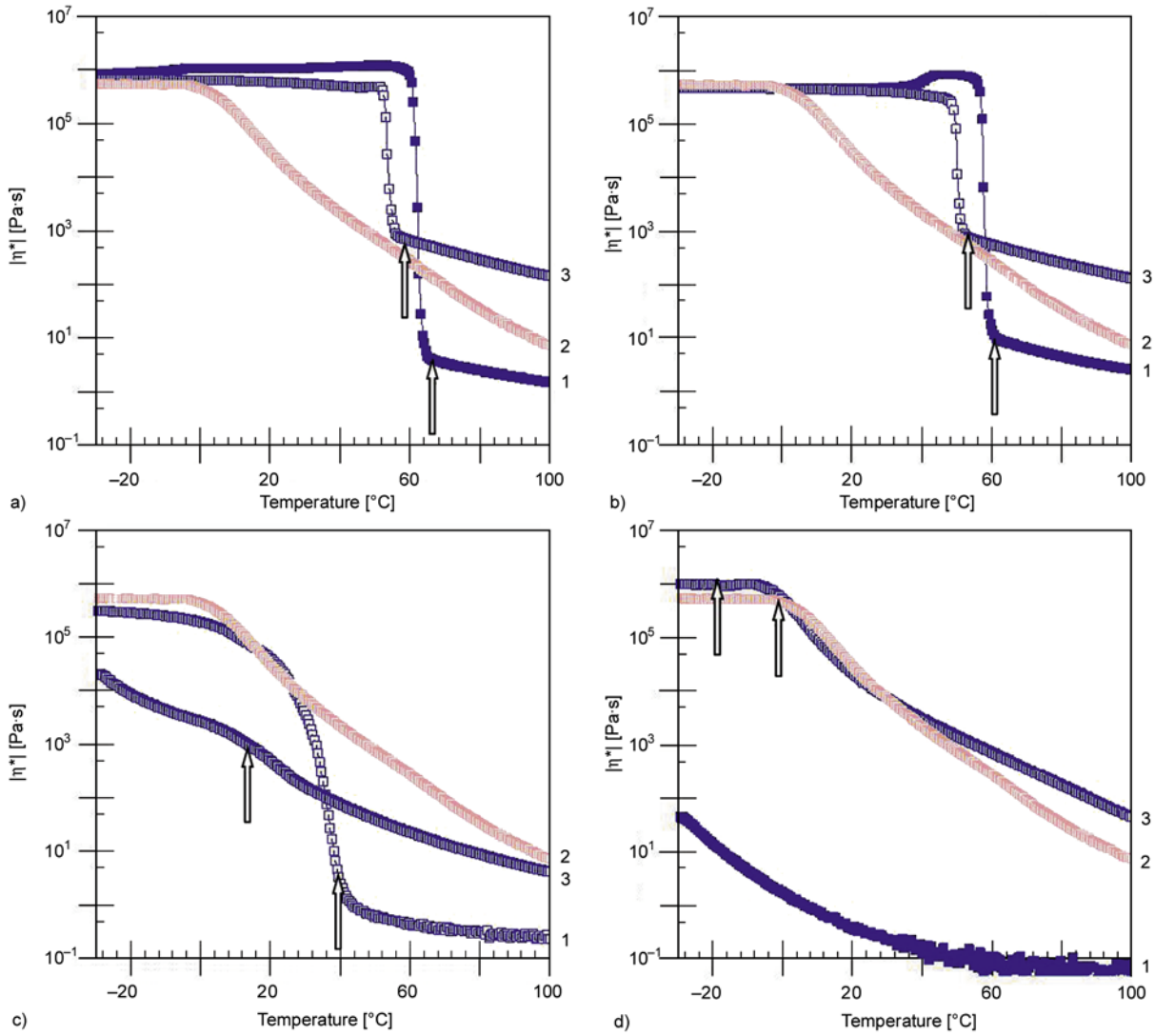

Figure 5. Effect of PDM on thermal transition behaviour observed as complex viscosity of a) 1 = PEO, 2 = PDM, 3 = PDM-PEO-PDM; b) 1 = PEO-PPO-PEO-H, 2 = PDM, 3 = PDM-PEO-PPO-PEO-PDM-H; c) 1 = PEO-PPO-PEO-L, 2 = PDM, 3 = PDM-PEO-PPO-PEO-PDM-L; d) 1 = PPO, 2 = PDM, 3 = PDM-PPO-PDM. Thermal transition points determined with DSC are marked with arrows.

of strain-induced crystallization. In addition, the ability to controlled strain instead of stress produced repeatable results, and sensitivity was additionally increased by using 10 Hz frequency.

The problem with temperature scans can be that hard polymers may be outside equipment's maximum torque range. In our case, however, the polymers were soft enough so that the melting temperatures as well the glass transition points were clearly obtained as decrease in complex viscosity (Figures 5 a–d). The obtained transition temperatures were consistent with the DSC results even though a slight systematic deviation of few degrees was observed between the results (Table 3). In addition, the T_g's of PDM and PDM-PPO-PDM were more distinct when compared with the DSC analysis. Still, either the rheometer was not able to detect separate T_g originating from PDM in any of the polymers containing PEO. The absence of T_g is consistent with the very high viscosity values for PDM-PEO-PDM and PDM-PEO-PPO-PEO-PDM-H obtained below the melting point. At the temperature where the glassy stage of PDM should be softened, PEO is still strongly crystalline with high viscosity, thus binding the PDM and preventing softening. Finally, in addition to the basic thermal transitions, a slight but clear increase in viscosity of solid PEO-PPO-PEO-H was found around 40°C

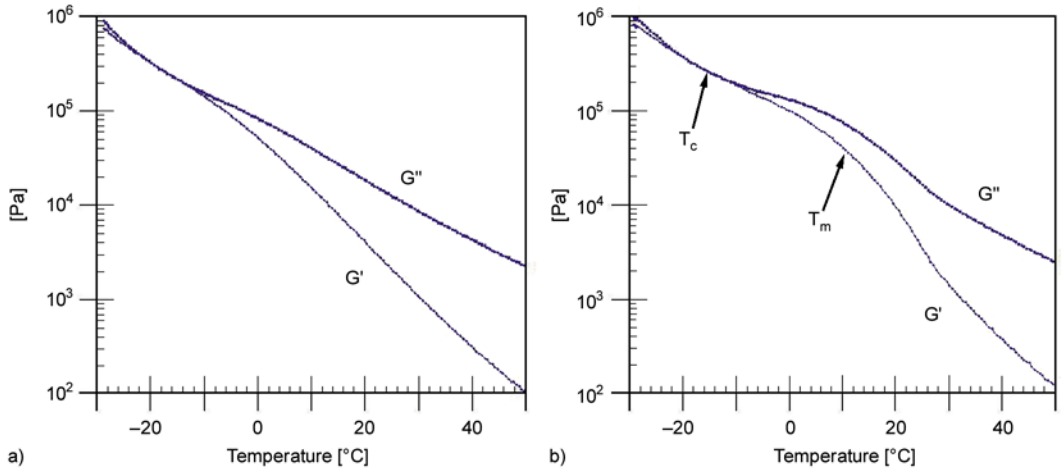

Figure 6. Thermal transition behaviour of storage (G') and loss (G'') modulus in cooling (a) and heating ramp (b) of PDM-PEO-PPO-PEO-PDM-L

(Figure 5 b 1). This kind of increase in viscosity may indicate microphase separation or order disorder transition point [32].

The cold crystallization behaviour PDM-PEO-PPO-PEO-PDM-L observed in DSC was studied in detail by comparing storage module (G') and loss module (G'') in cooling and heating cycles (Figure 6). Just like in DSC, the cold crystallization behaviour was seen only in heating cycle whereas cooling ramp did not indicate any phase transitions occurring. T_c was determined as tangential point of G' and G'' whereas T_m could be seen as clear decrease in modulus. It was also remarkable that regardless of the thermal transition points, G'' was practically higher than G' over the whole range of temperatures. That indicates that this polymer behaves as a high viscosity fluid. This kind of rheological behaviour is normally seen in polymer melts containing some crystalline parts [34].

3.4. Melt rheology

Modification of the pre-polymers with PDM-blocks clearly increased melt viscosity of one to three orders of magnitude as can be observed in Figure 5. Still, the weak temperature/viscosity dependence (at the melt state) of the pre-polymers was maintained in the modified polymers. It must also be noted that the melt viscosity of PDM-containing

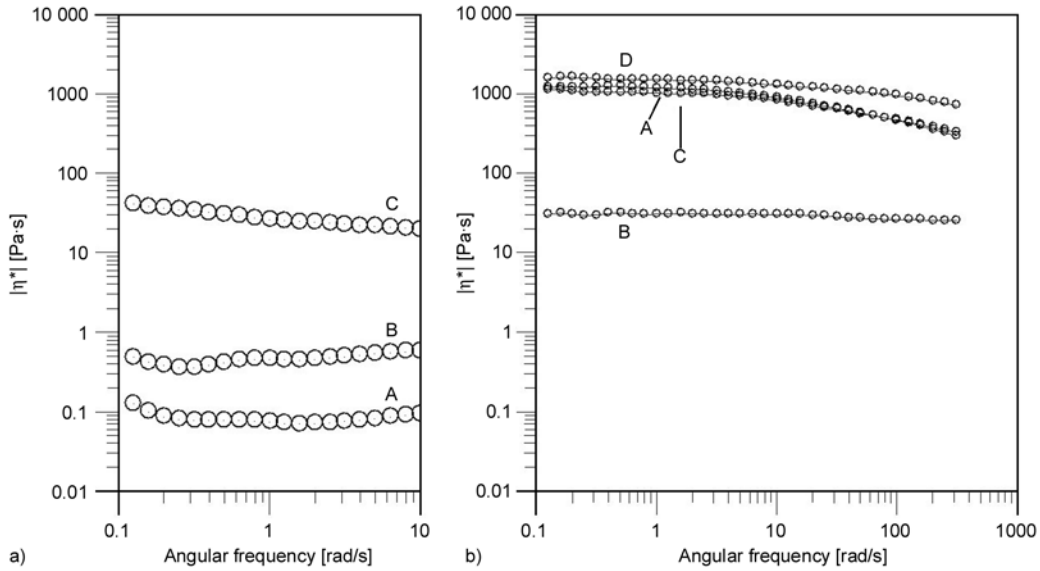

Figure 7. Complex viscosity of pre-polymers (a): A = PPO, B = PEO-PPO-PEO-L, C = PEO-PPO-PEO-H and modified block co-polymers (b): A = PDM-PPO-PDM, B = PDM-PEO-PPO-PEO-L, C = PDM-PEO-PPO-PEO-H, D = PDM

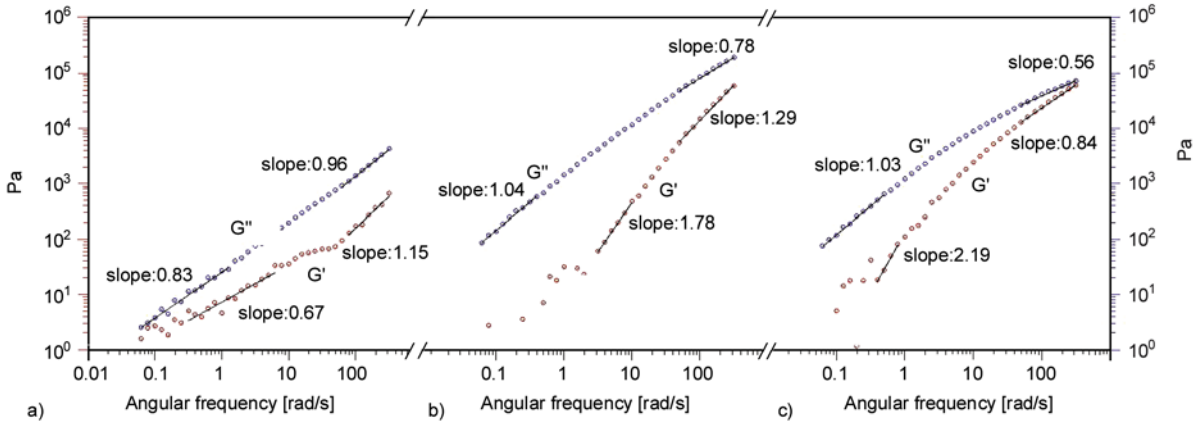

Figure 8. Frequency sweeps of a) PEO-PPO-PEO-H, b) PDM and c) PDM-PEO-PPO-PEO-PDM-H measured at 60°C

polymer was higher than the average of PDM and the corresponding pre-polymer in all polymers except PDM-PEO-PPO-PEO-PDM-L.

In frequency sweeps the complex viscosity of the pre-polymers showed only a weak frequency dependency indicating strong Newtonian behaviour (Figure 7). This is consistent with what is reported in the literature [24] and indicates that PEO and PPO do not form entanglements at the melt stage. However, these polymers had also measurable storage modulus (Figure 8 a and b), which is slightly contradictory with the assumption of Newtonian fluid.

Modification of the pre-polymers (excluding PEO-PPO-PEO-L) with PDM was seen as the appearance of a shear thinning character (Figure 7) and with an obvious elastic modulus (Figure 8c). The module dependence of angular frequency (ω) was calculated and correlations $G''\sim\omega^1$ and $G'\sim\omega^2$ were observed at low shear rates (slopes in Figure 8c). This terminal slope was similar to what is generally seen for entangled polymer melts [34]. Still, no cross-over point for the moduli was observed, but this was due to the limited experimental window available.

3.5. Time temperature superposition (TTS) frequency sweeps for *PDM-PEO-PPO-PEO-PDM-L*

As mentioned above, the PDM-PEO-PPO-PEO-PDM-L seemed to act as a Newtonian fluid (at 60°C) even though the other PDM-modified pre-polymers exhibited clear shear thinning behaviour. Therefore the TTS was calculated for PDM-PEO-PPO-PEO-PDM-L in order to find changes in material characteristics over a wider range of frequencies. Unfortunately, the TTS was not suitable for polymers that exhibit strong phase transition at the used temperature range [23], and therefore the direct comparison e.g. with unmodified PEO-PPO-PEO-L was not performed.

The TTS measurements for PDM-PEO-PPO-PEO-PDM-L were performed from 40 to –25°C to avoid the cold crystallization. The TTS calculations were referenced at 35°C (Figure 9) and a clear shear thinning behaviour for PDM-PEO-PPO-PEO-PDM-L was observed. The complex viscosity decreased in parallel of increase in shear force, and a low frequency behaviour ($G''\sim\omega^1$ and $G'\sim\omega^2$) typical for entangled polymer melts was present. Also a clear cross-over point for G' and G'' was found in frequency ramps at around 100 000 rad/s. The earlier Newtonian behaviour of PDM-PEO-PPO-PEO-

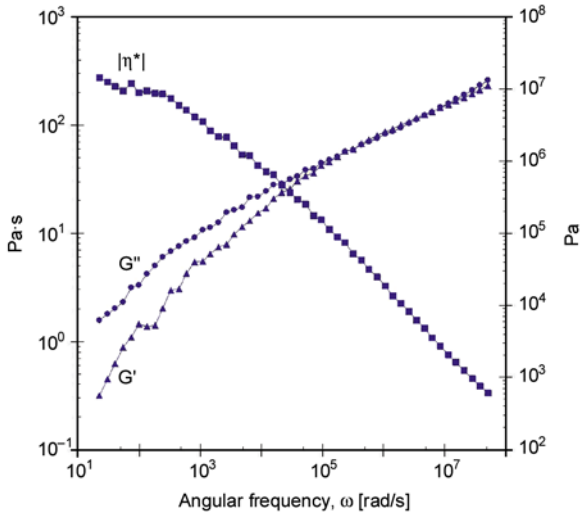

Figure 9. Frequency dependence expressed as complex viscosity (η*), storage modulus (G') and loss modulus (G'') of PDM-PEO-PPO-PEO-PDM-L. Horizontal shift factor $a_T = 0.2468$ and vertical shift factor $b_T = 2.039$. Reference temperature is 35°C.

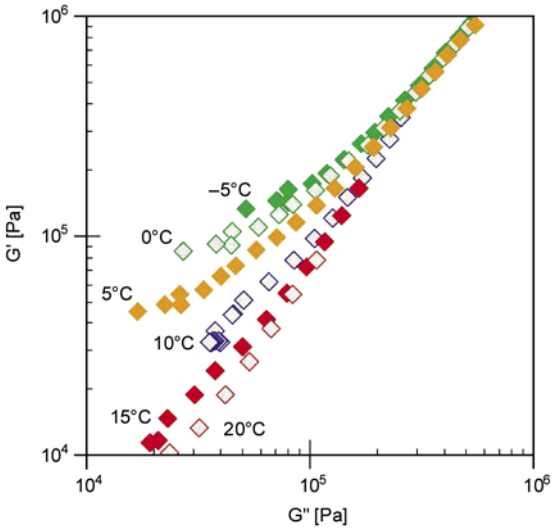

Figure 10. G'' of PDM-PEO-PPO-PEO-PDM-L plotted against G' in frequency sweeps at different temperatures

PDM-L (Figure 7) originated most likely due to the high measuring temperature, where the complex viscosity was at the Newtonian plateau over the whole range of frequencies.

The abovementioned TTS measurements were performed also by starting at the lowest temperature when the cold crystallization of PDM-PEO-PPO-PEO-PDM-L was present. Because of occurring phase transition the master curve could not be done, and instead Cole-Cole correlation [33] was plotted (Figure 10, temperature range from –5 to 20°C). At high frequency area hardly any deviations in the ratio of G' and G'' could be observed between the temperatures, but at low frequencies the impact of G' gets stronger at lower temperatures. This is a clear indication of occurring phase transition [29], but the detailed microstructure still remains unclear.

4. Conclusions

Block polymers were successfully synthesized by using a potassium functionalized pre-polymer as initiator. The formation of block structure was confirmed with SEC and NMR. Thermal transitions were determined by calorimetric and rheological means, and the results were consistent with each other. The thermal behaviour, with obvious glass transitions and melting endotherms, indicated that poly(ethylene oxide) (PEO) and poly(propylene oxide) (PPO) segments are mostly phase separated in these copolymers at solid state. Modification with poly[2-(dimethylamino)ethyl methacrylate] (PDM) did affect the thermal transition temperatures of the PEO-rich pre-polymer only slightly, whereas more significant changes were observed in PPO-rich polymers. Thermal behaviour indicates that PDM is phase separated from PEO but forms a mixed phase with PPO. Cold crystallization behaviour for PPO-rich PDM-PEO-PPO-PEO-PDM-L could be observed in DSC measurements as well as in temperature scan in rheometer.

Melt rheology of the block copolymers confirmed that PEO and PPO block co-polymers behaved almost as Newtonian liquids over the whole range of frequencies. Rheological characterization of the block co-polymers also confirmed that melt viscosity of the pre-polymers was increased by modifying them with PDM block. Additionally, PDM segments seemed to increase frequency dependence of the polymers slightly and to modify polymers from Newtonian into shear thinning fluids. Overall, the frequency sweeps confirmed the behaviour seen in temperature scans. No cross-over frequency was found for polymers without PDM, but the elastic component originating from PDM can give advantage in melt processing of these polymers.

References

[1] Lodge T. P.: Block copolymers: Past successes and future challenges. Macromolecular Chemistry and Physics, **204**, 265–273 (2003).
DOI: 10.1002/macp.200290073

[2] Mortensen K., Batsberg W., Hvidt S.: Effects of PEO–PPO diblock impurities on the cubic structure of aqueous PEO–PPO–PEO pluronics micelles: fcc and bcc ordered structures in F127. Macromolecules, **41**, 1720–1727 (2008).
DOI: 10.1021/ma702269c

[3] Ibrahim K., Salminen A., Holappa S., Kataja K., Lampinen H., Löfgren B., Laine J., Seppälä J.: Preparation and characterization of polystyrene–poly(ethylene oxide) amphiphilic block copolymers via atom transfer radical polymerization: Potential application as paper coating materials. Journal of Applied Polymer Science, **102**, 4304– 4313 (2006).
DOI: 10.1002/app.24886

[4] Nurmi L., Holappa S., Nykänen A., Laine J., Ruokolainen J., Seppälä J.: Ultra-thin films of cationic amphiphilic poly(2-(dimethylamino)ethyl methacrylate) based block copolymers as surface wettability modifiers. Polymer, **50**, 5250–5261 (2009).
DOI: 10.1016/j.polymer.2009.08.043

[5] Vesterinen A-H., Rich J., Myllytie P., Laine J., Seppälä J.: Poly(ethylene oxide)-*block*-poly[2-(dimethylamino) ethyl methacrylate] as strengthening agent in paper: Dynamic mechanical characterization. Macromolecular Materials and Engineering, **295**, 269–275 (2010). DOI: 10.1002/mame.200900317

[6] Vesterinen A-H., Rich J., Seppälä J.: Synthesis and solution rheology of poly[(stearyl methacrylate)-*stat*-([2-(methacryloyloxy)ethyl] trimethyl ammonium iodide)]. Journal of Colloid and Interface Science, **351**, 478–484 (2010). DOI: 10.1016/j.jcis.2010.07.073

[7] Peng Z., Li G., Liu X., Tong Z.: Synthesis, pH- and temperature-induced micellization and gelation of doubly hydrophilic triblock copolymer of poly(*N,N*-dimethylamino-2-ethylmethacrylate)-*b*-poly(ethylene glycol)-*b*-poly(*N,N*-dimethylamino-2-ethylmethacrylate) in aqueous solutions. Journal of Polymer Science Part A: Polymer Chemistry, **46**, 5869–5878 (2008). DOI: 10.1002/pola.22904

[8] Baines F. L., Billingham N. C., Armes S. P.: Synthesis and solution properties of water-soluble hydrophilic–hydrophobic block copolymers. Macromolecules, **29**, 3416–3420 (1996). DOI: 10.1021/ma951699+

[9] Zeng F., Shen Y., Zhu S., Pelton R.: Synthesis and characterization of comb-branched polyelectrolytes. 1. Preparation of cationic macromonomer of 2-(dimethylamino)ethyl methacrylate by atom transfer radical polymerization. Macromolecules, **33**, 1628–1635 (2000). DOI: 10.1021/ma991654z

[10] de Paz Báñez M. V., Robinson K. L., Bütün V., Armes S. P.: Use of oxyanion-initiated polymerization for the synthesis of amine methacrylate-based homopolymers and block copolymers. Polymer, **42**, 29–37 (2000). DOI: 10.1016/S0032-3861(00)00329-3

[11] Nagasaki Y., Sato Y., Kato M.: A novel synthesis of semitelechelic functional poly(methacrylate)s through an alcoholate initiated polymerization. Synthesis of poly[2-(*N,N*-diethylaminoethyl) methacrylate] macromonomer. Macromolecular Rapid Communications, **18**, 827–835 (1997). DOI: 10.1002/marc.1997.030180911

[12] Vamvakaki M., Billingham N. C., Armes S. P.: Synthesis of controlled structure water-soluble diblock copolymers via oxyanionic polymerization. Macromolecules, **32**, 2088–2090 (1999). DOI: 10.1021/ma981779o

[13] Lascelles S. F., Malet F., Mayada R., Billingham N. C., Armes S. P.: Latex syntheses using novel tertiary amine methacrylate-based macromonomers prepared by oxyanionic polymerization. Macromolecules, **32**, 2462–2471 (1999). DOI: 10.1021/ma981967e

[14] Tong D., Yao J., Li H., Han S.: Synthesis and characterization of thermo- and pH-sensitive block copolymers bearing a biotin group at the poly(ethylene oxide) chain end. Journal of Applied Polymer Science, **102**, 3552–3558 (2006). DOI: 10.1002/app.24812

[15] Ni P-H., Pan Q-S., Zha L-S., Wang C-C., Elaïssari A., Fu S-K.: Syntheses and characterizations of poly[2-(dimethylamino)ethyl methacrylate]-poly(propylene oxide)-poly[2-(dimethylamino)ethyl methacrylate] ABA triblock copolymers. Journal of Polymer Science Part A: Polymer Chemistry, **40**, 624–631 (2002). DOI: 10.1002/pola.10144

[16] de Paz Báñez M. V., Robinson K. L., Armes S. P.: Synthesis and solution properties of dimethylsiloxane–2-(dimethylamino)ethyl methacrylate block copolymers. Macromolecules, **33**, 451–456 (2000). DOI: 10.1021/ma991665s

[17] de Paz Báñez M. V., Robinson K. L., Vamvakaki M., Lascelles S. F., Armes S. P.: Synthesis of novel cationic polymeric surfactants. Polymer, **41**, 8501–8511 (2000). DOI: 10.1016/S0032-3861(00)00217-2

[18] Jin L., Deng Y., Hu J., Wang C.: Preparation and characterization of core–shell polymer particles with protonizable shells prepared by oxyanionic polymerization. Journal of Polymer Science Part A: Polymer Chemistry, **42**, 6081–6088 (2004). DOI: 10.1002/pola.20453

[19] Li Y., Armes S. P.: Synthesis of branched water-soluble vinyl polymers via oxyanionic polymerization. Macromolecules, **38**, 5002–5009 (2005). DOI: 10.1021/ma050333m

[20] Anderson B. C., Cox S. M., Bloom P. D., Sheares V. V., Mallapragada S. K.: Synthesis and characterization of diblock and gel-forming pentablock copolymers of tertiary amine methacrylates, poly(ethylene glycol), and poly(propylene glycol). Macromolecules, **36**, 1670–1676 (2003). DOI: 10.1021/ma0211481

[21] Iijima M., Nagasaki Y., Kato M., Kataoka K.: A potassium alcoholate-initiated polymerization of 2-(trialkylsiloxyethyl) methacrylate. Polymer, **38**, 1197–1202 (1997). DOI: 10.1016/S0032-3861(96)00623-4

[22] Ebagninin K. W., Benchabane A., Bekkour K.: Rheological characterization of poly(ethylene oxide) solutions of different molecular weights. Journal of Colloid and Interface Science, **336**, 360–367 (2009). DOI: 10.1016/j.jcis.2009.03.014

[23] Niedzwiedz K., Wischnewski A., Pyckhout-Hintzen W., Allgaier J., Richter D., Faraone A.: Chain dynamics and viscoelastic properties of poly(ethylene oxide). Macromolecules, **41**, 4866–4872 (2008). DOI: 10.1021/ma800446n

[24] Coppola S., Grizzuti N., Floudas G., Vlassopoulos D.: Viscoelasticity and crystallization of poly(ethylene oxide) star polymers of varying arm number and size. Journal of Rheology, **51**, 1007–1025 (2007).
DOI: 10.1122/1.2751076

[25] Floudas G., Tsitsilianis C.: Crystallization kinetics of poly(ethylene oxide) in poly(ethylene oxide)–polystyrene–poly(ethylene oxide) triblock copolymers. Macromolecules, **30**, 4381–4390 (1997).
DOI: 10.1021/ma9616118

[26] Yurekli K., Krishnamoorti R.: Dynamics of block copolymer micelles. Macromolecules, **35**, 4075–4083 (2002).
DOI: 10.1021/ma012024b

[27] Sebastian J. M., Lai C., Graessley W. W., Register R. A., Marchand G. R.: Steady-shear rheology of block copolymer melts: Zero-shear viscosity and shear disordering in body-centered-cubic systems. Macromolecules, **35**, 2700–2706 (2002).
DOI: 10.1021/ma011522h

[28] Wewerka A., Floudas G., Pakula T., Stelzer F.: Side-chain liquid-crystalline homopolymers and copolymers. Structure and rheology. Macromolecules, **34**, 8129–8137 (2001).
DOI: 10.1021/ma010944o

[29] Gopalan P., Zhang Y., Li X., Wiesner U., Ober C. K.: Liquid crystalline rod−coil block copolymers by stable free radical polymerization: Synthesis, morphology, and rheology. Macromolecules, **36**, 3357–3364 (2003).
DOI: 10.1021/ma021573u

[30] Almdal K., Koppi K. A., Bates F. S., Mortensen K.: Multiple ordered phases in a block copolymer melt. Macromolecules, **25**, 1743–1751 (1992).
DOI: 10.1021/ma00032a019

[31] Mok M. M., Pujari S., Burghardt W. R., Dettmer C. M., Nguyen S. T., Ellison C. J., Torkelson J. M.: Microphase separation and shear alignment of gradient copolymers: Melt rheology and small-angle X-ray scattering analysis. Macromolecules, **41**, 5818–5829 (2008).
DOI: 10.1021/ma8009454

[32] Bates F. S.: Block copolymers near the microphase separation transition. 2. Linear dynamic mechanical properties. Macromolecules, **17**, 2607–2613 (1984).
DOI: 10.1021/ma00142a025

[33] Rosedale J. H., Bates F. S.: Rheology of ordered and disordered symmetric poly(ethylenepropylene)-poly (ethylethylene) diblock copolymers. Macromolecules, **23**, 2329–2338 (1990).
DOI: 10.1021/ma00210a032

[34] Fredrickson G. H., Bates F. S.: Dynamics of block copolymers: Theory and experiment. Annual Review of Materials Science, **26**, 501–550 (1996).
DOI: 10.1146/annurev.ms.26.080196.002441

[35] Kossuth M. B., Morse D. C., Bates F. S.: Viscoelastic behavior of cubic phases in block copolymer melts. Journal of Rheology, **43**, 167–196 (1999).
DOI: 10.1122/1.550981

[36] Han C. D., Baek D. M., Kim J. K., Ogawa T., Sakamoto N., Hashimoto T.: Effect of volume fraction on the order-disorder transition in low molecular weight polystyrene-block-polyisoprene copolymers. 1. Order-disorder transition temperature determined by rheological measurements. Macromolecules, **28**, 5043–5062 (1995).
DOI: 10.1021/ma00118a038

[37] Harris J. M.: Laboratory synthesis of polyethylene glycol derivatives. Polymer Reviews, **25**, 325–373 (1985).
DOI: 10.1080/07366578508081960

[38] Dust J. M., Fang Z. H., Harris J. M.: Proton NMR characterization of poly(ethylene glycols) and derivatives. Macromolecules, **23**, 3742–3746 (1990).
DOI: 10.1021/ma00218a005

[39] Williams M. L., Landel R. F., Ferry J. D.: The temperature dependence of relaxation mechanisms in amorphous polymers and other glass-forming liquids. Journal of the American Chemical Society, **77**, 3701–3707 (1955).
DOI: 10.1021/ja01619a008

[40] Teoh R. L., Guice K. B., Loo Y-L.: Atom transfer radical copolymerization of hydroxyethyl methacrylate and dimethylaminoethyl methacrylate in polar solvents. Macromolecules, **39**, 8609–8615 (2006).
DOI: 10.1021/ma061650b

[41] Zhang J., Jiang L., Zhu L., Jane J-L., Mungara P.: Morphology and properties of soy protein and polylactide blends. Biomacromolecules, **7**, 1551–1561 (2006).
DOI: 10.1021/bm050888p

[42] Lu X., Hay J. N.: The effect of physical aging on the rates of cold crystallization of poly(ethylene terephthalate). Polymer, **41**, 7427–7436 (2000).
DOI: 10.1016/S0032-3861(00)00092-6

[43] O'Sickey M. J., Lawrey B. D., Wilkes G. L.: Structure–property relationships of poly(urethane-urea)s with ultralow monol content poly(propylene glycol) soft segments. III. Influence of mixed soft segments of ultralow monol poly(propylene glycol), poly(tetramethylene ether glycol), and tri(propylene glycol). Journal of Applied Polymer Science, **89**, 3520–3529 (2003).
DOI: 10.1002/app.12520

[44] Xu Z., Niu Y., Yang L., Xie W., Li H., Gan Z., Wang Z.: Morphology, rheology and crystallization behavior of polylactide composites prepared through addition of five-armed star polylactide grafted multiwalled carbon nanotubes. Polymer, **51**, 730–737 (2010).
DOI: 10.1016/j.polymer.2009.12.017

[45] Hillmyer M. A., Bates F. S.: Synthesis and characterization of model polyalkane–poly(ethylene oxide) block copolymers. Macromolecules, **29**, 6994–7002 (1996).
DOI: 10.1021/ma960774t

[46] Kelarakis A., Mai S-M., Booth C., Ryan A. J.: Can rheometry measure crystallization kinetics? A comparative study using block copolymers. Polymer, **46**, 2739–2747 (2005).
DOI: 10.1016/j.polymer.2005.01.068

eXPRESS Polymer Letters Vol.5, No.9 (2011) 766–776
Available online at www.expresspolymlett.com
DOI: 10.3144/expresspolymlett.2011.75

Oxidation and silanization of MWCNTs for MWCNT/vinyl ester composites

F. Avilés[*], *J. V. Cauich-Rodríguez, J. A. Rodríguez-González, A. May-Pat*

Centro de Investigación Científica de Yucatán, A.C., Unidad de Materiales Calle 43 # 130, Col. Chuburná de Hidalgo, 97200, Mérida, Yucatán, México

Received 27 December 2010; accepted in revised form 1 March 2011

Abstract. Chemical functionalization of multi-wall carbon nanotubes (MWCNTs) is conducted by means of acid oxidation, direct silanization of the as-received MWCNTs and a sequential treatment based on oxidation and silanization. Polymer composites made from the functionalized MWCNTs and a vinyl ester resin are fabricated and tested in compression. It is found that although silanization could be achieved without the assistance of a previous oxidative treatment, oxidizing the MWCNTs by HNO_3/H_2O_2 prior to silanization yields significantly better attachment of the silane molecules to the CNT surface and hence, better mechanical performance of the resulting composite. The limited improvements in mechanical properties found are discussed in light of the reduction of the nanotube length after MWCNT oxidation and composite processing.

Keywords: *nanocomposites, functionalization, silanization, oxidation, carbon nanotubes*

1. Introduction

The potential of carbon nanotubes (CNTs) as reinforcing elements in composite materials is based not only on the extraordinary mechanical properties of CNTs, but also on their relatively high aspect ratio (L/d) and surface area-to-volume ratio (A/V) [1–3]. Structures with high L/d are known to be more load-carrying efficient, while high A/V means more surface area at the same volume (weight). For composite materials, this yields an increase of the surface area of the reinforcing phase, and thus an increase of the region where stress transfer between the nanotube and matrix occurs. Thus, good interfacial bonding is important to guarantee adequate functionality of the composite [4, 5]. In spite of their great promises, several issues still hold the potential of carbon nanotubes as reinforcing agents for polymer composites, as stated in numerous studies [1, 2, 6, 7]. When such nanostructures are incorporated into a polymer matrix, the most important issues recognized are interfacial bonding with the matrix, adequate dispersion, and preservation of the CNT length [2, 6–11]. Given the dissimilar surface chemistry of CNTs and most polymer matrices, several attempts have been conducted to modify the surface of CNTs to improve their bonding to polymer matrices [4, 5, 12–14]. The general idea of these methods is to improve the CNT/polymer interfacial bonding by promoting chemical (covalent or non-covalent) interactions. In this regard, chemical functionalization (oxidation, amination, silanization, etc.) promotes the formation of functional groups at the nanotube surface, which may react with the functional groups of the organic polymer forming permanent bonds [4, 5, 15–17]. Among the most frequent functionalization techniques reported to improve mechanical properties of CNT-thermosetting polymer composites are oxidations [5, 15–18]

[*]Corresponding author, e-mail: faviles@cicy.mx

and amine based treatments [5, 13, 19, 20], while CNT silanization has been less reported in the open literature [21–25]. Although silane treatments are quite common for micron-size fiber-reinforced polymers, such treatments have not been thoroughly examined for CNTs. Pioneering efforts on CNT silanization for epoxy nanocomposites have been conducted by the groups of Ma and coworkers [22, 25] and Kathi and Rhee and coworkers [23, 24, 26]. Ma *et al.* [25] reported a three-step procedure to functionalize multi-wall carbon nanotubes (MWCNTs) based on oxidation by UV light, reduction with $LiAlH_4$ and finally nanotube silanization. The process presented by these authors successfully functionalized the surface of MWCNTs and improved the dispersion of the MWCNTs within an epoxy matrix and, consequently, the flexural properties of the composite. Recently, Kim *et al.* [26] conducted a functionalization procedure based on acid oxidation followed by silanization, and their results suggest slight improvements in the flexural properties of epoxy nanocomposites. To our knowledge, results for silanized CNT composites employing a vinyl ester thermosetting matrix (commonly used in resin infusion processes for composites manufacturing) have not been reported. Commercial CNTs commonly receive a proprietary purification treatment which frequently creates some functional groups on the CNT surface. The need of further oxidation previous to CNT silanization has also not being systematically addressed.

In this work, MWCNTs are chemically functionalized by three different methods: i) wet acid oxidation, ii) silanization of as-received nanotubes (without previous oxidation), iii) CNT silanization after acid and H_2O_2 oxidation. Elemental microanalysis and the presence of functional groups on the CNTs surface caused by oxidation and silanization are investigated by energy dispersive spectroscopy (EDX) and infrared spectroscopy (FT-IR), respectively. The functionalized MWCNTs are then employed to fabricate nanocomposites of vinyl ester resin, evaluating their compressive performance.

2. Materials and methods

2.1. Materials

CVD-grown MWCNT agglomerates were purchased from Bayer MaterialScience (Leverkusen, Germany) [27]. The nanotubes ('Baytubes C150P®') have an inner diameter of approximately 4 nm, outer mean diameter of 13–16 nm, and a typical length distribution between 1 and 4 μm. The as-purchased material has over 95% nanotube content with amorphous carbon and very small traces of metal catalyst as impurities. The resin employed was a Derakane 'Momentum 470-300®' epoxy vinyl ester resin from Ashland Composites (Covington, KY, USA) [28], which is typically used for resin infusion molding due to its low viscosity (styrene content 33 wt%). The initiator was Methyl Ethyl Ketone Peroxide (Norox MEKP-925, Syrgis, Helena, AR, USA) and Cobalt Naphthenate (CoNap) was used as promoter, both at 0.5 % w/w with respect to the weight of the vinyl ester resin. The silane coupling agent employed to functionalize the MWCNTs was 3-methacryloxypropyltrimethoxysilane (MPTMS), which is employed as a coupling agent for free radicals cured resins, such as vinyl esters. This silane has a methacrylate organo-reactive group and trimethoxy hydrolyzable groups, which matches the organofunctional group of the vinyl ester resin employed.

2.2. Nanotube oxidation and silanization

Chemical oxidation was carried out using a sequential treatment based on 3.0 M nitric acid followed by hydrogen peroxide (30% v/v). For the oxidative treatment, 0.3 g of the agglomerated MWCNTs were first mixed with 70 ml of HNO_3 and mechanically stirred in a stirring plate for 15 minutes. The mixture was then sonicated in an ultrasonic bath for 2 h, promoting CNT disentanglement within the acid solution. Then, the slurry was filtered, thoroughly washed with distilled water and the process repeated using H_2O_2. This mild oxidative process has been previously reported [29], and scanning electron micrographs did not show evidence of significant CNT damage.

Silanization was achieved by first dispersing 0.3 g of MWCNTs in ethanol (48 g) for 1 h using an ultrasonic bath. Simultaneously, 0.6 g of MPTMS were hydrolyzed by dissolution in 12 g of ethanol (J. T. Baker, analytic grade, 0.1% H_2O, Mallinckrodt Baker, Inc. Phillipsburg, NJ, USA) using a magnetic stirrer for 1 h at room temperature (28°C). Both solutions were then mixed in a sonicating bath for 1 h and mechanically stirred for 2 h at 60°C. Ethanol was then fully evaporated inside a vacuum

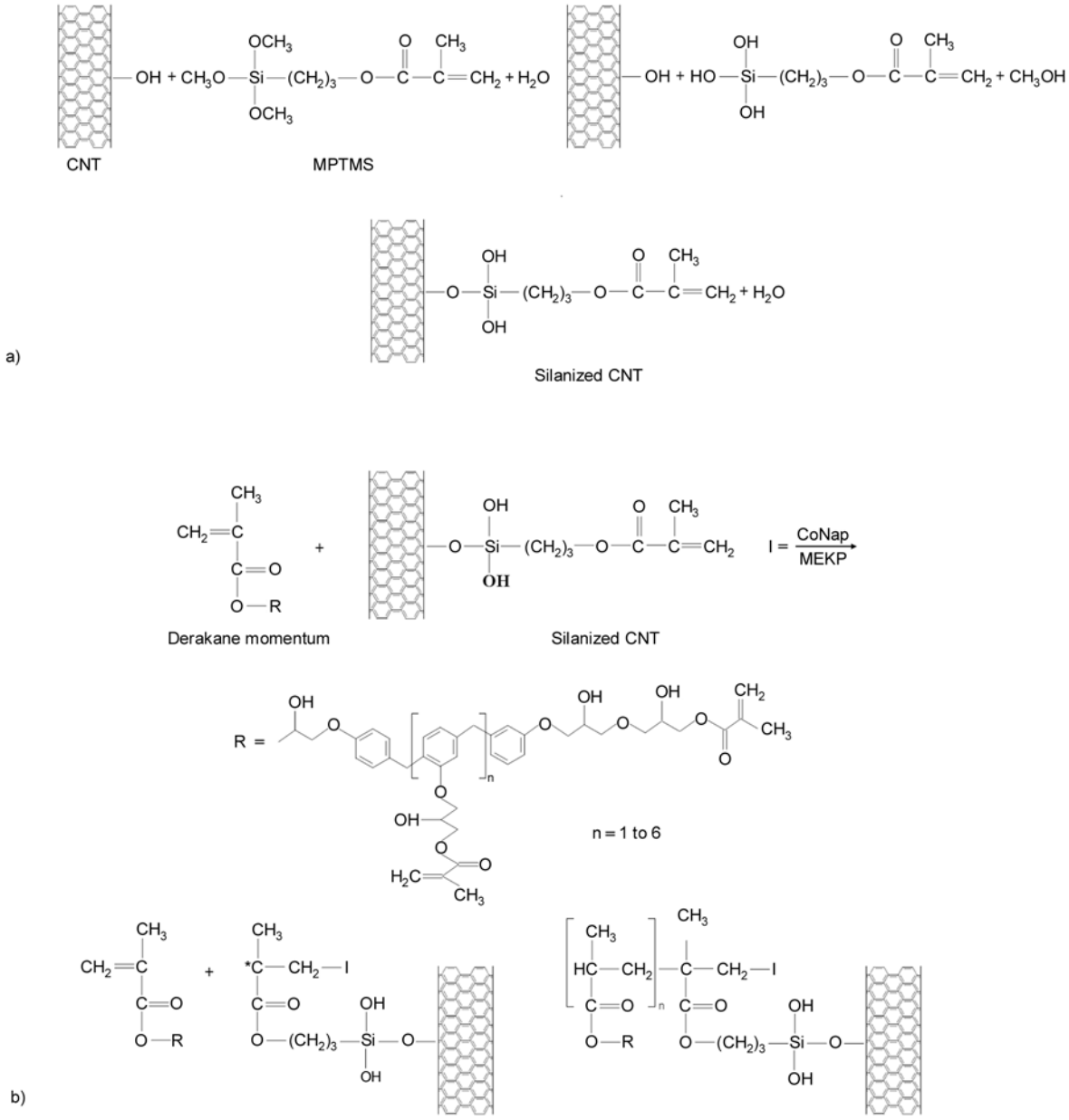

Figure 1. Schematic representation of CNT silanization and its bonding to the polymer matrix. a) CNT silanization with MPTMS, b) reaction of silanized CNT with the vinyl ester resin.

oven and MWCNTs were further dried at 150°C for 4 h to further improve condensation of silanol groups at the CNT surface. The silanized MWCNTs were intensively washed with ethanol, acetone and distilled water (sequentially) and dried in an oven at 150°C. Identical processes were employed to silanize the as-received MWCNTs and MWCNTs that had been previously oxidized as described above. Figure 1a depicts the chemical reactions occurring during silanization. Briefly, the oxidized surface contains hydrophilic hydroxyl groups (OH) that will serve as reaction sites. The silane coupling agent contains a trimethoxy group that after hydrolysis will also form hydroxyl groups. The hydroxyl groups on the CNT and silane will condense in order to attach covalently a methacrylate group (hydrophobic) on the surface. The methacrylate group, also an ester, matches the chemical structure of the vinyl ester matrix. Thus, the silane coupling agent is expected to act as a bridge at the interface between the carbon nanotube and the vinyl ester matrix.

2.3. Preparation of nanocomposites

Nanocomposites consisting of a vinyl ester resin loaded with 0.5% w/w MWCNTs were prepared using an ultrasonic-mechanical method to disperse the nanotubes within the resin. First, the desired amount of MWCNTs (0.2 g) was dispersed in acetone (40 g) for 2 h using an ultrasonic bath. The nanotubes/acetone solution was then mixed with the resin (40 g) and sonicated for 2 h in a cooled ultrasonic bath. The mixture MWCNTs/resin/acetone was then mechanically stirred in a hot plate until the acetone was evaporated. Since evaporation of styrene is also a possibility, the resin was initially weighted and gravimetric monitoring was conducted during the acetone evaporation process to maintain a constant amount of styrene in the resin, which was about 27 wt% for all specimens.

MWCNTs/resin mixtures were degassed under vacuum for approximately 1 h, and then mixed with 0.5% w/w CoNap and MEKP before casting into silicon moulds. Following this procedure, nanocomposites were prepared using as-received (AR) MWCNTs, as well as MWCNTs that were oxidized only (Ox), silanized without previous treatment (Sil), and silanized after the oxidative treatment (Ox-Sil). For reference, blank specimens of vinyl ester resin (VER) were also prepared following the same procedure as for nanocomposites. The specimens were molded as per the standard, requiring only polishing after casting. The nomenclature employed for the treatments and materials is listed in Table 1.

The possible chemical reaction occurring between the silanized MWCNT and vinyl ester resin is described in Figure 1b. The methacrylate groups on the silanized MWCNT will undergo free radical polymerization (initiated by the redox system CoNap/MEKP) in the presence of vinyl groups leading to a crosslinked network.

Table 1. Nomenclature of treatments/materials employed in this work

Material/treatment	Identification
Neat vinyl ester resin	VER
As-received MWCNTs	AR
Oxidized MWCNTs	Ox
Silanized MWCNTs without previous oxidation	Sil
Silanized MWCNTs after oxidation	Ox-Sil

2.4. Experimental characterization

The presence of silicon and new functional groups on the carbon nanotubes were assessed by microanalysis (EDX) and infrared spectroscopy (FT-IR). EDX/SEM analyses were carried out in a JEOL, JSM-6360-LV equipment coupled with an INCA Energy 200 detector (Oxford Instruments). For the EDX analysis, the MWCNT powder was affixed to a cooper support by means of a double-sided bonding copper tape. FT-IR spectra were obtained using KBr discs containing a very small amount of MWCNTs. The MWCNTs were first dispersed in acetone and a small drop added to the KBr powder. The KBr-MWCNTs powder was then diluted with additional KBr and analyzed several times, until a clear spectrum was obtained. The FT-IR analysis was conducted with a Nicolet-Protege 460 in the spectral range from 4000 to 600 cm^{-1}. Microanalysis and FT-IR spectra were obtained on each sample and the results presented correspond to the representative ones. An FEI-TITAN microscope (C_s = 1.25 mm) operated at 300 kV and registered near Scherzer focus was employed for transmission electron microscopy (TEM). TEM samples of treated and as-received MWCNTs were prepared on lacey carbon grids using dispersion in an ultrasonic bath for 30 minutes.

Axial compression of the composites and neat resin specimens was conducted in a Shimadzu AGI-100 universal testing machine, following ASTM standard D695 [30]. Compression specimens were prismatic with a length of 25.4 mm and square cross-sectional area of 12.7×12.7 mm^2. Cross head speed was 1 mm/min and eight replicates were used for each treatment.

3. Results and discussion

3.1. Functionalization of MWCNTs

EDX and FT-IR analyses were conducted in order to investigate the generation of oxygen containing species and attachment of silane molecules to MWCNTs. Table 2 presents the chemical composition of as-received (AR) MWCNTs, and nanotubes functionalized by oxidation only (Ox), silanization of the AR nanotubes (Sil), and silanization of the Ox nanotubes (Ox-Sil). It is observed that the AR nanotubes are mainly composed of carbon and oxy-

Table 2. EDX chemical composition (atomic %) of as-received and functionalized MWCNTs

Element	Treatment			
	AR	Ox	Sil	Ox-Sil
C	95.57	93.24	95.50	94.39
O	3.60	6.67	4.02	4.56
Si	–	–	0.06	0.89
Mg	0.21	–	0.10	–
Al	0.21	0.04	0.12	0.03
Mn	0.21	–	0.06	–
Co	0.21	0.02	0.06	–

– Not detected

gen, with a few metal impurities such as Mg, Al, Mn, and Co likely originated during the production or purification process. After oxidation with nitric acid and hydrogen peroxide (Ox), the great majority of the metal impurities are removed given the recognized action of HNO_3 as a purifying agent [15, 16, 18]. For this treatment, additional oxygen containing groups are introduced on the CNT surface, as indicated by the increase in oxygen content shown in Table 2. For the CNTs that are directly silanized from the AR material (Sil), the metal impurities contained in the AR material are not eliminated since the HNO_3 treatment was not conducted on these samples. The amount of oxygen in Sil samples is similar to that of the AR material and only a small amount of Si (0.06 atomic%) appears in the EDX quantification, suggesting that the covalent attachment of silane molecules may be marginal for this sample. However, when the CNTs are oxidized first and then silanized (Ox-Sil), the metal impurities almost disappear (because of the HNO_3 treatment) and a significant amount of Si (0.89 atomic%) is observed from the quantitative analysis. Therefore, these results suggest that silane molecules are better bonded to the CNT surface when an oxidative treatment is conducted before silanization. It is also noted that the oxygen content decreases for the Ox-Sil samples with respect to the Ox ones, which may be somewhat controversial. Although the MPTMS has five oxygen atoms (which should increase the oxygen content), the condensation of the silane with surface OH groups could cover the oxygen groups at the CNT surface, hindering their detection by EDX.

Figure 2 shows FT-IR spectra of the AR and functionalized CNTs examined in this work. For the as-received MWCNTs (Figure 2a) the IR spectrum shows important absorption bands at 3436 cm^{-1} (attributed to OH stretching), 2921 and 2860 cm^{-1} (asymmetric and symmetric CH_2 stretching), 1631 cm^{-1} (conjugated C=C stretching), and 1097 cm^{-1} (C-O stretch in alcohols). The presence of these functional groups implies that the as-received MWCNTs already have several functional groups that were introduced during the proprietary synthesis and/or purification processes. Thus, it could be possible that the hydroxy groups (OH) of the AR CNTs may react with the hydrolyzed silane during the silanization process, without demanding a previous oxidation step. When the CNTs are oxidized, Figure 2b, similar infrared absorptions remain although there are changes in their relative intensity in addition to new peaks of small intensity at 1714–1726 cm^{-1}, which may be assigned to stretching vibrations of carbonyl groups (C=O) due to carboxylic groups formed during the oxidation of hydroxyl compounds [29]. In addition to the presence of bands at 1726–1706 cm^{-1}, Ox-CNTs show a relative increase in the intensity of the hydroxyl groups with respect to the intensity of the CH band (3436 cm^{-1}) and C=C (1631 cm^{-1}) bands. A specific experiment was also conducted to guarantee that the increased intensity of the hydroxyl groups in the oxidized CNTs is not due to absorbed water. For this experiment, as-received MWCNTs were exposed to the laboratory environment for several weeks and the analysis was repeated, finding no further increase in the OH signal.

The CNTs that were oxidized and then silanized, Figure 2c, show distinctive absorption bands at 1160 and 655 cm^{-1}, characteristic of ≡Si–O–C≡ and Si–C (≡Si–CH_2) functional groups, respectively. To better visualize these bands, a 600–1200 cm^{-1} window of the Ox-Sil CNTs is included in Figure 2d. In addition to the bands at 1160 and 655 cm^{-1} discussed above, a weak band at 817 cm^{-1} associated to Si–OH is also appreciated in Figure 2d as expected from the hydrolysis of the MPTMS. It is worth mentioning that the ratio of intensities I_{OH}/I_{CH} in the Ox-Sil spectrum (Figure 2c) is lower than the corresponding I_{OH}/I_{CH} ratio obtained from the spectrum of the Ox sample (Figure 2b). The reduction of OH groups because of the subsequent silanization treatment may be associated to reaction of some of these groups with the hydrolyzed silane. The above observations confirm the covalent attachment of silane molecules to the CNT surface for the

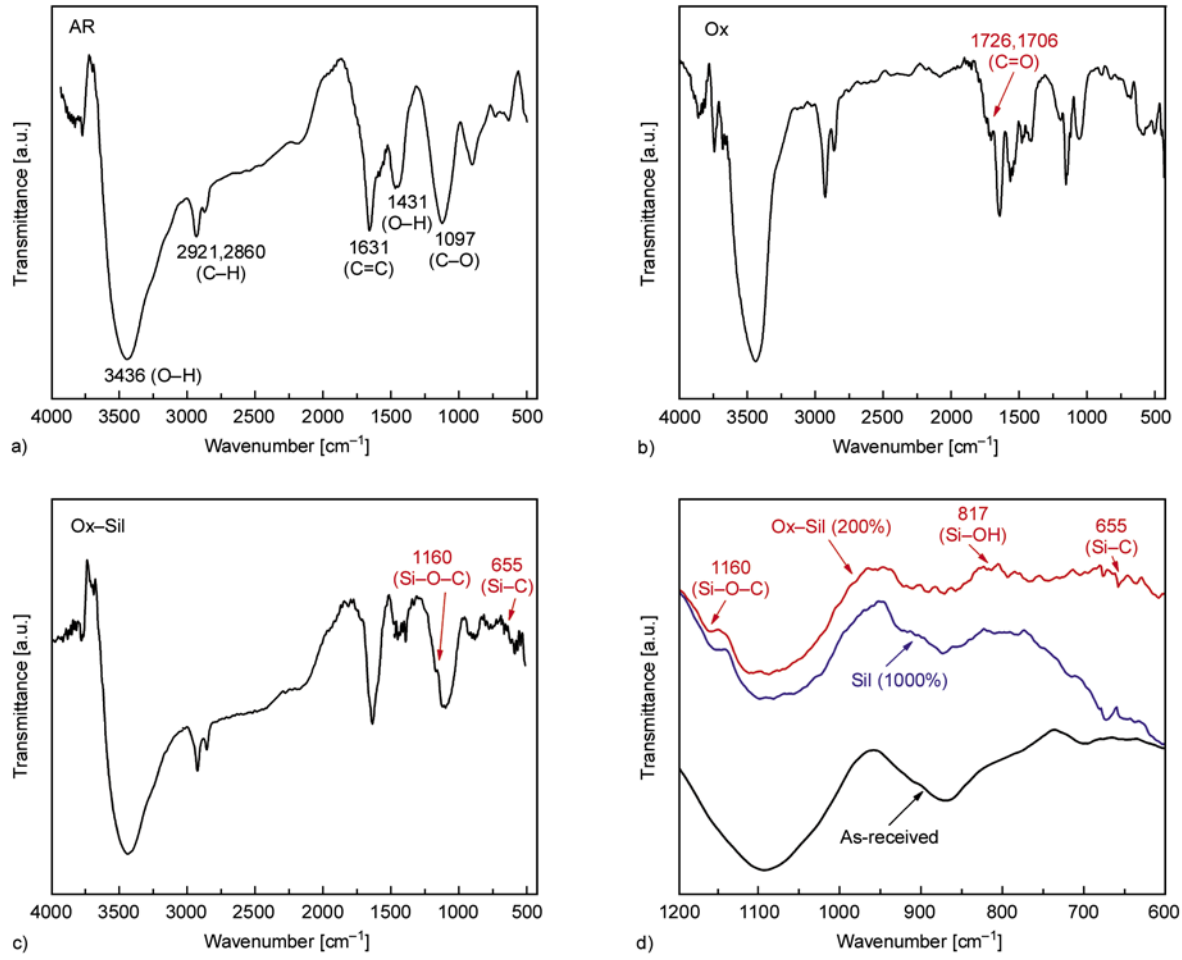

Figure 2. FT-IR spectra of MWCNTs. a) AR, b) Ox, c) Ox-Sil, d) 600–1200 cm^{-1} window of AR, Ox-Sil and Sil (1000 wt%).

Ox-Sil treatment in agreement with the EDX results. One may expect that also both vinyl (unsaturations) and carbonyl groups from the methacrylate were present but due to their low absorptivity, low concentration, or overlapping with existing groups, they were not detected.

On the other hand, for the nanotubes that were directly silanized from the as-received material (Sil) the absorption bands at 1160, 817 and 655 cm^{-1} (characteristic of attachment of silane molecules, see Figure 2c) were of very low intensity and hard to distinguish, which is related to the limited ability of the silane to bond to the non-oxidized CNT surface. Therefore, the IR spectrum of the original 'Sil' treatment (CNTs treated with 200 wt% of silane with respect to the weight of the CNTs) had no distinctive features and thus is not shown herein. Instead, Figure 2d shows the spectrum of CNTs directly silanized from the as-received material using a more concentrated silane solution (1000 wt%). At this high silane concentration, some of the distinctive bands identified in the spectrum of the Ox-Sil treatment are visible but let obvious than for the Ox-Sil treatment. The excess of silane, however, may form layers of polysiloxanes on the CNT surface. Therefore, the FT-IR and EDX analyses conducted here suggest that, although several functional groups are already present in the as-received MWCNTs, these groups are not sufficient to promote adequate silane attachment to the surface of the CNT. According to these results, efficient chemical bonding between the MWCNTs and silane molecules demands a previous oxidative treatment.

An important issue to address when functionalizing CNTs is the possibility of CNT damage during the functionalization process. In our work, the oxidative process conducted by the nitric acid may yield CNT damage. Figure 3 shows TEM images of as-received (AR), Figure 3a, oxidized (Ox), Figure 3b, and silanized MWCNTs that were previously oxi-

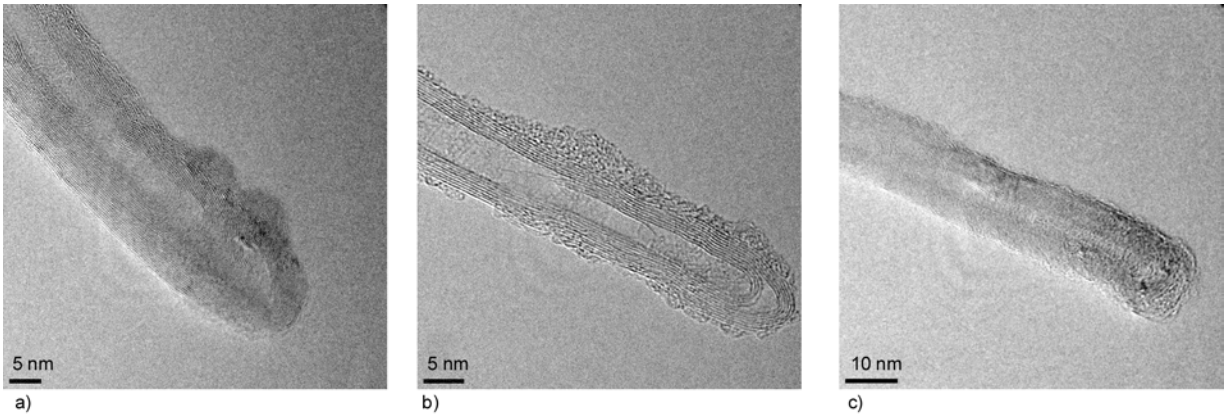

Figure 3. TEM morphology of as-received and functionalized MWCNTs. a) AR, b) Ox, c) Ox-Sil.

dized (Ox-Sil), Figure 3c. As shown in Figure 3a, the AR nanotubes are mostly capped with inner and outer diameters varying between 3.2–6.6 nm and 11–25.5 nm, in agreement with the information provided by the manufacturer [27]. The graphitic structure of the MWCNTs is composed of about 9–16 walls with an average separation between walls of 0.35 nm. Some amorphous carbon is observed at the outermost layers of the AR MWCNTs, likely yielded by the synthesis and/or (proprietary) purification processes. When these CNTs are oxidized, the basic graphitic structure and tubular geometry are preserved but some of the graphitic layers are etched by the action of the nitric acid, Figure 3b. The etching action of the oxidative treatment also caused stripping of some nanotube walls, with the consequent thinning of the nanotubes. The subsequent silanization process, Figure 3c, does not show evidence of further CNT damage beyond that produced by the oxidative treatment. Notice that a cap-open MWCNT is observed in Figure 3c. The defect generation and cap opening yielded by the oxidative process (although detrimental for the mechanical properties of the CNTs) should also yield more density of functional groups at those locations, and thus should favor the chemical reaction with the silane molecules and matrix bonding at these locations [5, 15, 18].

3.2. Mechanical characterization of nanocomposites

Nanocomposites consisting of vinyl ester resin (VER) and MWCNTs employing one of the treatments listed in Table 1 were tested in axial compression. The stress (σ)-strain (ε) compressive response of representative specimens is plotted in Figure 4. The representative specimens were chosen according to their similarity with the average measured properties, listed in Table 3. The neat vinyl ester resin specimens were labeled 'VER', and the rest of the nomenclature employed for the composites follows that assigned to the CNT treatments listed in Table 1. For all specimens examined, an initial linear behavior is observed up to $\varepsilon \sim 4\%$, where the onset of matrix yielding marks the initiation of nonlinear behavior, which continues up to specimen fracture. The nonlinear behavior observed is typical of thermosetting polymers under compression, which are normally highly linear and brittle in tension. To estimate the yield stress (σ_y), a 2% strain offset criteria was employed, calculating σ_y at the intersection of the 2% offset line with the σ-ε curve. The average and standard deviation values of strength (σ_{max}), yield stress, compressive elastic modulus (E), and ultimate strain (ε_{ult}), are listed in Table 3. Although overlapping of standard deviation (see Table 3) may compromise the strict

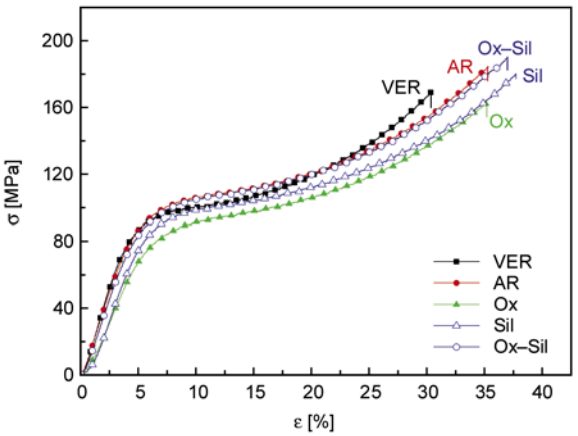

Figure 4. Compressive stress (σ)-strain (ε) curves representative of the MWCNT/VER nanocomposites examined

Table 3. Average and standard deviation compressive properties of MWCNT/VER nanocomposites

Material	σ_{max} [MPa]	σ_y [MPa]	E [GPa]	ε_{ult} [MPa]
VER	167.5±15.4	91.3±6.51	2.65±0.18	30.6±1.33
AR	183.3±11.2	97.6±1.63	2.53±0.11	35.3±2.02
Ox	163.2±8.82	86.6±2.25	2.34±0.09	33.9±1.83
Sil	183.9±14.2	96.9±5.75	2.51±0.19	36.6±1.79
Ox-Sil	186.4±11.6	98.8±3.48	2.54±0.10	36.7±1.18

statistical significance of the results, trends between the different treatments can be clearly observed. As observed from Figure 4 and Table 3, the composites containing MWCNTs that were only oxidized (Ox) showed lower properties than the rest of the composites. This may be attributed to the CNT damage generated during the oxidative process, see Fig. 3b. These flaws on the MWCNTs may serve as defect initiation sites and trigger CNT fragmentation during the process employed to fabricate the composite, reducing the effective MWCNT length in the final composite. This will be further examined in connection with SEM images of the composite fracture surfaces. Another distinctive trend in the compressive response of the composites is the improved mechanical properties obtained for the Ox-Sil composites. The improvements, however, are limited, and the reasons for these marginal improvements may be due to a competition of factors. On the one hand, the adequate bonding of the silane molecules to the CNT surface suggested for the Ox-Sil treatment (see section 3.1.) should promote stronger CNT-to-polymer interfacial bonding and hence improved mechanical properties of the composite. On the other hand, the pre-requisite of oxidation for the Ox-Sil treatment may lead to defective/shorter CNTs in the composite. These competing factors may lead to limited improvements in the mechanical properties of the composites.

Lastly, it is observed that the average mechanical properties of the composites containing CNTs that were silanized without previous oxidation (Sil) are slightly lower than those of the Ox-Sil composites. Although the difference is minor, the trend is again consistent with the FT-IR and EDX results presented in the previous section, which suggest poor bonding of the silane molecules to the CNTs for the Sil treatment.

To gain further insight into the mechanical response of the composites, fracture surfaces of the tested composites were investigated. Figure 5 shows SEM observations of the fracture surfaces of the examined composites. MWCNTs are observed as bright spaghetti-like cylinders (or 'dots') immersed in the (dark) polymer matrix. Overall, the dispersion of the nanotubes within the matrix is moderate with some agglomerates still visible. Agglomeration is more obvious in the non-treated samples, Figure 5a. To further improve dispersion would demand more energy input during the dispersion process but such high energy processes may also promote CNT damage and length shortening [10, 14, 31]. Figure 5a shows some AR nanotubes pulled out and lying longitudinally over the vinyl ester matrix. Pulling out of the AR CNTs is somewhat expected since they are not functionalized to promote bonding with the polymeric matrix. At this scale, it is difficult to assess a difference in the density of pull-outs observed in the Ox composites, Figure 5b, with respect to the AR ones, Figure 5a. However, a distinctive feature is observed for the composites fabricated with the Ox-Sil nanotubes, Figure 5d, which shows a higher density of bright dots which is indicative of broken CNTs (instead of being pulled-out). This finding suggests better interfacial bonding for the Ox-Sil composites, in agreement with the compression and FT-IR/EDX results discussed above.

An additional feature observed in all fracture surfaces of Figure 5 is the shorter length of the nanotubes with respect to its original length distribution. A detail transmission analysis of the as-received MWCNTs [32] yielded a length distribution of 1–4 μm. After composite processing (Figure 5), although an accurate length distribution is very difficult to assess, it is clear that the great majority of the CNTs are shorter than 1 μm. For the mild chemical treatments employed here, certain CNT damage may occur during the initial oxidative process [33], but the silanization process is not expect to yield severe structural damage or length shortening of the CNTs. However, in our case, even the composites manufactured with non-treated MWCNTs show significant length shortening, see Figure 5a. Fu *et al.* [10] recently pointed out that the brittleness of CNTs may cause significant reduction of the CNT length during processing of the composite, and such a length reduction can severely detriment the mechanical properties of the composite. Although existent theoretical models [9, 34, 35] present slight

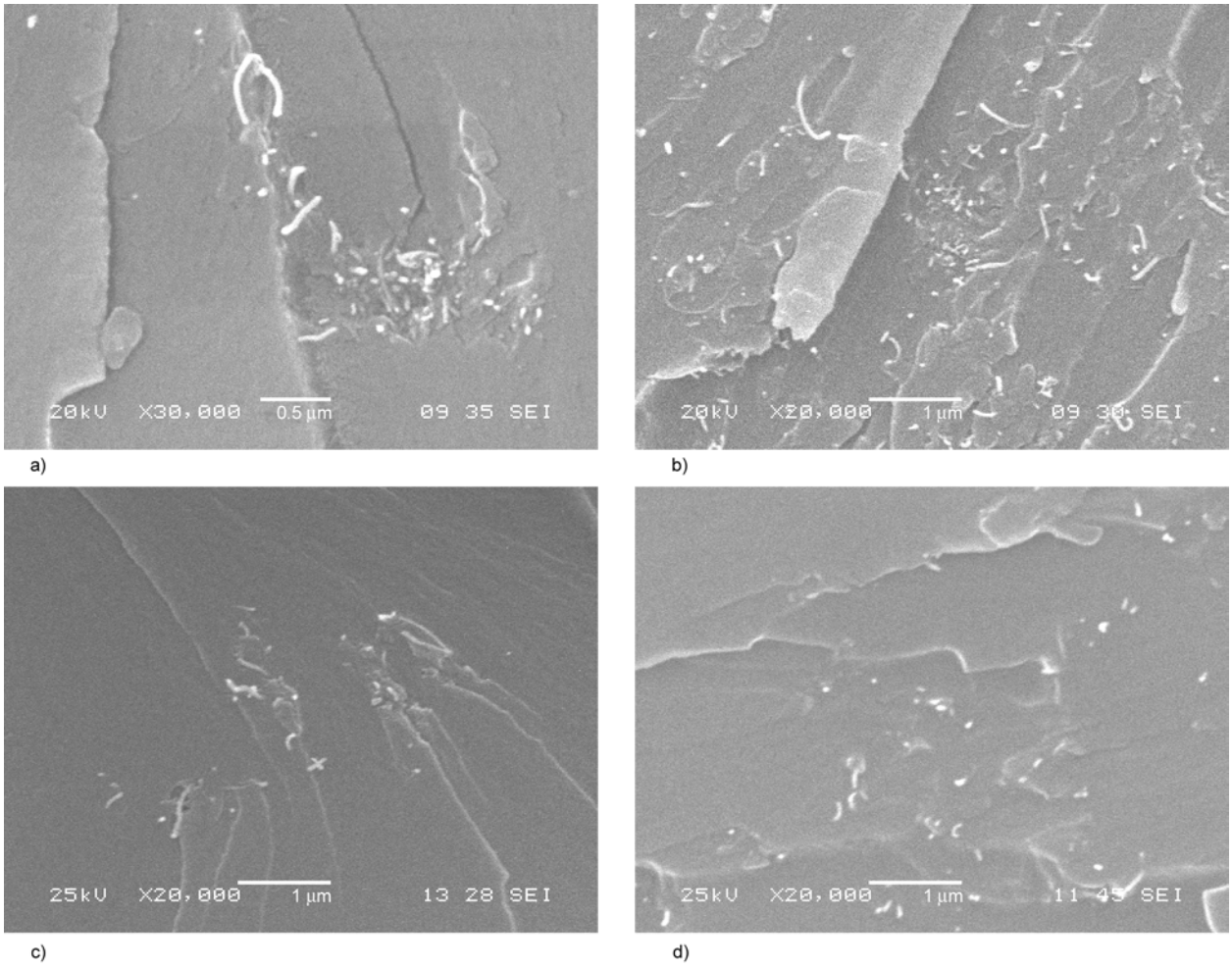

Figure 5. Fracture surface of MWCNT/VER nanocomposites examined by SEM. a) AR, b) Ox, c) Sil, d) Ox-Sil.

variations in the predicted critical aspect ratio (length/diameter) of the CNTs, the consensus (at least from the modeling input) seems to be that an aspect ratio of at least 100 is needed for adequate load transfer between the CNT and polymer matrix. In our case, considering a length distribution of 1–4 μm and a mean external diameter of 13 nm yields an aspect ratio of the pristine CNTs of 77–308, which is just above the critical aspect ratio allowed for adequate load transfer. Any shortening of the nanotubes, as evidenced by Figure 5, would greatly hamper the mechanical reinforcement effect of the CNTs in the polymer matrix.

4. Conclusions

Functionalization of multiwalled carbon nanotubes by acid oxidation and silanization was conducted. Two routes for MWCNT silanization were explored, a direct silanization of the as-received nanotubes without any previous treatment, and a method which involves oxidation and then silanization of the as-received CNTs. Even when the as-received CNTs have several functional groups originated during the synthesis (or purification), FT-IR and EDX analyses suggest better attachment of the silane molecules to the CNT when the nanotubes are previously oxidized. The better attachment of silane molecules to the CNTs for the sequential oxidation-silanization treatment correlates well with the improved compression properties of functionalized MWCNT/vinyl ester composites. Detailed TEM observations show evidence of slight CNT damage when the nanotubes are oxidized. When processing the composite, the initial CNT damage generated during functionalization is increased, causing CNT length shortening which limits the enhancement of the mechanical properties of the composite.

Acknowledgements

This work was supported by CONACyT (Mexico) Grant No. 79609, directed by Dr. Avilés. Technical assistance of Rossana Vargas (CICY) with SEM and FT-IR analysis is strongly appreciated. TEM analysis by Dr. Arturo Ponce and Gerardo Martínez at CIQA is also acknowledged.

References

[1] Thostenson E. T., Ren Z., Chou T-W.: Advances in the science and technology of carbon nanotubes and their composites: A review. Composites Science and Technology, **61**, 1899–1912 (2001). DOI: 10.1016/S0266-3538(01)00094-X

[2] Thostenson E. T., Li C., Chou T-W.: Nanocomposites in context. Composites Science and Technology, **65**, 491–516 (2005). DOI: 10.1016/j.compscitech.2004.11.003

[3] Tjong S. C.: Carbon nanotubes – Attractive nanofillers for forming bio-, functional and structural polymer composites. Express Polymer Letters, **4**, 516 (2010). DOI: 10.3144/expresspolymlett.2010.65

[4] Eitan A., Jiang K., Dukes D., Andrews R., Schadler L. S.: Surface modification of multiwalled carbon nanotubes: Toward the tailoring of the interface in polymer composites. Chemistry of Materials, **15**, 3198–3201 (2003). DOI: 10.1021/cm020975d

[5] Gojny F. H., Nastalczyk J., Roslaniec Z., Schulte K.: Surface modified multi-walled carbon nanotubes in CNT/epoxy-composites. Chemical Physics Letters, **370**, 820–824 (2003). DOI: 10.1016/S0009-2614(03)00187-8

[6] Lau K-T., Gu C., Hui D.: A critical review on nanotube and nanotube/nanoclay related polymer composite materials. Composites Part B: Engineering, **37**, 425–436 (2006). DOI: 10.1016/j.compositesb.2006.02.020

[7] Fiedler B., Gojny F. H., Wichman H. G. M., Nolte M. C. M., Schulte K.: Fundamental aspects of nano-reinforced composites. Composites Science and Technology, **66**, 3115–3125 (2006). DOI: 10.1016/j.compscitech.2005.01.014

[8] Xie X-L., Mai Y-W., Zhou X-P.: Dispersion and alignment of carbon nanotubes in polymer matrix: A review. Materials Science and Engineering R: Reports, **49**, 89–112 (2005). DOI: 10.1016/j.mser.2005.04.002

[9] Duncan R. K., Chen X. G., Bult J. B., Brinson L. C., Schadler L. S.: Measurement of the critical aspect ratio and interfacial shear strength in MWNT/polymer composites. Composites Science and Technology, **70**, 599–605 (2010). DOI: 10.1016/j.compscitech.2009.12.010

[10] Fu S-Y., Chen Z-K., Hong S., Han C. C.: The reduction of carbon nanotube (CNT) length during the manufacture of CNT/polymer composites and a method to simultaneously determine the resulting CNT and interfacial strengths. Carbon, **47**, 3192–3200 (2009). DOI: 10.1016/j.carbon.2009.07.028

[11] Gryshchuk O., Karger-Kocsis J., Thomann R., Kónya Z., Kiricsi I.: Multiwall carbon nanotube modified vinylester and vinylester – based hybrid resins. Composites Part A: Applied Science and Manufacturing, **37**, 1252–1259 (2006). DOI: 10.1016/j.compositesa.2005.09.003

[12] Gao Y., Wang Y., Shi J., Bai H., Song B.: Functionalized multi-walled carbon nanotubes improve non-isothermal crystallization of poly(ethylene terephthalate). Polymer Testing, **27**, 179–188 (2008). DOI: 10.1016/j.polymertesting.2007.09.012

[13] Shen J., Huang W., Wu L., Hu Y., Ye M.: Thermophysical properties of epoxy nanocomposites reinforced with amino-functionalized multi-walled carbon nanotubes. Composites Part A: Applied Science and Manufacturing, **38**, 1331–1336 (2007). DOI: 10.1016/j.compositesa.2006.10.012

[14] Chen H., Jacobs O., Wu W., Rüdiger G., Schädel B.: Effect of dispersion method on tribological properties of carbon nanotube reinforced epoxy resin composites. Polymer Testing, **26**, 351–360 (2007). DOI: 10.1016/j.polymertesting.2006.11.004

[15] Tasis D., Tagmatarchis N., Bianco A., Prato M.: Chemistry of carbon nanotubes. Chemical Reviews, **106**, 1105–1136 (2006). DOI: 10.1021/cr050569o

[16] Xing Y., Li L., Chusuei C. C., Hull R. V.: Sonochemical oxidation of multiwalled carbon nanotubes. Langmuir, **21**, 4185–4190 (2005). DOI: 10.1021/la047268e

[17] Zhu J., Kim J. D., Peng H., Margrave J. L., Khabashesku V. N., Barrera E. V.: Improving the dispersion and integration of single-walled carbon nanotubes in epoxy composites through functionalization. Nano Letters, **3**, 1107–1113 (2003). DOI: 10.1021/nl0342489

[18] Datsyuk V., Kalyva M., Papagelis K., Parthenios J., Tasis D., Siokou A., Kallitsis I., Galiotis C.: Chemical oxidation of multiwalled carbon nanotubes. Carbon, **46**, 833–840 (2008). DOI: 10.1016/j.carbon.2008.02.012

[19] Gojny F. H., Schulte K.: Functionalisation effect on the thermo-mechanical behaviour of multi-wall carbon nanotube/epoxy-composites. Composites Science and Technology, **64**, 2303–2308 (2004). DOI: 10.1016/j.compscitech.2004.01.024

[20] Seyhan A. T., Tanoglu M., Schulte K.: Tensile mechanical behavior and fracture toughness of MWCNT and DWCNT modified vinyl-ester/polyester hybrid nanocomposites produced by 3-roll milling. Materials Science and Engineering: A, **523**, 85–92 (2009). DOI: 10.1016/j.msea.2009.05.035

[21] Velasco-Santos C., Martínez-Hernández A. L., Lozada-Cassou M., Alvares Castillo A., Castaño V. M.: Chemical functionalization of carbon nanotubes through an organosilane. Nanotechnology, **13**, 495–498 (2002). DOI: 10.1088/0957-4484/13/4/311

[22] Ma P. C., Kim J-K., Tang B. Z.: Functionalization of carbon nanotubes using a silane coupling agent. Carbon, **44**, 3232–3238 (2006). DOI: 10.1016/j.carbon.2006.06.032

[23] Kathi J., Rhee K. Y.: Surface modification of multi-walled carbon nanotubes using 3-aminopropyltriethoxysilane. Journal of Materials Science, **43**, 33–37 (2008). DOI: 10.1007/s10853-007-2209-2

[24] Kathi J., Rhee K-Y., Lee J. H.: Effect of chemical functionalization of multi-walled carbon nanotubes with 3-aminopropyltriethoxysilane on mechanical and morphological properties of epoxy nanocomposites. Composites Part A: Applied Science and Manufacturing, **40**, 800–809 (2009). DOI: 10.1016/j.compositesa.2009.04.001

[25] Ma P. C., Kim J-K., Tang B. Z.: Effects of silane functionalization on the properties of carbon nanotube/epoxy nanocomposites. Composites Science and Technology, **67**, 2965–2972 (2007). DOI: 10.1016/j.compscitech.2007.05.006

[26] Kim H-C., Kim S-K., Kim J. T., Rhee K-Y., Kathi J.: The effect of different treatment methods of multi-walled carbon nanotubes on thermal and flexural properties of their epoxy nanocomposites. Journal of Polymer Science Part B: Polymer Physics, **48**, 1175–1184 (2010). DOI: 10.1002/polb.22007

[27] Bayer Material Science AG. Kaiser-Wilhelm-Allee 51368, Leverkusen, Germany. www.baytubes.com (2011).

[28] Ashland Performance Materials. 5200 Blazer Parkway, Dublin, Ohio, USA. www.derakane.com (2011).

[29] Avilés F., Cauich-Rodríguez J. V., Moo-Tah L., May-Pat A., Vargas-Coronado R.: Evaluation of mild acid oxidation treatments for MWCNT functionalization. Carbon, **47**, 2970–2975 (2009). DOI: 10.1016/j.carbon.2009.06.044

[30] ASTM D695: Standard test method for compressive properties of rigid plastics (2002).

[31] Lu K. L., Lago R. M., Chen Y. K., Green M. L. H., Harris P. J. F., Tsang S. C.: Mechanical damage of carbon nanotubes by ultrasound. Carbon, **34**, 814–816 (1996). DOI: 10.1016/0008-6223(96)89470-X

[32] Avilés F., Ponce A., Cauich-Rodriguez J. V., Martínez G. T.: TEM observations of MWCNTs oxidized by mild experimental conditions. Fullerenes, Nanotubes and Carbon Nanostructures, in press (2011).

[33] Hong C-E., Lee J-H., Kalappa P., Advani S. G.: Effects of oxidative conditions on properties of multi-walled carbon nanotubes in polymer nanocomposites. Composites Science and Technology, **67**, 1027–1034 (2007). DOI: 10.1016/j.compscitech.2006.06.003

[34] Haque A., Ramassety A.: Theoretical study of stress transfer in carbon nanotube reinforced polymer matrix composite. Composite Structures, **71**, 68–77 (2005). DOI: 10.1016/j.compstruct.2004.09.029

[35] Wan H., Delale F., Shen L.: Effect of CNT length and CNT-matrix interphase in carbon nanotube (CNT) reinforced composites. Mechanics Research Communications, **32**, 481–489 (2005). DOI: 10.1016/j.mechrescom.2004.10.011

eXPRESS Polymer Letters Vol.5, No.9 (2011) 777–787
Available online at www.expresspolymlett.com
DOI: 10.3144/expresspolymlett.2011.76

Micro-structural evolution of rubber/clay nanocomposites with vulcanization process

Y-L. Lu[1,2,3], *F-Y. Ye*[1], *L-X. Mao*[1], *Y. Li*[1], *L-Q. Zhang*[1,2,3*]

[1]Key Laboratory of Beijing City on Preparation and Processing of Novel Polymer Materials, College of Polymer Science and Engineering, Beijing University of Chemical Technology, Beijing 100029, PR China
[2]Key Laboratory of Carbon Fiber and Functional Polymers, Ministry of Education, College of Polymer Science and Engineering, Beijing University of Chemical Technology, Beijing 100029, PR China
[3]Key Laboratory for Nanomaterials, Ministry of Education, College of Polymer Science and Engineering, Beijing University of Chemical Technology, Beijing 100029, PR China

Received 31 December 2010; accepted in revised form 10 March 2011

Abstract. Brominated isobutyl-isoprene rubber/clay nanocomposite (BIIRCN) and ethylene-propylene-diene-monomer rubber/clay nanocomposite (EPDMCN) were prepared by melt blending. The micro-structural evolution of these two kinds of rubber/clay nanocomposites (RCNs) with vulcanization process was investigated using wide-angle X-ray diffraction (WAXD) and transmission electron microscope (TEM). The WAXD results revealed that the intercalated structure of organically modified clay (OMC) changed throughout the whole curing process. The intercalated structure kept on changing beyond the vulcanization stage of T_{90}. The interlayer space of intercalated silicate in uncured BIIRCN is larger than that in uncured EPDMCN. However, the intercalated structure for EPDMCN changed by a larger extent than that for BIIRCN during the vulcanization process, and the interlayer space of the intercalated structure is larger in the cured EPDMCN than that in the cured BIIRCN. It was found that the intercalant (i.e., octadecylamine, ODA) for OMC could shorten the scorch time of the curing reaction, and increase the curing rate, which was attributed to the further intercalation during vulcanization. TEM results indicated that the spatial distribution of OMC is much better in BIIR (a polar rubber matrix) than that in EPDM (a non-polar rubber matrix). The changes in spatial dispersion structure during vulcanization for EPDMCN and BIIRCN show different trends. In conclusion, the polarity of the rubber is the determining factor influencing the evolution of both the intercalated structure and the spatial dispersion of clay during vulcanization.

Keywords: *nanocomposites, organoclay, vulcanization, intercalated structure, spatial distribution*

1. Introduction

In recent years, rubber/clay nanocomposites (RCNs) have become a research focus because of their high strength, gas barrier, and flame resistance. Up to date, four processing methods, including *in-situ* polymerization intercalation [1], solution intercalation [2], melt intercalation [3–5], and latex compounding [6–8], have been developed for preparation of RCNs. Among them, melt compounding is the most practical method, because existing rubber processing equipment can be used and no organic solvent is needed.

The dispersion state of organically modified clay (OMC) in the rubber matrix determines the final properties of the composite. There are many factors that impact the microstructure of RCNs prepared by melt compounding. Previous studies have shown that the type of intercalant [9–12], the compounding conditions (shear stress and temperature) [13, 14], as well as the polarity of the rubber [15] have sig-

*Corresponding author, e-mail: zhanglq@mail.buct.edu.cn

nificant impact on the dispersion state of OMC in the rubber matrix. In addition, significant changes in the microstructure of RCNs also occur during the curing process at high temperature and high pressure [16–18]. However, there is still some fuzziness in the mechanism and reasons for this change in clay dispersion during the curing process until now. In particular, the microstructural evolution of RCNs with the vulcanization course has not been reported. In the present work, brominated isobutyl-isoprene rubber/clay nanocomposites (BIIRCN) and ethylene propylene diene monomer rubber/clay nanocomposites (EPDMCN) were prepared by melt intercalation, and the evolution of both intercalation structure and spatial dispersion of clay layers in these two kinds of RCNs during vulcanization process was studied. We observed some unexpected phenomenon that might have provided us with a new idea to prepare well-dispersed rubber/clay nanocomposites. At the same time, the role of intercalants and the polarity of matrix rubber on microstructure evolution were discussed.

2. Experimental

2.1. Materials and basic formulation

Brominated isobutyl-isoprene rubber (BIIR, 2030) with the Br content of 2.0±0.3%, the unsaturation degree of ~1.95% and the Mooney viscosity ($ML_{1+8}^{125°C}$) of 32±4 was produced by Bayer, Germany. Ethylene propylene diene monomer rubber (EPDM, 4050) with ethylene content of 52%, ethylidene norbornene (ENB) content of 6.7 g/100 g, and the $ML_{1+4}^{100°C}$ of ~45 was provided by Jilin Petrochemical Company, China. The organically modified clay (OMC, I.30P) with an initial basal spacing of 2.36 nm was purchased from Nanocor, USA. Pristine sodium montmorillonite (Na-MMT) was supplied by Liufangzi Mining Co. Ltd, Siping City, Jilin Providence, China. Other materials and agents were commercial products. In order to obtain organic intercalant (i.e., octadecylamine, ODA) from the OMC (I.30P), some amounts of OMC were subjected to 48 h Soxhlet extraction at 95°C with anhydrous ethanol. The residual extraction solution of ethanol was evaporated at 100°C. The obtained substance was pestled and dried to obtain ODA. The formulations for rubber compounds used in this work are listed in Table 1.

2.2. Preparation of samples

The rubber and OMC (or, Na-MMT and ODA) were first compounded uniformly on a two-roll mill (Zhanjiang Rubber and Plastic Machinery Factory, China) according to the formulation given in Table 1, and the other agents were gradually mixed into the compound.

Besides BIIRCN and EPDMCN, the neat BIIR and EPDM containing MMT or ODA compounds were also prepared according to the formulation given in Table 1, in order to analyse the influence of OMC on vulcanization course of matrix. The rubber compounds were prepared by a 6 inch two-roll mill blending in the following addition order of the ingredients: the EPDM → ZnO → SA → additive. In this study, we used OMC, MMT, and ODA as fillers for EPDM in the amounts of 10, 7, and 3 phr, respectively.

The vulcanization curves of the rubber compounds at 150°C were examined by using a disc oscillating rheometer (P3555B2, Beijing Huanfeng Chemical Technology and Experimental Machine Plant, China). Figure 1 shows the curing curves of BIIRCN and EPDMCN at 150°C. The curing times for different curing stages, T_i (i.e., T_{10}, T_{20}, … T_{90}, T_{100}),

Table 1. Formulations for rubber compounds

Materials	Loading [phr[a]]				
	BIIRCN	EPDMCN	EPDM	E-ODA	E-MMT
BIIR	100	–	–	–	–
EPDM	–	100	100	100	100
Organoclay (OMC)	10	10	–	–	–
ODA	–	–	–	3	–
Na-MMT	–	–	–	–	7
Zinc oxide (ZnO)	5.0	5.0	5.0	5.0	5.0
Stearic acid (SA)	2.0	2.0	2.0	2.0	2.0
Tetramethyl thiuram disulfide (accelerator TMTD)	1.0	1.0	1.0	1.0	1.0
2-Mercapto benzothiazole (accelerator M)	0.5	0.5	0.5	0.5	0.5
Sulfur (S)	1.8	1.8	1.8	1.8	1.8

[a]phr is the abbreviation of parts per hundreds of rubber

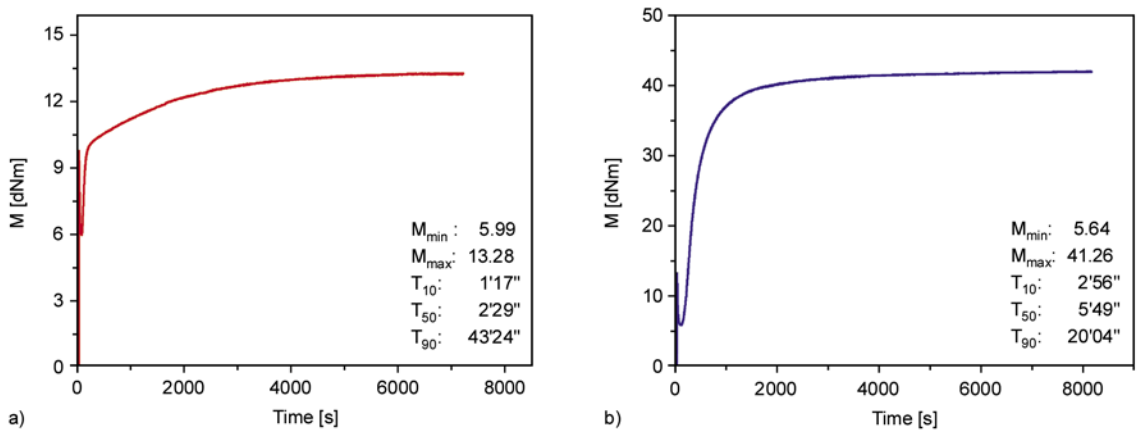

Figure 1. Curing curves at 150°C of (a) BIIRCN and (b) EPDMCN

Table 2. Curing times for different cure stages of BIIRCN and EPDMCN at 150°C

Cure stage	Cure time [s]	
	BIIRCN	EPDMCN
T_0	0	0
T_{10}	77	176
T_{20}	88	216
T_{30}	100	252
T_{40}	117	295
T_{50}	149	349
T_{60}	348	423
T_{70}	875	536
T_{80}	1549	733
T_{90}	2604	1204
T_{100}	6889	8070

were calculated as following procedure: (1) the difference between the maximum torque (M_{max}) and the minimum torque (M_{min}) of the curing curves, $\Delta M = M_{max} - M_{min}$, was calculated; (2) the torques at various curing stages (M_i) were calculated from the equation, $M_i = M_{min} + \Delta M \cdot i\%$, e.g., $M_{10} = M_{min} + \Delta M \cdot 10\%$, $M_{20} = M_{min} + \Delta M \cdot 20\%$, … $M_{90} = M_{min} + \Delta M \cdot 90\%$; and (3) the cure time (T_i) corresponding to M_i was obtained from the vulcanization curve. The resultant curing time for BIIRCN and EPDMCN at different vulcanization stages are summarized in Table 2.

The RCNs were vulcanized by a plate vulcanizing press (25 tons, Shanghai Rubber Machinery Factory, China) to the time for different curing stages (T_i) at 150°C and 15 MPa. The vulcanized specimens have the dimension of 132 mm × 112 mm × 1 mm. The samples were promptly removed from the mold when the curing time reached predetermined T_i, and then rapidly quenched in cold water to stop the curing reaction. We denoted the BIIRCN and EPDMCN nanocomposites whose curing stage is at T_i as BIIR-T_i and EPDM-T_i, respectively. The uncured samples, BIIR-T_0 and EPDM-T_0, were prepared by filling the mold with BIIRCN and EPDMCN compounds, respectively, and then pressed at 60°C and 15 MPa for 30 min and finally for another 30 min at room temperature.

2.3. Characterization

WAXD measurements were carried out on a RINT diffractometer (D/max-IIIC, Rigaku Corporation, Japan) with a Cu-K_α radiation (40 kV, 200 mA) in the 2θ range of 0.5 to 10° at a scan rate of 1°/min. The spatial dispersion state of OMC in the rubber matrix was observed on a transmission electron microscope (TEM) (H-800, Hitachi, Japan) with an acceleration voltage of 200 kV. Ultra-thin sections of RCNs were cut by using a microtome at –100°C for the TEM experiments.

3. Results and discussion

3.1. The evolution of intercalated structure of rubber/clay nanocomposites during curing process

Wide-angle X-ray diffraction (WAXD) is a very useful tool for the study of polymer/clay nanocomposites. It can directly determine the intercalation of polymer molecules in the silicate gallery. Figure 2 displays the WAXD patterns of BIIRCN and EPDMCN at different curing stages. It can be seen that there are the main diffraction peaks corresponding to the basal spacing of 3.90 or 3.25 nm in the WAXD patterns of BIIR-T_0 and EPDM-T_0 (uncured samples), respectively, while the original gallery height of OMC (I.30P) is 2.36 nm, indicating that nanocomposites with an intercalated structure have

been obtained by melt blending. BIIR is a polar rubber with a Br content of 1.8%, while EPDM is a non-polar rubber. According to the theory of polymer melt intercalation [19, 20], the higher the polarity of the polymer the higher the interaction between the polymer molecules and clay layers, facilitating intercalation of polymer chains into inter space of the silicate.

In the wide-angle X-ray diffraction (WAXD) analysis, the gallery height of the clay is calculated by the Bragg equation, Equation (1):

$$2d\sin\theta = n\lambda,\ n = 1, 2, 3, \ldots \quad (1)$$

where d is the interplanar spacing; 2θ is the diffraction angle or Bragg angle; n is the order of the diffracted beam; and λ is the wavelength of the radiation. Because of the lower order degree of OMC, the width of the basal diffraction peak (001) is relatively large and the high order diffraction peaks offset to a certain degree; and as a result the d values of the high order diffraction peaks and basal diffraction peak are just approximate multiples. For example, aside from the basal diffraction peak located at 3.90 nm, the reflection peaks at 1.93 and 1.28 nm with descending intensity were observed in the WAXD pattern of uncured BIIRCN, and these two reflection peaks have the relationship of approximate multiples with the main diffraction peak. Therefore, we attribute these two diffraction peaks (i.e., (002) and (003)) to the high order diffraction peak of basal one (001). Similarly, other EPDMCN samples at different curing stages (T_{10}, T_{20}, etc.) also show such high order diffraction peaks. These results indicate that the intercalated structure of clay in the rubber matrix have relative high order degree. As the curing reaction proceeds, the basal diffraction (001) peaks for both of BIIRCN and EPDMCN undergo an obvious change. The interlayer spaces (D_{001}) corresponding to main diffraction peaks for cured BIIRCN and EPDMCN were significantly higher than those for uncured nanocomposites (i.e., T_0 samples), indicating further intercalation of rubber molecules during the curing process.

In previous reports [16], it was speculated that the microstructure of RCN could change only during the initial period of the curing course, when the viscosity of the system is still relatively low. However, our results show that even beyond the curing stage of T_{90}, the intercalated structure of clay still changes apparently with increasing curing time. At the curing time of T_{90}, the vast majority of rubber chains have formed a three-dimensional network structure by chemical crosslinking, but the crosslinking density is not high, generally in the range of 10^{-4} to 10^{-5} mol/cm^3. There are the segments of rubber

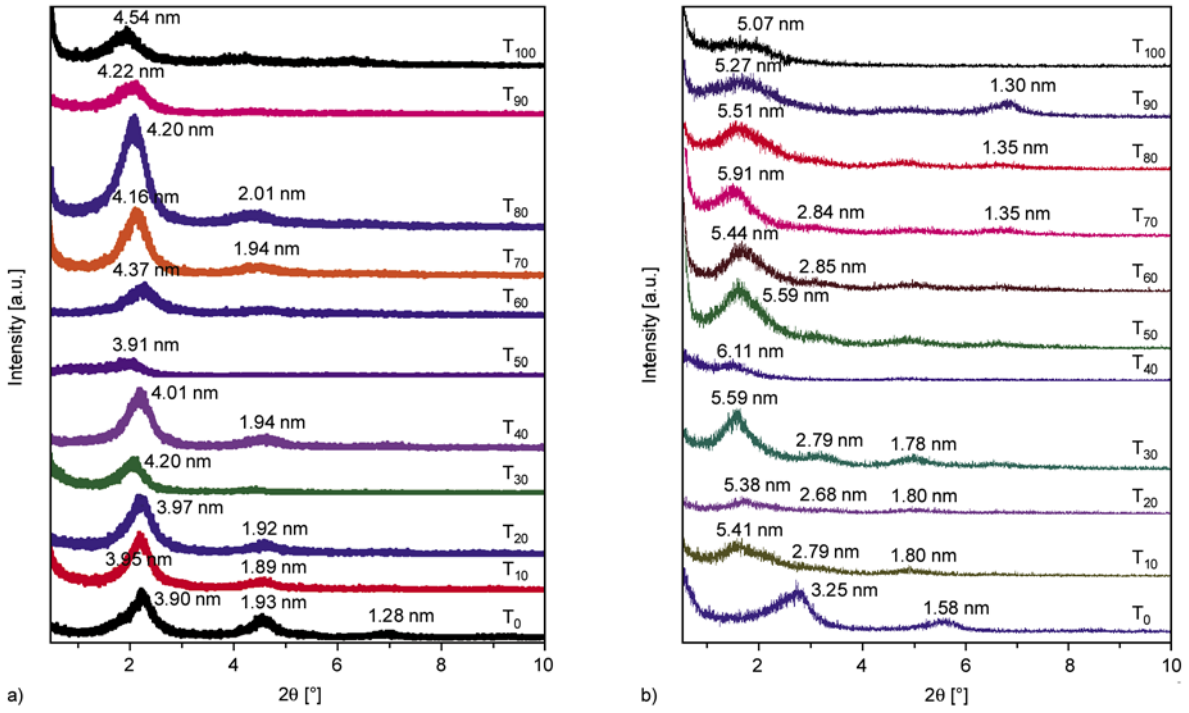

Figure 2. WAXD patterns of (a) BIIRCN and (b) EPDMCN at different curing stages. All curves were shifted vertically for clarity.

chains having dozens of or even hundreds of repeating units between cross-linking sites, which still maintain a high mobility. The high temperature of the curing process further enhances the activity of the molecular segments. Consequently, significant changes in the intercalated structure of are still possible at the later stages of the curing course.

Aside from the (001) reflection peak, the higher order reflection peaks can be observed in the WAXD patterns of some BIIRCNs and EPDMCNs at different curing stages. The appearance of these high order diffraction peaks indicates that the intercalated structure of the clay could maintain relatively high order degree, though the interlayer space undergone large changes during the vulcanization course. In the WAXD patterns of some EPDMCNs at later curing stages of T_{70}, T_{80} and T_{90}, except for the main diffraction peak at low angles, the small diffraction peaks at high angles, corresponding to ~1.30 nm were observed. They are not the higher order reflection peaks of the main diffraction peak because of the large deviations from integral multiples of the main diffraction peak. The interlayer space of ~1.30 nm is significantly smaller than the initial interlayer space (2.36 nm) of OMC (I.30P), but is close to that for inorganic clay. These results show that collapse of the intercalated structure also occurred during the curing process of EPDMCN [21], even formed some inorganic clay.

To further study the changes in intercalated structure during the curing reaction, we plotted the variation of the relative D_{001} values (normalized to the D_{001} values for the uncured samples at T_0) of OMC with the curing stage, as shown in Figure 3. For both BIIRCN and EPDMCN, the interlayer space of OMC changes significantly in the initial few seconds of the curing reaction, i.e., it increases first, reaches a maximum at a certain curing time, and then decreases. The basal interlayer spacing (D_{001}) gradually increases in BIIRCN, but decreases in EPDMCN during the latter period of the curing course. Previous studies showed that the vulcanization reaction can make rubber molecules intercalate into the silicate gallery, increasing the interlayer space [22], but the vulcanization reaction can also facilitate the de-intercalation of intercalants, resulting in collapse of the intercalated structure–the reduction of interlayer space [21]. High pressure during the curing process would 'squeeze out' the rubber molecules that had been intercalated

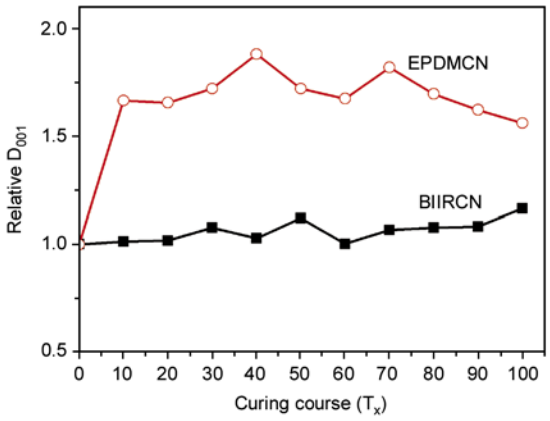

Figure 3. The evolution of relative basal spacing (D_{001}) of intercalated silicate structure with curing course. The relative D_{001} is the ratio of D_{001} for the sample at T_x curing stage to that at T_0 curing stage, and D_{001} for T_0 sample was set as one.

into the clay layers [23], thus reducing the interlayer space. We believe that all these effects are present and compete with each other during the curing process, leading to the complex phenomenon of changes in intercalated structure with increasing curing time. Further studies are still needed to establish the specific mechanisms involved. Another noteworthy phenomenon is that the basal interlayer space (D_{001}) of the intercalated structure is 4.54 nm after vulcanization in the polar BIIR, significantly less than the corresponding value of 5.23 nm in the non-polar EPDM.

We can draw the conclusion that the change in D_{001} value is much larger in the non-polar EPDM system than in the polar BIIR system. In the polar BIIR system, the change in D_{001} value is less than 10%, while the increase in D_{001} value is over 80% in the non-polar EPDM system.

3.2. Effects of OMC on the curing process

The influence of OMC on vulcanization reactions was believed to be an important factor affecting the microstructural change of RCNs during vulcanization. Most previous studies about the vulcanization kinetic of RCNs indicted that addition of OMC would considerably increase curing rate and cross-linking density of various rubber compounds, including NR [24, 25], ENR [26], BR [27, 28], SBR [29], EAR [30], NBR [31], and NBR/SBR blend [32]. On the other hand, some studies [12, 33] on EPDM/OMC systems shown that addition of OMC prolonged the optimum curing time and reduced the

cross-linking density of the composites. As shown by above experimental results, the intercalated structure of clay in the EPDMCN had changed much more intensively than that in the BIIRCN during the curing process. In this work, therefore, the EPDM system was selected as an example to discuss the effect of OMC on curing process.

The vulcanization curves presented in Figure 4 and the corresponding curing parameters given in Table 3 show the effect of the intercalant (i.e., ODA), pristine clay (i.e., Na-MMT) and OMC on the curing reaction of EPDM. Compared with the neat EPDM compound, addition of Na-MMT shortened the scorch time (T_{10}), but obviously reduced the CRI, indicating that Na-MMT could suppress curing reactions. On the other hand, the addition of ODA not only shortened the scorch time of EPDM by more than 60%, but also increased the curing rate by about 12%, suggesting that ODA could accelerate curing reactions. The OMC is comprised of Na-MMT and ODA, so that the effects of OMC on vulcanization kinetic should be the combination of the effects of ODA. As shown in Table 3, EPDMCN exhibits reduced T_{10} compared to net EPDM, and the middle value of CRI between those for E-ODA and E-MMT compounds. In addition, the CRI of EPDMCN is closer to that for E-MMT, and smaller than that of net EPDM.

The inner part of the OMC interlayer is enriched with ODA molecules, which can promote the curing reaction. Therefore, the crosslinking rate of the rubber intercalated into the silicate gallery is expected to be obviously higher than that of the rubber outside the layers. For chemical equilibrium, a large number of rubber molecular chains outside

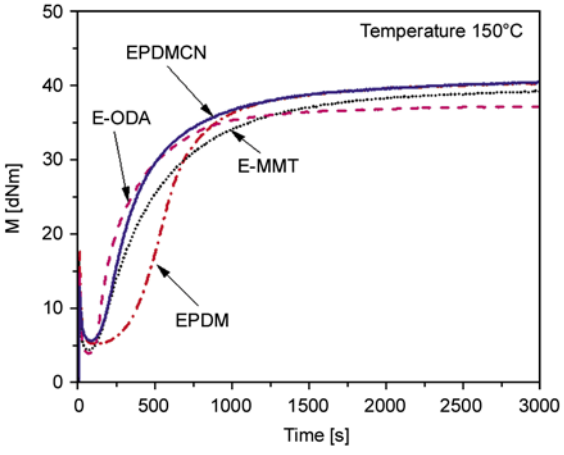

Figure 4. Curing curves of different EPDM compounds with sulfur vulcanization system under 150°C

Table 3. Curing parameters of different EPDM compounds with sulfur vulcanization system

Samples	Curing parameter					
	T_{10} [min]	T_{90} [min]	CRI[a] [min^{-1}]	M_{max} [dNm]	M_{min} [dNm]	ΔM[b] [dNm]
EPDM	5.73	17.83	8.26	40.35	5.21	35.14
E-MMT	2.68	20.88	5.49	39.45	4.38	35.07
E-ODA	2.15	12.98	9.23	37.54	3.91	33.53
EPDMCN	2.93	20.07	5.83	41.26	5.64	35.62

[a]CRI is abbreviation of curing rate index, defined as $100/(T_{90} - T_{10})$.
[b]ΔM is the difference between M_{max} and M_{min}.

the layers would be driven to further intercalate into the silicate gallery, participating in the crosslinking reaction in the interlayer of OMC and expanding the interlayer spacing of the OMC. It has been reported [21] that ODA can react with curing agents to form intermediate compounds. These compounds may migrate into the rubber matrix to take part in the vulcanization process, thus the intercalants would be extracted from the clay galleries, with a resultant confinement and even deintercalation. For the EPDMCN at later period of vulcanization course in this study, the similar phenomenon has also been observed (see Figure 2).

As shown in Figure 1, EPDMCN has higher curing rate (i.e., smaller value of T_{90}–T_{10}) and higher cross-linking density (i.e., higher value of $M_{max} - M_{min}$) than BIIRCN, though they have the same compound recipes (see Table 1), likely due to relatively high unsaturated degree of EPDM. Therefore, the cross-linking reactions in EPDMCN should be more intense than those in BIIRCN. Thus the driving force for further intercalation of rubber molecules into silicate gallery or the collapse of intercalated structure caused by de-adsorption of intercalant would be greater in EPDMCN. As a result, the interlayer spacing of intercalated silicate in EPDMCN changed with vulcanization course larger and more violently, also resulting in some collapsed structures. In our previous studies on IIRCNs [17], we also found that when curing reaction is more severe by raising the curing temperature, more collapses structure would be generated in the cured nanocomposites.

3.3. The evolution of spatial dispersion of organically modified clay during the curing process

Transmission electron microscopy (TEM) is an effective means to observe the morphology and

spatial dispersion of nano-clay in rubber matrix. TEM images of BIIRCNs and EPDMCNs at the representative curing times of T_0, T_{10}, T_{50}, and T_{100} were displayed in Figure 5 and 6 to reflect the changes in spatial dispersion of clay in the matrix during the entire curing process. In these figures, the lighter phase and the darker lines or phase represent the rubber matrix and OMC, respectively.

Figure 5 shows that the dispersion of clay is uniform in BIIR-T_0 (uncured BIIRCN). BIIR-T_0 contains the least amount of clay aggregates, and the size of the aggregates was the smallest (about 20 nm in thickness and 500 nm in length). The amount of clay aggregates increases significantly in BIIR-T_{10}. The dispersion state of the clay deteriorates with increasing curing time. The amount and size of clay aggregates continue to increase in BIIR-T_{50} and BIIR-T_{100}, with local appearances of micron-level aggregates.

In the curing process of EPDMCN, the evolution of clay dispersion is slightly different from that of BIIRCN. As shown in Figure 6, the clay exists in the form of granules, and large aggregates appear in EPDM-T_0 (uncured EPDMCN). The dispersion state of clay improved markedly in EPDM-T_{10}. The clay exists largely as fine filaments 10 nm in thickness and 160 nm in length. After T_{10}, the dispersion state deteriorates gradually. Flocculating aggregates are formed by a large number of crystal lamellas in EPDM-T_{50}, and the dispersion becomes non-uniform. In EPDM-T_{100}, the dispersion degree of clay continues to decrease, with the appearance of large flocculating clay aggregates.

Our previous study on IIRCN [16] revealed that the effect of high pressure on microstructure exhibit time dependence–subjecting to high pressure for short time would not cause obvious change in the microstructure of the nanocomposite. The result

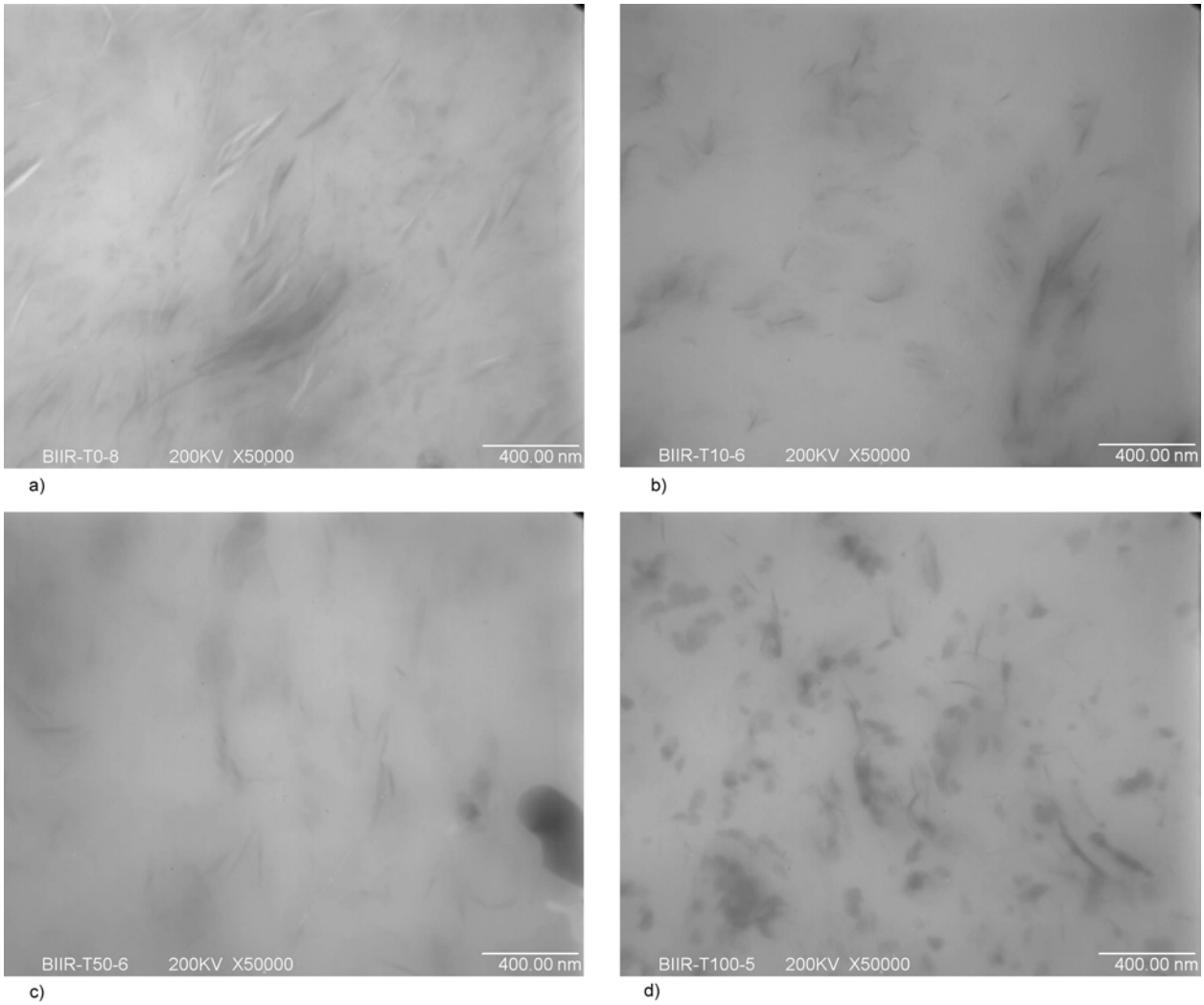

Figure 5. TEM images of BIIRCN at various curing stages (×50 000): (a) T_0, (b) T_{10}, (c) T_{50} and (d) T_{100}

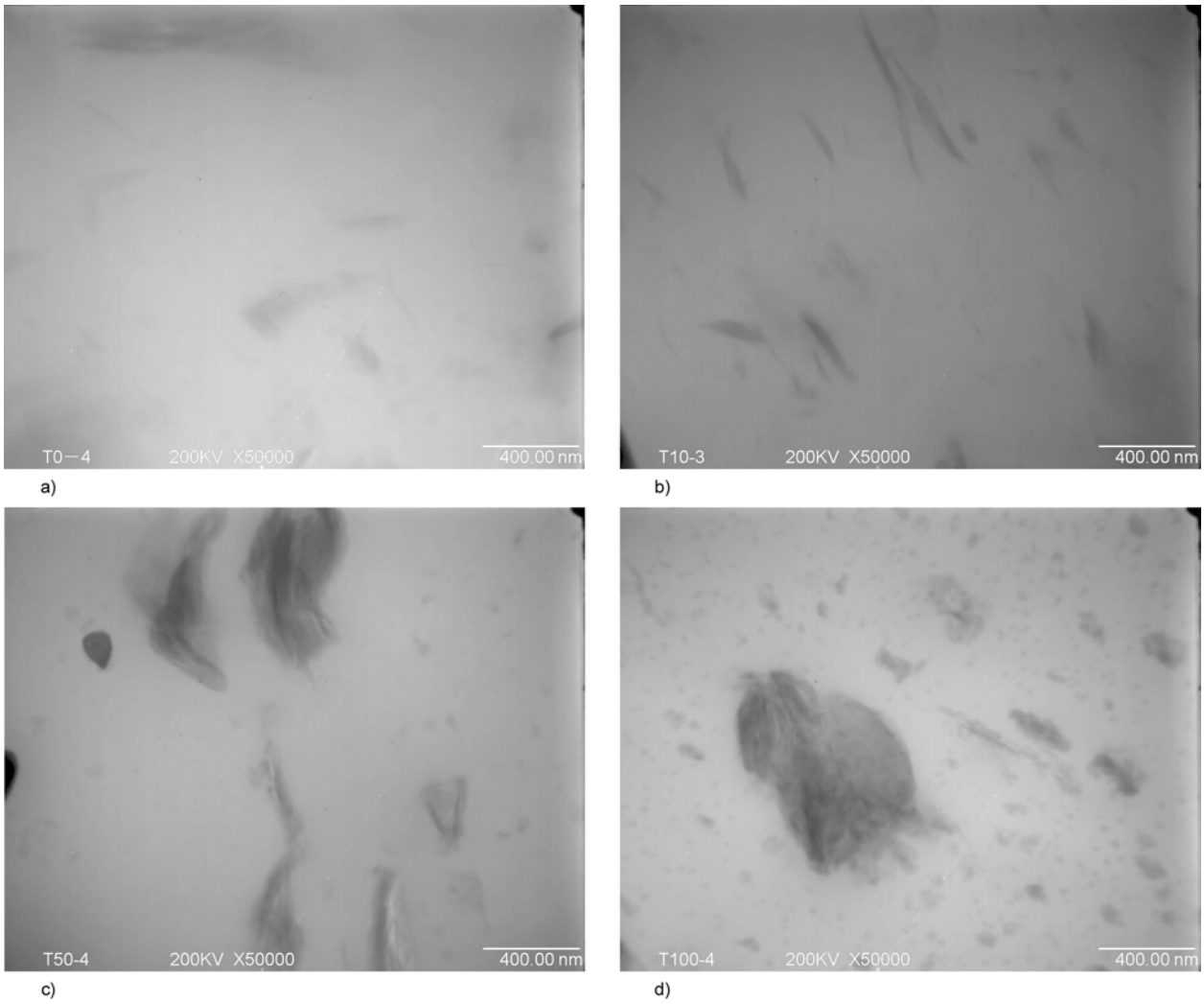

Figure 6. TEM images of EPDMCN at various curing stages (×50 000): (a) T_0, (b) T_{10}, (c) T_{50} and (d) T_{100}

shown in Figure 6 suggests that such time dependence for high pressure effect also exists in EPDMCN. As a result, in the initial stage of vulcanization (i.e., before T_{10}), curing reaction plays a major role on dispersion state of clay, which can drive rubber molecules further intercalate into the silicate gallery and improve the spatial dispersion of clay. On the other hand, with the time for subjecting to high pressure increasing (i.e., in the later stage of vulcanization), the effect of high pressure becomes more and more considerable, generating large flocculates of intercalated silicate, though the interlayer spacing of which is larger than that in uncured nanocomposite.

In comparison of TEM morphology between BIIRCN and EPDMCN (Figure 5 and 6), the spatial dispersion of OMC in EPDMCN is clearly inferior to that in BIIRCN. WAXD results (Figure 2) show the interlayer space of the intercalated structure in cured EPDMCN is obviously larger than that in cured BIIRCN. These results suggested that the intercalated clay with the larger interlayer space does not necessarily result in the better spatial dispersion.

3.4. Impact of the polarity of rubber on the microstructure of rubber/clay nanocomposite

The above results demonstrate that the RCNs with different polarity show different change trends in both the intercalated structure and spatial dispersion of clay during the vulcanization process. The interlayer space of BIIR-T_0 is larger than that of EPDM-T_0, while the interlayer space of cured EPDMCN is larger than that of cured BIIRCN and more variable during the curing process. The spatial dispersion of the OMC is obviously better in the polar BIIR than in the non-polar EPDM. The spatial dispersion dete-

riorates continuously with curing time in BIIRCN, while it improves from T_0 to T_{10} before worsening with further increasing in curing time in EPDMCN. The vulcanization curves of BIIRCN and EPDMCN given in Figure 1 reveal that the torque difference (i.e., $M_{max} - M_{min}$) of EPDMCN is significantly higher than that of BIIRCN, and the optimum curing time (i.e., T_{90}) of the EPDMCN is significantly shorter than that of the BIIRCN, indicating that both the crosslink density of the cured EPDM and its curing rate are much larger than those for the BIIRCN. If only the factor of the mobility of dispersed clay layers in RCNs during vulcanization process were considered, the microstructural changes for EPDMCN would be smaller than those BIIRCN. However, the experimental results show that the opposite fact is true, suggesting that the polarity of matrix rubber might be a more significant factor on the microstructural change than other factors.

Using the polarity of rubber as the starting point, we present a preliminary explanation of the phenomena disclosed in this study on base of the kinetics and thermodynamics of the intercalation of polymer chain into layered silicate. According to the theory on melt polymer intercalation [19, 20], the polymer molecules with high polarity have strong interaction with the clay, and this strong interaction can offset some of the entropy decrease caused by confinement of intercalated polymer chains. From the point of view of thermodynamics, the intercalation of polymer with high polarity easily results in the intercalated structure with a larger gallery height. The intercalation of polymer molecules into the silicate gallery is a continuous process of destruction and reconstruction of the interaction between the molecules and the clay. The polar rubber macromolecules have stronger interaction with OMC than non-polar macromolecules, and this stronger interaction is more difficult to be destroyed. From the point of view of kinetics, therefore, the energy barrier against intercalation for polar rubber is higher than that for nonpolar rubber. In the process of mechanical blending rubber with OMC, the strong external shear force can destroy the energy barrier for intercalation, thus facilitating the intercalation process. At this time, the thermodynamic factor should play dominant role in determining the intercalation structure. As a result, the intercalated structure in BIIRCN mixing compound exhibits larger interlayer spacing than that in EPDMCN mixing compound. Accordingly, the spatial dispersion state of OMC in BIIRCN mixing compound is much better than that in EPDMCN. On the contrary, different from the process of mechanical mixing, there is a lack of external strong shear force during the vulcanization process to overcome the energy barrier against intercalation, so kinetics factors play a greater role in further intercalation. EPDM rubber molecules have lower intermolecular forces with clay than BIIR molecules, so the energy barrier for the destruction of the original structure to form the new intercalated structure is smaller for EPDM system than in BIIR system, resulting in a larger interlayer spacing of the intercalated structure in cured EPDMCN than in cured BIIRCN. Accordingly, the change in spatial dispersion state of OMC during vulcanization process in EPDMCN is more intensively than that in BIIRCN.

4. Conclusions

(a) The intercalated structure of clay continuously changed throughout the curing process, and such micro-structural changes could occur even after the curing time had reached T_{90}. The intercalants ODA of organoclay could shorten the scorch time, and increase the curing rate, so the impact of intercalants on vulcanization kinetic was considered to be primary cause for the evolution of intercalated structure.

(b) Of the two uncured RCNs, uncured BIIRCN has a larger interlayer spacing of the intercalated structure than uncured EPDMC. However, the opposite is true in the cured RCNs. The change in intercalated structure during vulcanization is larger in EPDMCN than in BIIRCN. The spatial dispersion of clay in BIIR, a polar rubber, is superior to that in EPDM, a non-polar rubber. During the vulcanization process, the spatial dispersion state of clay in BIIRCN gradually deteriorates. In the case of EPDMCN, the spatial dispersion of clay increased from T_0 to T_{10}, followed by gradual deterioration with curing time.

(c) For BIIRCN and EPDMCN, sulfur-curing reactions can cause further intercalation and increase the interlayer space, but also possibly result in collapse of intercalated structure. High pressure has negative effects on the dispersion of clay. These factors coexist and compete with each other during

vulcanization course, leading to complex microstructural evolution behavior. The difference in microstructural evolution during vulcanization between BIIRCN and EPDMCN is interpreted from the viewpoints of thermodynamics and kinetics, and the polarity of the rubber matrix is expected to play a major role.

(d) This work shows that the dispersion state of rubber/clay nanocomposites obtained by the current conventional vulcanization process is not the best. For instance, the dispersion state of clay in EPDMCN is the best at a certain intermediate stage of the curing process, showing the potential for improving the clay dispersion through the optimization of curing parameters. Our previous work [23] has demonstrated that the curing under low pressure can obtain RCN with better dispersion. However, high pressure is necessary for many rubber products in order to adequately fill the mould with complex shape, improve product compactness, and reduce defects. We suggested that performing vulcanization of RCNs under altered pressure, that is using high pressure at the beginning stage but reducing pressure at latter stage, may obtain the RCN with good dispersion, the work on which is still ongoing.

Acknowledgements

This work was financially supported by New Star Program of Beijing Science and Technology (2006A15), National Outstanding Youth Science Fund (contract grant number: 50725310) and Program for Changjiang Scholars and Innovative Research Team in University (PCSIRT, IRT0807).

References

[1] Zhang Z., Zhang L., Li Y., Xu H.: New fabricate of styrene–butadiene rubber/montmorillonite nanocomposites by anionic polymerization. Polymer, **46**, 129–136 (2005).
DOI: 10.1016/j.polymer.2004.11.008

[2] Pramanik M., Srivastava S. K., Samantaray B. K., Bhowmick A. K.: Rubber–clay nanocomposite by solution blending. Journal of Applied Polymer Science, **87**, 2216–2220 (2003).
DOI: 10.1002/app.11475

[3] Hasegawa N., Okamoto H., Kawasumi M., Kato M., Tsukigase A., Usuki A.: Polyolefin-clay hybrids based on modified polyolefins and organophilic clay. Macromolecular Materials and Engineering, **280/281**, 76–79 (2000).
DOI: 10.1002/1439-2054(20000801)280:1<76::aid-mame76>3.0.co;2-#

[4] Varghese S., Karger-Kocsis J., Gatos K. G.: Melt compounded epoxidized natural rubber/layered silicate nanocomposites: Structure-properties relationships. Polymer, **44**, 3977–3983 (2003).
DOI: 10.1016/S0032-3861(03)00358-6

[5] Ramorino G., Bignotti F., Pandini S., Riccò T.: Mechanical reinforcement in natural rubber/organoclay nanocomposites. Composites Science and Technology, **69**, 1206–1211 (2009).
DOI: 10.1016/j.compscitech.2009.02.023

[6] Varghese S., Karger-Kocsis J.: Natural rubber-based nanocomposites by latex compounding with layered silicates. Polymer, **44**, 4921–4927 (2003).
DOI: 10.1016/S0032-3861(03)00480-4

[7] Wu Y-P., Jia Q-X., Yu D-S., Zhang L-Q.: Structure and properties of nitrile rubber (NBR)–clay nanocomposites by co-coagulating NBR latex and clay aqueous suspension. Journal of Applied Polymer Science, **89**, 3855–3858 (2003).
DOI: 10.1002/app.12568

[8] Wu Y-P., Zhang L-Q., Wang Y-Q., Liang Y., Yu D-S.: Structure of carboxylated acrylonitrile-butadiene rubber (CNBR)–clay nanocomposites by co-coagulating rubber latex and clay aqueous suspension. Journal of Applied Polymer Science, **82**, 2842–2848 (2001).
DOI: 10.1002/app.2138

[9] Varghese S., Karger-Kocsis J.: Melt-compounded natural rubber nanocomposites with pristine and organophilic layered silicates of natural and synthetic origin. Journal of Applied Polymer Science, **91**, 813–819 (2004).
DOI: 10.1002/app.13173

[10] Kim J-T., Oh T-S., Lee D-H.: Morphology and rheological properties of nanocomposites based on nitrile rubber and organophilic layered silicates. Polymer International, **52**, 1203–1208 (2003).
DOI: 10.1002/pi.1249

[11] Kim J-T., Oh T-S., Lee D-H.: Preparation and characteristics of nitrile rubber (NBR) nanocomposites based on organophilic layered clay. Polymer International, **52**, 1058–1063 (2003).
DOI: 10.1002/pi.1110

[12] Zheng H., Zhang Y., Peng Z., Zhang Y.: Influence of clay modification on the structure and mechanical properties of EPDM/montmorillonite nanocomposites. Polymer Testing, **23**, 217–223 (2004).
DOI: 10.1016/S0142-9418(03)00097-7

[13] Schön F., Thomann R., Gronski W.: Shear controlled morphology of rubber/organoclay nanocomposites and dynamic mechanical analysis. Macromolecular Symposia, **189**, 105–110 (2002).
DOI: 10.1002/masy.200290000

[14] Gatos K. G., Thomann R., Karger-Kocsis J.: Characteristics of ethylene propylene diene monomer rubber/organoclay nanocomposites resulting from different processing conditions and formulations. Polymer International, **53**, 1191–1197 (2004).
DOI: 10.1002/pi.1556

[15] Sadhu S., Bhowmick A. K.: Preparation and properties of nanocomposites based on acrylonitrile–butadiene rubber, styrene–butadiene rubber, and polybutadiene rubber. Journal of Polymer Science Part B: Polymer Physics, **42**, 1573–1585 (2004).
DOI: 10.1002/polb.20036

[16] Liang Y-R., Ma J., Lu Y-L., Wu Y-P., Zhang L-Q., Mai Y-W.: Effects of heat and pressure on intercalation structures of isobutylene-isoprene rubber/clay nanocomposites. I. Prepared by melt blending. Journal of Polymer Science Part B: Polymer Physics, **43**, 2653–2664 (2005).
DOI: 10.1002/polb.20555

[17] Lu Y-L., Li Z., Mao L-X., Li Y., Wu Y-P., Liang Y-R., Zhang L-Q.: Impact of curing temperature on microstructures and properties of isobutylene–isoprene rubber/clay nanocomposites. Journal of Applied Polymer Science, **110**, 1034–1042 (2008).
DOI: 10.1002/app.28690

[18] Lu Y-L., Liang Y-R., Wu Y-P., Zhang L-Q.: Effects of heat and pressure on microstructures of isobutylene-isoprene rubber (IIR)/clay nanocomposites. Macromolecular Materials and Engineering, **291**, 27–36 (2006).
DOI: 10.1002/mame.200500319

[19] Vaia R. A., Giannelis E. P.: Polymer melt intercalation in organically-modified layered silicates: Model predictions and experiment. Macromolecules, **30**, 8000–8009 (1997).
DOI: 10.1021/ma9603488

[20] Vaia R. A., Jandt K. D., Kramer E. J., Giannelis E. P.: Kinetics of polymer melt intercalation. Macromolecules, **28**, 8080–8085 (1995).
DOI: 10.1021/ma00128a016

[21] Gatos K. G., Karger-Kocsis J.: Effects of primary and quaternary amine intercalants on the organoclay dispersion in a sulfur-cured EPDM rubber. Polymer, **46**, 3069–3076 (2005).
DOI: 10.1016/j.polymer.2005.01.095

[22] Usuki A., Tukigase A., Kato M.: Preparation and properties of EPDM–clay hybrids. Polymer, **43**, 2185–2189 (2002).
DOI: 10.1016/S0032-3861(02)00013-7

[23] Liang Y-R., Lu Y-L., Wu Y-P., Ma Y., Zhang L-Q.: Pressure, the critical factor governing final microstructures of cured rubber/clay nanocomposites. Macromolecular Rapid Communications, **26**, 926–931 (2005).
DOI: 10.1002/marc.200500077

[24] Arroyo M., López-Manchado M. A., Herrero B.: Organo-montmorillonite as substitute of carbon black in natural rubber compounds. Polymer, **44**, 2447–2453 (2003).
DOI: 10.1016/S0032-3861(03)00090-9

[25] López-Manchado M. A., Arroyo M., Herrero B., Biagiotti J.: Vulcanization kinetics of natural rubber–organoclay nanocomposites. Journal of Applied Polymer Science, **89**, 1–15 (2003).
DOI: 10.1002/app.12082

[26] Teh P. L., Mohd Ishak Z. A., Hashim A. S., Karger-Kocsis J., Ishiaku U. S.: Effects of epoxidized natural rubber as a compatibilizer in melt compounded natural rubber–organoclay nanocomposites. European Polymer Journal, **40**, 2513–2521 (2004).
DOI: 10.1016/j.eurpolymj.2004.06.025

[27] Kim M-S., Kim D-W., Chowdhury S. R., Kim G-H.: Melt-compounded butadiene rubber nanocomposites with improved mechanical properties and abrasion resistance. Journal of Applied Polymer Science, **102**, 2062–2066 (2006).
DOI: 10.1002/app.23738

[28] Kim M-S., Kim G-H., Chowdhury S. R.: Polybutadiene rubber/organoclay nanocomposites: Effect of organoclay with various modifier concentrations on the vulcanization behavior and mechanical properties. Polymer Engineering and Science, **47**, 308–313 (2007).
DOI: 10.1002/pen.20709

[29] Mousa A., Karger-Kocsis J.: Rheological and thermodynamical behavior of styrene/butadiene rubber-organoclay nanocomposites. Macromolecular Materials and Engineering, **286**, 260–266 (2001).
DOI: 10.1002/1439-2054(20010401)286:4<260::AID-MAME260>3.0.CO;2-X

[30] Mathew G., Rhee J. M., Lee Y-S., Park D. H., Nah C.: Cure kinetics of ethylene acrylate rubber/clay nanocomposites. Journal of Industrial and Engineering Chemistry, **14**, 60–65 (2008).
DOI: 10.1016/j.jiec.2007.07.001

[31] Choi D., Kader M. A., Cho B-H., Huh Y-I., Nah C.: Vulcanization kinetics of nitrile rubber/layered clay nanocomposites. Journal of Applied Polymer Science, **98**, 1688–1696 (2005).
DOI: 10.1002/app.22341

[32] Essawy H., El-Nashar D.: The use of montmorillonite as a reinforcing and compatibilizing filler for NBR/SBR rubber blend. Polymer Testing, **23**, 803–807 (2004).
DOI: 10.1016/j.polymertesting.2004.03.003

[33] Ma Y., Wu Y-P., Wang Y-Q., Zhang L-Q.: Structure and properties of organoclay/EPDM nanocomposites: Influence of ethylene contents. Journal of Applied Polymer Science, **99**, 914–919 (2006).
DOI: 10.1002/app.22247

eXPRESS Polymer Letters Vol.5, No.9 (2011) 788–798
Available online at www.expresspolymlett.com
DOI: 10.3144/expresspolymlett.2011.77

Sterilization of propylene/ethylene random copolymers: Annealing effects on crystalline structure and transparency as influenced by polymer structure and nucleation

M. Gahleitner[1,], C. Grein[1], R. Blell[2], J. Wolfschwenger[1] , T. Koch[3], E. Ingolic[4]*

[1]Borealis Polyolefine GmbH, Innovation Headquarters Linz, St. Peterstr. 25, 4021 Linz, Austria
[2]Institut Charles Sadron, UPR22, CNRS-ULP, 6 rue Boussingault, 67083 Strasbourg, France
[3]Vienna University of Technology, Institute of Materials Science and Technology, Favoritenstraße 9-11, 1040 Vienna, Austria
[4]Institute for Electron Microscopy, Graz University of Technology, Steyrergasse 17, 8010 Graz, Austria

Received 5 January 2011; accepted in revised form 11 March 2011

Abstract. An extensive investigation of three different series of isotactic ethylene/propylene (EP) random copolymers was performed to understand the factors influencing the change in optical properties in the steam sterilization of extrusion cast films from such materials. Different analytical methods (differential scanning calorimetry (DSC), X-ray diffraction and electron microscopy) were employed to elucidate structural changes determining film optics, and in addition to the polymer structure parameters also nucleation and processing effects were studied. The findings clearly show that a combination of homogeneously randomized comonomer distribution and nucleation can partly inhibit lamellar thickening in sterilization, thus preserving high transparency even after a heat treatment. In detail, attention has to be paid to the combined effects of primary and secondary post-crystallization, which both are affected by the chain regularity.

Keywords: *processing technologies, material testing, polypropylene, crystallization, optical properties*

1. Introduction

Extrusion cast film, a major application area for polypropylene (PP), requires an excellent combination of mechanical and optical properties. Apart from homopolymers, ethylene-propylene (EP) random copolymers are the most important materials for this segment, taking advantage of their remarkable see-through performance. The good optical quality is a result of their slower crystallization speed compared to standard isotactic PP (iPP) resulting in less crystallinity and a finer crystal structure [1]. A growing fraction of this segment is subjected to pasteurization or sterilization processes, like in medical applications or food packaging. Radiation sterilization by γ-radiation or electron beam (β-radiation) which is a normal and well established technology for polyethylene (PE) has been found to be critical for PP as it induces radical degradation processes and leads to massive toughness losses [2].

But also in steam sterilization which has been found to be generally suitable for PP, the mechanical and optical consequences of such a treatment must be considered in material design already [3], basically requiring an understanding of physical ageing and post-crystallization effects [4]. Several studies regarding controlled aging or annealing at different temperatures for various times have been performed on injection or compression moulded thick samples. Mechanical tests along with observation of the

*Corresponding author, e-mail: markus.gahleitner@borealisgroup.com

microstructure at different scales have been done in order to follow the induced changes and understand their origin [5–7], but such results are of limited relevance for predicting the behaviour of films, especially with respect to an alteration of the optical properties after a defined heat treatment.

In this special case the crystal structure originally generated in a process often involving massive quenching and high cooling rates will be a mixture of α-crystalline and mesomorphic phase, giving room for post-crystallization into the α-crystalline phase of iPP under the right circumstances. Since the first paper of Schael [8] a number of authors have dealt with the specific case of extruded cast films [9–12] which only recently has received special attention by the group of Androsch [13–15]. Their work has demonstrated that not only the degree of α-crystallinity is greatly reduced by quenching but also the morphology is changed from lamellar to a nodular structure. In another recent paper by De Santis *et al.* [16] not only the quenching process and mesophase formation, but also the possible transformation into the α-crystalline phase at higher temperatures was studied.

The polymorphic nature of iPP which is capable of crystallizing in three different ordered forms of the α-, β- and γ-modifications [17, 18] next to the mesomorphic state plays a limited role under the solidification conditions of cast film extrusion. While at least some α-nucleating agents are capable of inducing the γ-form as well [18] this modification does not form normally at high cooling rates. Formation of the β-modification should be avoided anyway when targeting transparency, but in absence of specific nucleating agents this modification would only be formed at very high chill roll temperatures (>110°C).

The present study was directed at understanding processing and sterilization effects on the crystalline structures and the resulting cast film performance for both PP homopolymers and EP random copolymers, including versions with different α-nucleating agents frequently used for improving transparency [19, 20]. The influence of polymer parameters (C_2-content and randomness of EP-copolymers as defined by catalyst systems and polymerization parameters), nucleating agents and processing parameters (variation of the film thickness and the chill-roll temperature in the cast film extrusion line) were studied. Finally, the changes in optics were correlated to crystallinity and morphology variations assessed by differential scanning calorimetry (DSC), wide- and small-angle X-ray diffraction (WAXD/SAXS) and transmission electron microscopy (TEM).

2. Experimental work

Three series of experimental materials, all produced in a Borstar™ PP pilot plant unit with triethyl aluminium (TEAL) as co-catalyst and cyclohexyl methyl dimethoxysilane (CHMDMS, donor C) as external donor were investigated for this study:

– Series 'A' covers 7 EP random copolymers produced with a proprietary, non-commercial Ziegler-Natta catalyst based on emulsion technology [21, 22] (C1). All grades had a reactor melt flow rate (MFR 230°C / 2.16 kg) of 1,5 g/10 min, were visbroken with peroxide (2,5-dimethyl-2,5-di-(tert. butylperoxy)hexane, Trigonox 101, Akzo-Nobel, Germany) to an MFR of 8 g/10 min and equipped with a standard additivation package (acid scavenger calcium stearate type 'SP', Faci, Italy; antioxidant blend Irganox B225, BASF AG, Germany; and synthetic silica as antiblocking agent, Sylobloc 45, Gracec Davison, USA).

– Series 'B' covers 6 EP random copolymers produced with a conventional high yield 4th generation Ziegler-Natta catalyst (C2; Avant ZN M1, Lyondell-Basell, Italy) having an ethylene content between 0 and 5 wt%. Visbreaking and additivation were the same as in series 'A'.

– Series 'C' covers EP-copolymers with a C2-content of about 3.5 wt% based on three different catalyst systems from the same category. The grade made with catalyst C2 (FTIR randomness 0.920) had an MFR of about 1.5 g/10 min and was subsequently visbroken to an MFR of 8 g/10 min, while the grades made with catalysts C1 (FTIR randomness 0.978) and C3 (conventional high yield 4th generation Ziegler-Natta catalyst, proprietary Borealis type, FTIR randomness 0.918) were neat reactor grades with an MFR of about 6 g/10 min. Different nucleating agents (A1 being an organophosphate, Adekastab NA-21, Adeka Palmaraole, France; A2 a sorbitol derivative, Millad 3988, Milliken, USA; and A3 a new carboxylic acid type, Hyperform HPN-68, Milliken, USA) for the α-modification were added together with the same additive

package as before, during the compounding step, testing against non-nucleated references.

For all PP materials, extrusion cast films of 50 and in some cases 130 μm thickness were produced on a PM30 type laboratory extruder (Plastik Maschinenbau GmbH., Germany) with a coat-hanger slit die 200 mm wide and with a gap range of 0.55 to 0.6 mm. The melt temperature was around 250°C, the chill roll temperature was set at 15°C for series A and B, while it was varied for series C (20, 55 and 90°C).

After the extrusion, all films were optically characterized according to ASTM D 1003 using a Hazegard Plus instrument (BYK-Gardner GmbH, Germany). The haze was chosen as most relevant parameter to assess differences in optics before and after sterilization. The measurements were done at least 96 h after film production or sterilization.

Steam sterilization was performed in a Systec D series machine (Systec Inc., USA). The samples were heated up at a heating rate of 5°C/min starting from 23°C. After having been kept for 30 min at 121°C, they were removed immediately from the steam sterilizer and stored at room temperature till processed further.

Crystallinity and morphology of the films before and after sterilization were studied by DSC, WAXD/SAXS and TEM, however not employing every method in each case. DSC measurements were carried out on a heat flux DSC 2920-CE (TA instruments, USA) on all samples before and after sterilization. Two heating scans and one cooling scan were done in between –10 and 210°C at a rate of 10°C/min. The analyzed samples had a weight of about 5 mg. The first heating cycle was considered to be the most interesting as it did not erase the history of thermal treated samples and was thus believed to give fairly reliable indications on the morphology of the investigated specimens. This is acceptable even though the test results are not as accurate as those provided by non destructive methods (e.g. WAXD). The melting temperature was determined as the maximum of the considered peak, and the melting enthalpies as the area under the respective peak.

Some selected samples were submitted to WAXD investigations at Vienna University of Technology and to TEM investigations at the Center for Electron Microscopy Graz, Austria. Wide-angle X-ray diffraction was done on the full films with a Philips X'Pert Pro instrument (Philips, Netherlands) using CuK_α radiation in reflection mode. The peak integration for determining crystallinity was performed as reported before [23]. Small-angle X-ray scattering was performed on a Bruker AXS Nanostar instrument (Bruker, USA) with rotating anode source and a wavelength of 0.154 nm using a Histar 2D detector at a sample distance of 105 cm.

For TEM, ultrathin sections of sample specimens contrasted with ruthenium tetroxide to allow differentiation between regions of high and low crystallinity were prepared [24]. Images were recorded on a Tecnai G^2 12 from FEI, USA, equipped with a CCD camera (Gatan Bioscan, Gatan Inc., USA) at 100 kV acceleration voltage.

Ethylene content and the degree of randomness of comonomer insertion were determined by FTIR spectroscopy on a Spectrometer System 2000 (Perkin Elmer, USA) on compression moulded films by relating the peak heights at 733 cm^{-1} (representing the total C_2 content) and the one at 720 cm^{-1} (representing the blocky insertion of ethylene) to each other [22]. Isotacticity was not determined, but from experience with the catalysts and donor employed a triad isotacticity (^{13}C-NMR) of ~97% can be assumed

3. Results and discussion

The basic composition and melting points determined on cast films are summarized for series 1 and 2 in Table 1, and for series 3 in Table 2 below. An example of the first heating cycle of a DSC thermogram of a freshly extruded cast film and sterilized film sample is provided in Figure 1 for one of the homopolymers from series A and for one of the EP-copolymers from series C. The main challenge in this evaluation is to fix the baseline of the DSC traces in a reproducible way and the split between the two peaks appearing after sterilization, which for simplicity was done by taking the baseline as the line between the first minimum points to the left and the right of the peak and the split between two peaks as a vertical section at the minimum between the two peaks.

Two effects are immediately obvious from the first two tables: The rather linear reduction of melting point and enthalpy with increasing C_2 content for series A and B (presented in Figure 2), and the fact

Table 1. Basic properties of the polymers from series A and B (melting point from DSC on cast film before sterilization, enthalpy before and after sterilization)

Sample number	Catalyst type	MFR 230°C/2,16 kg [g/10 min]	C_2 FTIR [wt%]	Randomness FTIR [–]	T_m [°C]	H_m (heat 1)		
						fresh [J/g]	sterilized [J/g]	Delta [J/g]
A/1	emulsion	8.0	0.0	not def.	162.9	100.7	100.9	0.2
A/2	emulsion	7.9	1.6	0.952	153.8	95.3	95.5	0.2
A/3	emulsion	7.5	2.4	0.972	146.6	87.9	90.3	2.4
A/4	emulsion	7.5	2.8	0.977	145.0	84.7	87.5	2.8
A/5	emulsion	8.2	3.5	0.979	144.0	83.7	85.1	1.4
A/6	emulsion	8.6	4.3	0.967	138.2	76.7	78.7	2.0
A/7	emulsion	8.4	5.2	0.958	132.3	68.5	73.8	5.3
B/1	standard	8.6	0.0	not def.	163.7	101.3	102.5	1.2
B/2	standard	7.4	1.6	0.913	154.7	94.1	96.0	1.9
B/3	standard	7.6	2.4	0.941	147.4	88.5	92.2	3.7
B/4	standard	8.5	3.3	0.915	145.2	83.3	88.4	5.1
B/5	standard	7.4	4.3	0.918	140.9	80.5	84.5	4.0
B/6	standard	7.2	5.0	0.900	136.3	75.1	80.9	5.8

Table 2. Basic properties of the polymers from series C (C_2 3.5 wt%; visbroken grades indicated by 'CR' for 'controlled rheology'; melting point from DSC on cast film processed at different chill roll temperatures before sterilization)

Sample number	Catalyst type	MFR 230°C/2,16 kg [g/10 min]	Reactor or CR type	Nucleation	T_m [°C] at chill roll temperature		
					20°C	55°C	90°C
C/1	C2	8.2	CR	No	143.1	144.5	146.3
C/2	C1	5.7	RE	No	146.3	144.5	150.0
C/3	C3	6.0	RE	No	142.0	143.3	145.3
C/4	C2	7.8	CR	A1	144.7	144.9	145.2
C/5	C1	5.8	RE	A1	146.7	148.1	149.5
C/6	C3	6.4	RE	A1	143.0	144.0	142.7
C/7	C2	8.1	CR	A2	144.1	145.2	145.8
C/8	C1	5.6	RE	A2	148.4	147.9	149.2
C/9	C3	6.1	RE	A2	143.1	143.8	140.5
C/10	C2	7.9	CR	A3	143.6	144.3	145.5
C/11	C1	5.7	RE	A3	147.7	147.8	149.0
C/12	C3	6.2	RE	A3	142.4	143.4	145.4

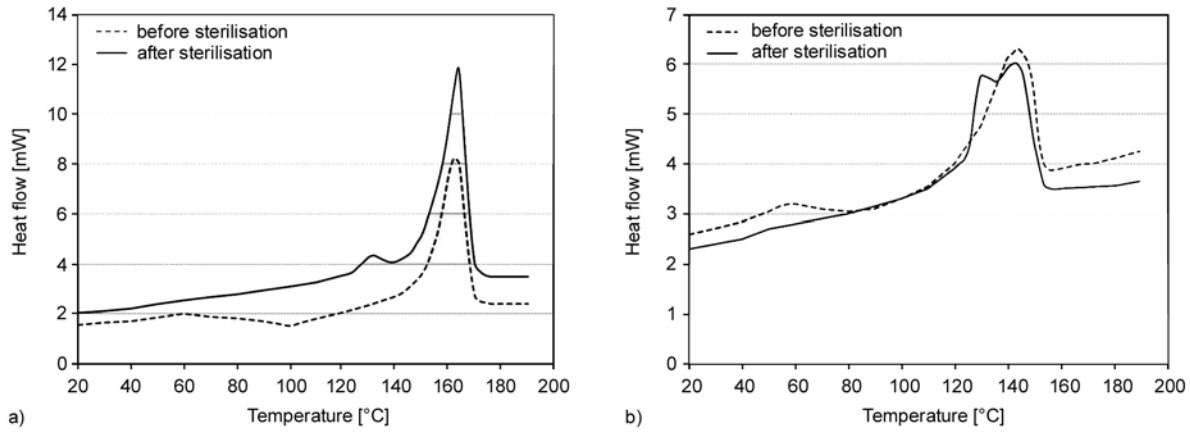

Figure 1. DSC thermograms recorded at 10 K/min for (a) PP homopolymer A/1 (MFR 8,0) processed at a chill roll temperature of 15°C, and (b) EP random copolymer C/3 (MFR 6,0 and 3,5 wt% C2) processed at a chill roll temperature of 55°C; scans before and after sterilization

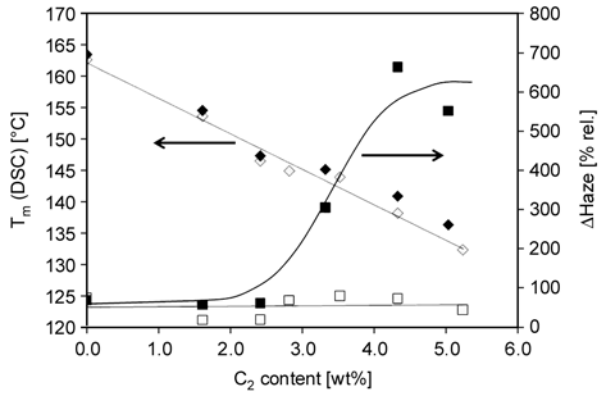

Figure 2. Changes in melting temperature and haze (cast film, 50 μm) in sterilization at 121°C depending on the C_2-content for polymers from series A (high randomness, open symbols) and second series B (limited randomness, filled symbols)

that both nucleation and catalyst type co-influence the quenching effect achieved by reducing the chill roll temperature in series C. Here, the chill roll temperature (T_{roll}) was varied between 20 and 90°C to simulate cases of a:

(i) a highly amorphous transparent structure with moderate stiffness (T_{roll}: 20°C),

(ii) a stiff film also having good starting optics (T_{roll}: 55°C),

(iii) a maximum crystalline film (T_{roll}: 90°C).

In the industrial practice of film processing, such variations are applied to balance film properties [25, 26], but the resulting crystal structures also define the long-term property evolution of the produced films. In an earlier paper from our group [27] the massive difference between injection moulded parts and cast films both in term of room temperature ageing and sterilization (annealing) behaviour has been demonstrated already.

The comonomer influence in the first two series is clearly reflected in the optical changes during sterilization. As Figure 2 shows, the haze increase from this annealing process remains rather constant up to an ethylene content of about 2.5 wt% and then rises significantly for the polymers based on the conventional catalyst (B) while staying at a lower level (<100%) for the emulsion catalyst based products with better randomness (A). The high numbers of up to ~670% for the relative haze change should be considered together with the absolute values listed in Table 3. Only for the materials showing the strongest haze increase, B/5 and B/6, the film loses its transparency visibly with absolute haze value of >15%.

Figure 3 further illustrates the fact that this trend in haze increase generally goes together with differ-

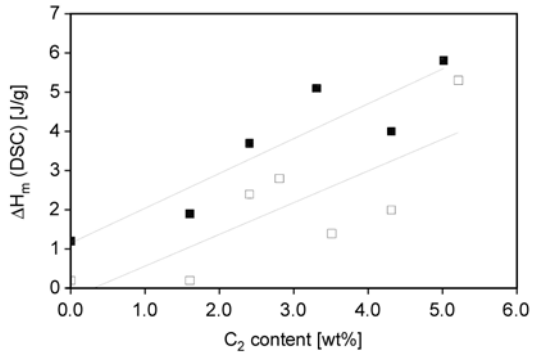

Figure 3. Changes in melting enthalpy in sterilization at 121°C depending on the C_2-content for polymers from series A (high randomness, open symbols) and second series B (limited randomness, filled symbols)

Table 3. Ethylene content and randomness effects on haze of PP cast films of 50 μm thickness produced at 15°C chill roll temperature (absolute values and change in sterilization) for polymers from series A and B

Number	C_2 FTIR [wt%]	Randomness FTIR [–]	Haze 50 μm film		
			fresh [%]	sterilized [%]	Delta [% rel.]
A/1	0.0	n.d.	2.2	3.8	73
A/2	1.6	0.952	1.9	2.2	16
A/3	2.4	0.972	2.3	2.7	17
A/4	2.8	0.977	1.8	3.0	67
A/5	3.5	0.979	2.7	4.8	78
A/6	4.3	0.967	2.4	4.1	71
A/7	5.2	0.958	2.8	4.0	43
B/1	0.0	n.d.	2.4	4.0	67
B/2	1.6	0.913	2.2	3.4	55
B/3	2.4	0.941	2.0	3.2	60
B/4	3.3	0.915	1.9	7.7	305
B/5	4.3	0.918	2.1	16.1	667
B/6	5.0	0.900	2.4	15.7	554

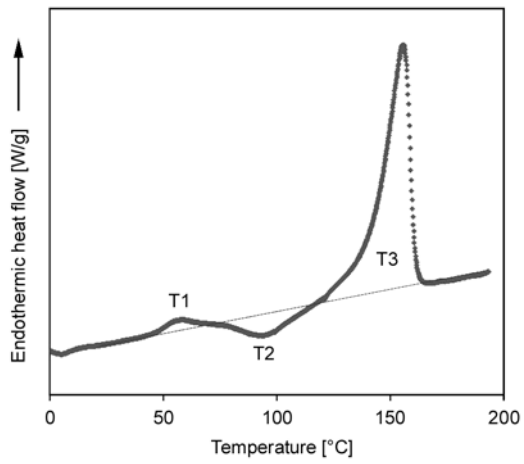

Figure 4. DSC thermogram (heat 1) recorded at 10 K/min for a 1.6 wt% ethylene content film (polymer B/2) before sterilization

ences in the post-crystallization intensity as expressed by the increase of melting enthalpy. An acceptable correlation between haze and crystallinity changes is only achieved for the materials from series B.

For better understanding this phenomenon, the fraction of the melting enthalpy curve below the sterilization temperature of 121°C was calculated in relation to the total melting enthalpy. The slope change at 2.5 wt% found in Figure 2 could not quite be reproduced here, but the reason for this becomes obvious when taking a closer look at the DSC curve (heat 1) before sterilization as recorded for material B/2 (see Figure 4) which is rather typical.

Three peaks could be distinguished here, corresponding to three transitions [28]:

(i) an endothermic peak (T1) with its maximum at around 60°C,

(ii) an exothermic peak (T2) with its maximum at around 100°C,

(iii) a large endothermic peak (T3) with its maximum at around 160°C in the case of the homopolymer (resp. 156°C for the polymer considered here).

Peak T1 probably is just the result of a superposition of the post-crystallisation peak T2 and the melting peak T3, with the exothermic peak T2 resulting from post-crystallization due to the increased mobility of the crystalline phase starting at ~50°C [29].

With this increased mobility, further crystallization of the quenched film takes place both in the form of lamellar thickening and in the formation of secondary crystals in the amorphous regions between the lamellae [7, 28]. The rearrangement of the amorphous part – and probably part of the mesomorphic fraction as well – causes a crystallization peak. Evaluation of the area of this peak T2 showed a linear decrease of this area with the increase in ethylene content. This area evaluation is not exact as the superposition of the two peaks leads to high error but it is representative of the evolution. The increase in ethylene content therefore improves the optical properties of the films before sterilization by reducing haze. However it also increases the difference in the optical properties of the films with sterilization and encourages secondary crystallization; this increased 'quenchability' of PP grades with reduced regularity due to stereodefects and/or comonomer incorporation has already been demonstrated before by La Carrubba *et al.* [30].

After sterilization, the DSC analysis of the films reveals a double melting peak as already evidenced in Figure 1. Surprisingly, the first peak of these is always at the same temperature of ~131°C, indicating the secondary crystals generated in the sterilization step being rather independent of the ethylene content. Figure 5 gives the partial enthalpies for the primary (high T_m, depending on C_2 content) and secondary (low T_m, 131°C) crystallization fractions in the films from the B-series (conventional catalyst, limited randomness). The qualitative correlation of the latter part to the haze increase in Figure 3 is quite striking – at the highest comonomer content the chain irregularities obviously even reduce the capacity for post-crystallization, in line with the overall crystallization speed reduction found for such materials before [1]. A possible explanation for the limited correlation between haze and crystallinity changes for material series A mentioned

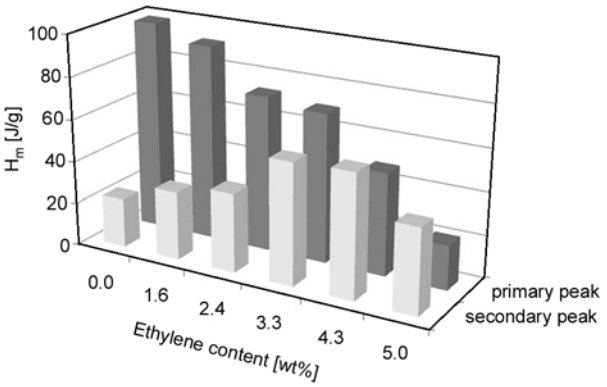

Figure 5. Partial melting enthalpy for primary and secondary crystallization melting for the sterilized cast films from series B

above could be the changing relation between primary and secondary crystals with changing comonomer content.

In series C, where the focus was on processing and nucleation effects, the optical properties were found to deteriorate with increasing the chill roll temperatures as a result of an increase in crystallinity as to be expected from literature [31]. When exemplified with material C/1 (non-nucleated sample), this feature corresponds to an enhancement of the melt enthalpy from 64.0 J/g for a chill roll temperature of 20°C, to 76.1 J/g for a chill roll temperature of 55°C, to 82.7 J/g for a chill roll temperature of 90°C. Two factors play a parallel role in this effect for high chill roll temperatures, especially in absence of a nucleating agent:

(i) the reduction of the rate of crystallization allowing the crystallites to grow to large spherulites, in turn increasing the haze (see Figure 6), and

(ii) a reduction of the amount of mesomorphic phase in the system [32].

Even though the optical performance worsened with the chill roll temperature, this picture was notably influenced by nucleation as also highlighted in Table 4. Both the organophosphate and the sorbitol derivative, i.e. a particulate and a soluble nucleating agent, are obviously capable of stabilizing the transparency at an acceptable level by increasing the number of nuclei in the system and limiting spherulite size. The higher overall crystallization rate promoted by heterogeneous nucleation [15] also results in a lower sensitivity of α-nucleated samples to cooling rates. This result suggests that the morphology and thus the optical performance of random copolymers can be controlled by α-nucleation rather independently of the conversion temperature.

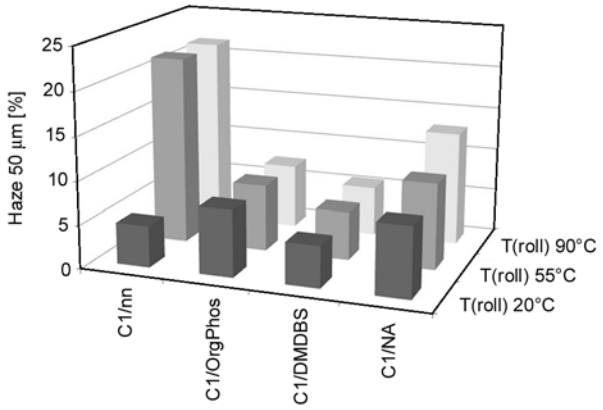

Figure 6. Nucleation and processing effects on haze of PP cast films of 50 µm thickness before sterilization (chill roll temperature variation from 20 to 90°C) for one of the polymers from series C (catalyst C1)

The relative change in haze as a function of the chill roll temperature of up to 80% starting from a very low haze level of around 3 to 6% for the 'worst' nucleating agent tested contrasts sharply to a variation of up to 670% for non-nucleated samples as a consequence of the processing conditions as already mentioned earlier. The low difference in haze between a chill roll temperature of 55 and 90°C suggests that the crystallization speed of the studied polymer is not overruled by processing parameters, while the opposite holds for chill-roll temperatures of 20°C independently of the material under investigation.

Table 4 also gives the difference in haze caused by sterilization; these variations are more or less pronounced depending on the initial crystalline state of the grade. For the medium chill roll temperature of 55°C the situation is illustrated in Figure 7: The different interaction between polymer and nucleating agent for the materials based on the emulsion catalyst C1 (higher randomness) allows better haze values after sterilization despite slightly higher ones before, at least for two of the nucleating agents. Quenched films obtained with a chill roll temperature of 20°C are far more sensitive to a heat treat-

Table 4. Nucleation and chill roll temperature effects on haze of PP cast films of 50 µm thickness (absolute values and change in sterilization) for two different polymers from series C (same as in Figure 6)

Sample number	Catalyst type	Nucl. type	Haze 20°C		Haze 55°C		Haze 90°C	
			fresh	Delta	fresh	Delta	fresh	Delta
C/2	C1	No	4.8	2.3	21.7	1.4	21.7	1.4
C/5		A1	7.7	0.0	7.7	0.9	7.4	1.9
C/8		A2	4.8	2.5	5.6	1.6	5.7	7.8
C/11		A3	8.1	4.5	9.9	1.5	13.1	2.1
C/3	C3	No	4.7	1.8	19.2	0.9	25.3	0.5
C/6		A1	6.8	3.2	6.1	5.3	6.5	1.7
C/9		A2	4.2	6.1	4.7	4.5	5.3	9.1
C/12		A3	6.7	3.7	8.4	0.8	11.6	1.6

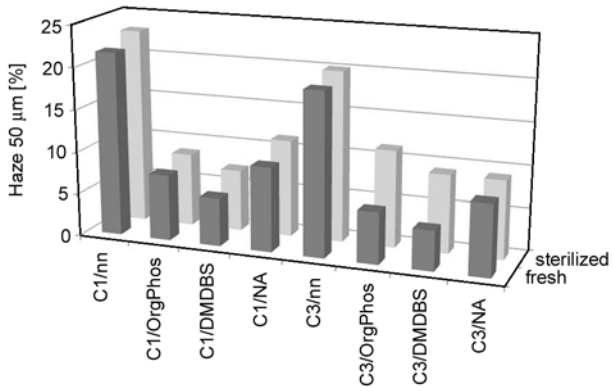

Figure 7. Nucleation and sterilization effects on haze of PP cast films of 50 µm thickness (chill roll temperature 55°C) for two different polymers from series C (catalysts C2 and C3, same C_2 content but different randomness)

ment than more crystalline samples manufactured at a chill-roll temperature of 90°C. They undergo the largest reorganization and lamellar thickening with sterilization, as a combination of annealing and post-crystallization effects as also documented in the literature [6, 7, 9, 27–29].

The occurrence of lamellar thickening in post-crystallization – as a result of a reduction of the magnitude on the interfacial free energy [7] – could be confirmed by TEM (see Figur 8) and in WAXD/SAXS analysis (see Table 5). Using the example of a nucleated sample processed at a chill-roll temperature of 90°C, it becomes obvious that a heat treatment at 121°C for 30 min promotes the formation of thicker lamella and leads to a denser network of crystalline structures. The X-ray data moreover show two very interesting phenomena:

(i) the crystallinity increase in sterilization is significant only for the non-nucleated sample, providing an additional explanation for the reduced haze increase in nucleated materials (see again Table 3),

(ii) in contrast to expectations from theory (which predicts an increase due to the higher crystallization temperature [33]), nucleation does not affect the lamellar thickness in cast-film processing.

In detail, the correlation between lamellar thickening and haze increase remains a subject of speculation. It is difficult understand either how a change in crystallinity on the nm-scale should affect light scattering, but secondary effects like surface distortion and roughness might play a role here.

Table 5. Results of WAXD/SAXS analysis of films from materials C/3 and C/6 (catalyst C3, MFR 6, 3.5 wt% C2) before and after sterilization; overall crystallinity from WAXD and long period L from SAXS given

Sample	State	X_{cr} [%]	L [nm]
C/3, non-nucleated	extruded 90°C	56	11,3
C/3, non-nucleated	sterilized 121°C	64	15,1
C/6, nucleated	extruded 90°C	61	11,5
C/6, nucleated	sterilized 121°C	63	15,2

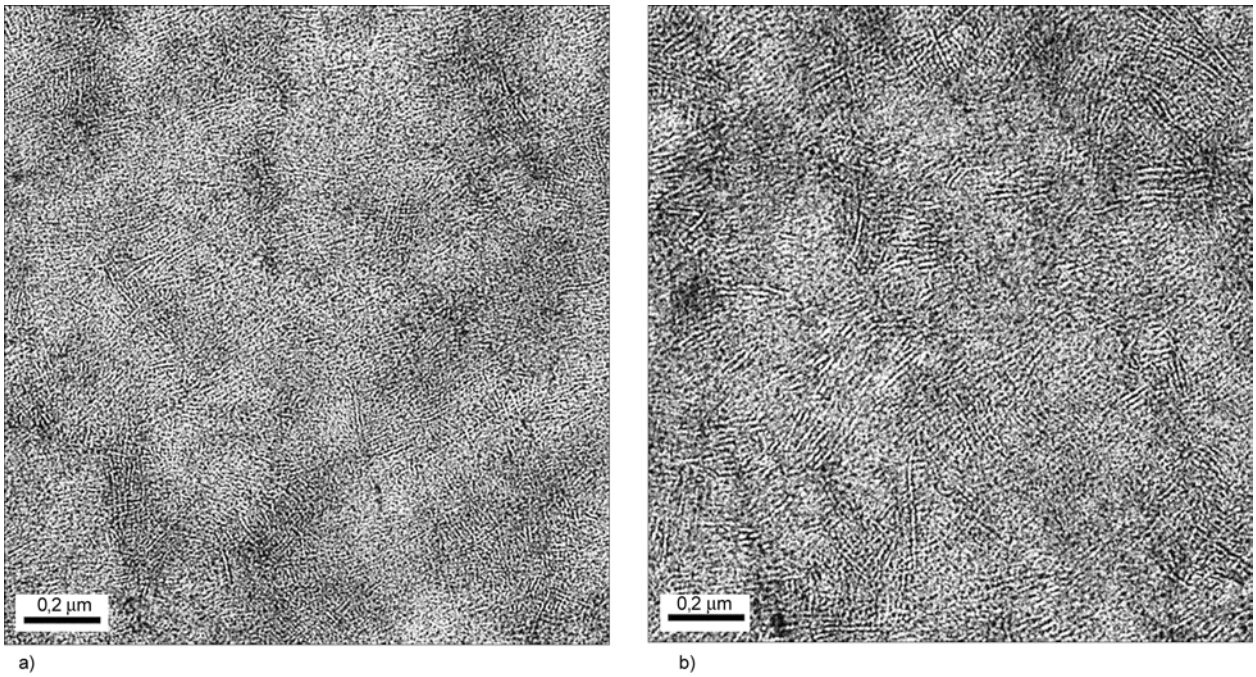

Figure 8. TEM images of the lamellar morphology of material C/6 (catalyst C3, MFR 6, 3.5 wt% C_2) from cast film extruded at chill roll temperature of 90°C before (a) and after (b) sterilization at 121°C; scale bar dimension 200 nm

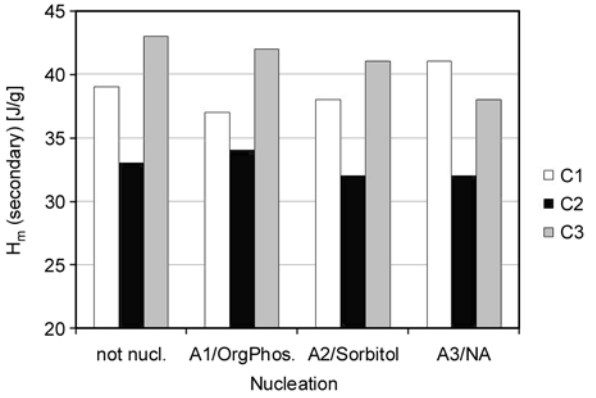

Figure 9. Melting enthalpy of secondary crystallization after sterilization for polymers from series C extruded at T_{roll} = 20°C

Also for the third series an attempt to correlate haze variations with crystallinity changes before and after sterilization was made using the DSC traces of the first heat after sterilization. As explained before, a double peak was found with high reproducibility for all samples. In contrast to the results shown in Figure 5, where a clear correlation of both primary and secondary peak with the comonomer content could be established, the situation was found to be far more complex here. In general, the relative amount (enthalpy) of the secondary crystallization was higher for the 20°C chill roll temperatures than for the 90°C chill roll temperature, confirming the increased mobility in more strongly quenched films observed for PP homopolymers before [27].

Another clear difference among the materials results from the catalyst choice; the lower area of secondary crystallization for materials based on the emulsion catalyst C1 for the quenched films was quite obvious (see Figure 9). One possible reason is the higher melting point mentioned above for these films which leads to less reorganization due to melting. Another effect could also be the decrease of lamellar thickening with the increase in randomly distributed ethylene content as the lamellae are already thick enough and could not thicken further. The influence of the nucleating agents on the secondary crystallization is however not visible in the DSC analysis as the areas of all the films for a given polymerization method are nearly constant. This is true for all three chill roll temperatures.

4. Conclusions

We investigated the structure of EP random copolymer films before and after sterilization at 121°C for 30 minutes by DSC, TEM, POM and WAXD/SAXS to explain the changes in optical properties (haze) of extrusion cast films. In addition to the comonomer content and the polymer structure (as a function of polymerization conditions and visbreaking), nucleating agents and extrusion conditions were changed. Three series of films were studied, varying catalyst type and comonomer content in the first two series, and catalyst, molecular weight distribution, nucleation and processing conditions in the third one. The findings clearly show that a combination of homogeneously randomized comonomer distribution and nucleation can partly inhibit lamellar thickening in sterilization, thus preserving high transparency even after a heat treatment.

In detail, attention has to be paid to the combined effects of physical ageing and post-crystallization, which both are affected by the chain regularity. The appearance of a rather constant secondary melting peak in DSC at a temperature of 10 K above the sterilization temperature clearly points to the existence of secondary crystalline structures postulated before by several authors [7, 27, 28]. More extensive investigations, especially using the possibilities of X-ray diffraction, will be required to develop a more complete understanding.

References

[1] Gahleitner M., Jääskeläinen P., Ratajski E., Paulik C., Reussner J., Wolfschwenger J., Neißl W.: Propylene–ethylene random copolymers: Comonomer effects on crystallinity and application properties. Journal of Applied Polymer Science, **95**, 1073–1081 (2005). DOI: 10.1002/app.21308

[2] Thorat H. B., Prabhu C. S., Suresh K. K., Pandya M. V.: γ-ray-induced degradation in ethylene-propylene copolymer. Journal of Applied Polymer Science, **59**, 1769–1773 (1996). DOI: 10.1002/(SICI)1097-4628(19960314)59:11<1769::AID-APP13>3.0.CO;2-P

[3] Resch K., Wallner G. M., Teichert C., Maier G., Gahleitner M.: Optical properties of highly transparent polypropylene cast films: Influence of material structure, additives, and processing conditions. Polymer Engineering and Science, **46**, 520–531 (2006). DOI: 10.1002/pen.20503

[4] Gezovich D. M., Geil P. H.: Deformation and aging of quenched polypropylene. Polymer Engineering and Science, **8**, 210–215 (1986).
DOI: 10.1002/pen.760080306

[5] Vittoria V.: Investigation of the ageing of isotactic polypropylene via transport properties. Polymer, **29**, 1118–1123 (1988).
DOI: 10.1016/0032-3861(88)90025-0

[6] Piccarolo S.: Ageing of isotactic polypropylene due to morphology evolution, experimental limitations of realtime density measurements with a gradient column. Polymer, **47**, 5610–5622 (2006).
DOI: 10.1016/j.polymer.2005.03.128

[7] Marand H., Alizadeh A., Sohn S., Xu J., Farmer R., Prabhu V., Cronin S., Velikov V.: A model for the physical aging of semicrystalline polymers above T_g: Secondary crystallization induced constraining effects. Proceedings of SPE ANTEC 59, Vol. 2, 1856–1859 (2001).

[8] Schael G. W.: A study of the morphology and physical properties of polypropylene films. Journal of Applied Polymer Science, **10**, 901–915 (1966).
DOI: 10.1002/app.1966.070100607

[9] O'Kane W. J., Young R. J., Ryan A. J.: The effect of annealing on the structure and properties of isotactic polypropylene films. Journal of Macromolecular Science Part B: Physics, **34**, 427–458 (1995).
DOI: 10.1080/00222349508219502

[10] Ferrer-Balas D., Maspoch M. L., Martinez A. B., Santana O. O.: Influence of annealing on the microstructural, tensile and fracture properties of polypropylene films. Polymer, **42**, 1697–1705 (2001).
DOI: 10.1016/S0032-3861(00)00487-0

[11] Marega C., Causin V., Marigo A.: A SAXS–WAXD study on the mesomorphic-α transition of isotactic polypropylene. Journal of Applied Polymer Science, **109**, 32–37 (2008).
DOI: 10.1002/app.28017

[12] Polo-Corpa M. J., Benavente R., Velilla T., Quijada R., Pérez E., Cerrada M. L.: Development of the mesomorphic phase in isotactic propene/higher α-olefin copolymers at intermediate comonomer content and its effect on properties. European Polymer Journal, **46**, 1345–1354 (2010).
DOI: 10.1016/j.eurpolymj.2010.03.014

[13] Mileva D., Androsch R., Radusch H-J.: Effect of cooling rate on melt-crystallization of random propylene-ethylene and propylene-1-butene copolymers. Polymer Bulletin, **61**, 643–654 (2008).
DOI: 10.1007/s00289-008-0979-6

[14] Androsch R.: In situ atomic force microscopy of the mesomorphic–monoclinic phase transition in isotactic polypropylene. Macromolecules, **41**, 533–535 (2008).
DOI: 10.1021/ma702334q

[15] Mileva D., Zia Q., Androsch R., Radusch H-J., Piccarolo S.: Mesophase formation in poly(propylene-*ran*-1-butene) by rapid cooling. Polymer, **50**, 5482–5489 (2009).
DOI: 10.1016/j.polymer.2009.09.064

[16] De Santis F., Adamovsky S., Titomanlio G., Schick C.: Scanning nanocalorimetry at high cooling rate of isotactic polypropylene. Macromolecules, **39**, 2562–2567 (2006).
DOI: 10.1021/ma052525n

[17] Lotz B., Wittmann J. C., Lovinger A. J.: Structure and morphology of poly(propylenes): A molecular analysis. Polymer, **37**, 4979–4992 (1996).
DOI: 10.1016/0032-3861(96)00370-9

[18] Foresta T., Piccarolo S., Goldbeck-Wood G.: Competition between α and γ phases in isotactic polypropylene: Effects of ethylene content and nucleating agents at different cooling rates. Polymer, **42**, 1167–1176 (2001).
DOI: 10.1016/S0032-3861(00)00404-3

[19] Macauley N. J., Harkin-Jones E. M. A., Murphy W. R.: The influence of nucleating agents on the extrusion and thermoforming of polypropylene. Polymer Engineering and Science, **38**, 662–670 (1998).
DOI: 10.1002/pen.10214

[20] Bernland K., Tervoort T., Smith P.: Phase behavior and optical- and mechanical properties of the binary system isotactic polypropylene and the nucleating/clarifying agent 1,2,3-trideoxy-4,6:5,7-bis-*O*-[(4-propylphenyl) methylene]-nonitol. Polymer, **50**, 2460–2464 (2009).
DOI: 10.1016/j.polymer.2009.03.010

[21] Abboud M., Denifl P., Reichert K-H.: Study of the morphology and kinetics of novel Ziegler-Natta catalysts for propylene polymerization. Journal of Applied Polymer Science, **98**, 2191–2200 (2005).
DOI: 10.1002/app.22412

[22] Grein C., Schedenig T.: Polyolefin compositions having improved optical and mechanical properties. WO 2009/027389, Germany (2007).

[23] Koch T., Seidler S., Halwax E., Bernstorff S.: Microhardness of quenched and annealed isotactic polypropylene. Journal of Materials Science, **42**, 5318–5326 (2007).
DOI: 10.1007/s10853-006-0960-4

[24] Zia Q., Androsch R., Radusch H-J., Ingolic E.: Crystal morphology of rapidly cooled isotactic polypropylene: A comparative study by TEM and AFM. Polymer Bulletin, **60**, 791–798 (2008).
DOI: 10.1007/s00289-008-0908-8

[25] Cotto D., Duffo P., Haudin J. M.: Cast film extrusion of polypropylene films. International Polymer Processing, **4**, 103–113 (1989).

[26] Duffo P., Monasse B., Haudin J. M.: Influence of stretching and cooling conditions in cast film extrusion of PP films. International Polymer Processing, **5**, 272–283 (1990).

[27] Gahleitner M., Fiebig J., Wolfschwenger J., Dreiling G., Paulik C.: Post-crystallization and physical aging of polypropylene: Material and processing effects. Journal of Macromolecular Science Part B: Physics, **41**, 833–849 (2002).
DOI: 10.1081/MB-120013068

[28] Alberola N., Fugier M., Petit D., Fillon B.: Microstructure of quenched and annealed films of isotactic polypropylene. Journal of Materials Science, **30**, 1187–1195 (1995).
DOI: 10.1007/BF00356118

[29] Agarwal M. K., Schultz J. M.: The physical aging of isotactic polypropylene. Polymer Engineering and Science, **21**, 776–781 (1981).
DOI: 10.1002/pen.760211206

[30] La Carrubba V., Piccarolo S., Brucato V.: Crystallization kinetics of iPP: Influence of operating conditions and molecular parameters. Journal of Applied Polymer Science, **104**, 1358–1367 (2007).
DOI: 10.1002/app.25871

[31] Resch K., Wallner G. M., Teichert C., Gahleitner M.: Highly transparent polypropylene cast films: Relationships between optical properties, additives, and surface structure. Polymer Engineering and Science, **47**, 1021–1032 (2007).
DOI: 10.1002/pen.20781

[32] Martorana A., Piccarolo S., Schichilone F.: The X-ray determination of the amounts of the phases in samples of isotactic poly(propylene) quenched from the melt at different cooling rates. Macromolecular Chemistry and Physics, **198**, 597–604 (1997).
DOI: 10.1002/macp.1997.021980231

[33] Pukánszky B., Mudra I., Staniek P.: Relation of crystalline structure and mechanical properties of nucleated polypropylene. Journal of Vinyl and Additive Technology, **3**, 53–57 (1997).
DOI: 10.1002/vnl.10165

eXPRESS Polymer Letters Vol.5, No.9 (2011) 799–808
Available online at www.expresspolymlett.com
DOI: 10.3144/expresspolymlett.2011.78

Interfacial adhesion of nanoparticles in polymer blends by intrinsic fluorescence spectra

J. Yang[1], G. S. He[1], B. Zhang[2], W. A. Luo[2], X. D. Chen[1], R. W. Fu[2], M. Q. Zhang[2]*

[1]Institute of Polymer Science, DSAPM Lab, OFCM Institute, School of Chemistry and Chemical Engineering, Sun Yat-Sen University, Guangzhou 510275, P. R. China
[2]Key Laboratory for Polymeric Composite and Functional Materials of Ministry of Education, School of Chemistry and Chemical Engineering, Sun Yat-sen University, Guangzhou 510275, P. R. China

Received 26 December 2010; accepted in revised form 18 March 2011

Abstract. Intrinsic fluorescence was applied to quantitatively describe the interfacial adhesion of nanoparticles in polystyrene/poly(vinyl methyl ether) (PS/PVME) blends. Due to the aggregation of aromatic rings on PS chains, the temperature dependence of excimer fluorescence intensity (I_{324}) showed the high sensitivity to the phase separation process. Consistent with Ginzburg thermodynamic model, it was found that the addition of spherical hydrophilic nanoparticles shifted the phase separation temperature to higher temperatures due to the aggregation of silica into PVME chains leading to the free energy reduction and slowing down the phase separation dynamics. A certain composition of polymer blend, i.e. 2/8, was focused on to shed light on the dynamic of spinodal decomposition (SD) phase separation by using decomposition reaction model. It was shown that the addition of nanoparticles to polymer blends resulted in the deviation of linear relationship between the initial SD phase separation rate (R_{p0}) and thermodynamic driving force (Δf_{SD}). Besides, for PS/PVME (2/8) with 2 vol% silica nanoparticles, the apparent activation energy of phase separation (E_a) was 196.61 kJ/mol, which was higher than that of neat PS/PVME (2/8) blend (E_a = 173.68 kJ/mol), which strongly confirmed the interfacial adhesion effect of silica nanoparticles as compatibilizers.

Keywords: *polymer blends and alloys, phase separation, nanoparticles, fluorescence*

1. Introduction

During the past years, a large number of studies focused on the miscibility and phase separation in polymer blends, from both theoretical and experimental viewpoints [1–6]. For polymer mixtures, controlling components compatibility has always seemed to be a very important factor in polymer industry. Recently, as potential compatibilizers, nanoparticles have attracted more and more attention due to their important role the immiscible polymer blends [7–12]. It has been shown that introducing nanoparticles can make the phase behavior more complicated by changing the shape of the phase diagram [13], changing the interaction parameter between two components [14, 15], and increasing or decreasing the phase separation temperature [13–16].

Among previous studies, a number of analytical methods [17–21] such as thermal analysis, atomic force microscopy (AFM), and scattering methods (visible light, neutron, X-ray) have been frequently used to investigate phase behavior of polymer blends. However, each of these techniques has its advantages and disadvantages, depending on the systems and problems of interest. For instance, the thermal analyses are very convenient to observe the miscibility in polymer blends, but sometimes it is hard to detect T_gs of polymer blends very clearly.

*Corresponding author, e-mail: ceszmq@mail.sysu.edu.cn

Compared with AFM, light scattering methods are superior because one can analyze the relaxation rate as a function of the scattering vector and that one can follow, *in situ*, the rapid growth of the fluctuations without introducing an additional physical process such as freezing a given phase-separated state. However, the light scattering technique inevitably depends on the expensive equipment and sophisticated process. As a sensitive method, the fluorescence technology is also widely applied to investigate macromolecular chain movements with probe and labeling [22–24]. Furthermore, it has been proved that the fluorescence technique can provide us with information on a scale smaller than conventional light scattering and comparable to small-angle neutron scattering [25]. Although fluorescence method can obtain lots of useful information of polymer micromorphology and microstructure, the labeling procedure is often tedious. In addition, in most of the fluorimetric studies of polymer, the fluorescent probe was covalently attached to one of the polymers, which in fact changed the microenvironment of macromolecules and made the macromolecules more hydrophobic, thus enhancing their complexation ability. Actually, the intrinsic fluorescence of polymers (e.g. polystyrene) has also been shown to be highly sensitive to issues ranging from local polymer conformational populations in solution and phase behavior in solvents and polymer blends to local microenvironments in bulk homopolymers [26–30].

Thus, intrinsic fluorescence was employed to investigate the phase separation behavior of polymer blends in our work. Here, polystyrene/poly(vinyl methyl ether) (PS/PVME) blend has been chosen as a model system. This blend exhibits a typical lower critical solution temperature (LCST) behavior [31–33], which is illustrated by the schematic polymer-polymer phase diagram in Figure 1. In this work, the interfacial adhesion of nanoparticles in PS/PVME blends has been quantitatively characterized by intrinsic fluorescence combining with a simple model based on decomposition reaction.

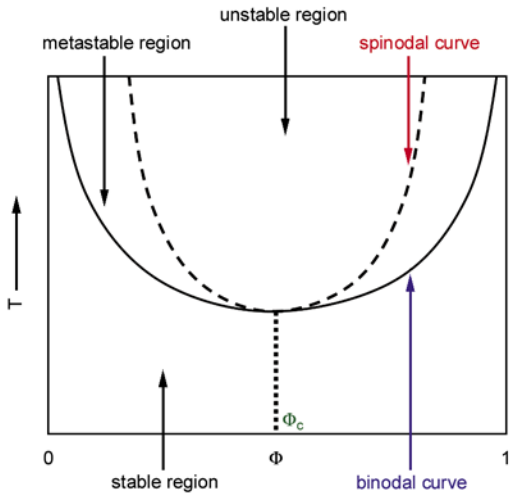

Figure 1. Schematic phase diagram of a polymer blend which exhibits a lower critical solution temperature (LCST)

2. Experimental

2.1. Materials

PS (M_w = 354 000 g/mol, PDI = 1.05, Polymer Source Inc., Canada) and PVME (M_w = 90 600 g/mol, PDI = 1.95, Scientific Polymer Products Inc., U. S. A.) were used in this study. Silica nanoparticles (Aerosil 200) were supplied by Evonik-Degussa Co., (Germany) with an average diameter of 12 nm and a specific surface area of 200 m^2/g. The particles were dried at 120°C under vacuum for 24 h to eliminate the physically absorbed and weakly chemically absorbed species. The PS/PVME/nanoparticles samples were prepared by continuous mechanical mixing of the components in toluene. And then, film samples were prepared by casting from 10 wt% toluene solutions of the polymer blend containing onto quartz plates at room temperature. The films were further heat treated in a vacuum oven at 45°C for 4 h and then 65°C for 24 h in order to remove the residual solvent. The vacuum was applied slowly to prevent any possible bubble formation. We found this procedure resulted in homogeneous films which were slightly opaque. The thickness of film was about 3 μm.

2.2. Methods

All the fluorescence emission spectra were recorded using a FLS920 Combined Fluorescence Lifetime and Steady State Spectrometer (Edinburgh, England) in front-face geometry. The excitation wavelength is at 260 nm and the slit (ex/em) width of the measurements was 1.5 nm/2.5 nm. The sample is heated by conduction via a nitrogen exchange gas in the sample space and the temperature control is achieved by a combination of manual nitrogen flow control and power dissipated in an electrical heater, regulated using an ITC temperature controller. By using this temperature-controlling accessory, the

variable-temperature measurements within 77–500 K can be carried out with the stability of ±0.1 K. In non-isothermal measurement, the sample was heated at a rate of 0.5 K/min with a time interval of 10 s for each increase of 2.5 K, while in isothermal measurement, the sample was heated to a specified temperature within 1 minute and then kept for 15 seconds.

3. Results and discussion

3.1. Phase separation temperature

Figure 2 shows the intrinsic fluorescence spectra of PS/PVME (2/8) film at different temperatures. It is clear that, for each spectrum, a maximum intensity can be observed at 324 nm, with a second, lesser peak at 283 nm. It is worth mentioning that, intrinsic fluorescence of PS consisted of both monomer and excimer fluorescence, the former due to emission from a single excited-state phenyl ring, while the latter due to the emission from an excited-state dimer consisting of two phenyl rings in a parallel, sandwich-like conformation with an inter-ring separation distance of 3–4 Å [34–36]. Hence, it is easy to understand that the intrinsic fluorescence peak at 324 and 283 nm should be ascribed to the excimer and monomer fluorescence, respectively. For PS, there exist three types of nominal excimer forming sites: (i) intermolecular interaction between rings on different chains (ii) intramolecular interaction between rings on nonadjacent chain segments and (iii) intramolecular site formed between aromatic in Figure 2, the intrinsic fluorescence intensity in the whole wavelength range increases as the temperature increases in the temperature range studied here. It is worth mentioning that the excited state of chromophore promoted by the absorption of a photon is usually deactivated by radiative (fluorescence K_r), and non-radiative (K_{nr}) and radiative energy transfer rates (K_{RET}), thus the change in intrinsic fluorescence intensity (I) can be understood considering Equation (1) for the fluorescence quantum yield (ϕ_F):

$$I \propto \phi_F = \frac{K_r}{K_r + K_{nr} + K_{RET}} \tag{1}$$

Since K_r only depends on temperature through the refraction index [40], Equation (1) can be expressed as Equation (2):

$$I \propto \frac{K_r^0 n^2}{K_r^0 n^2 + K_{nr} + K_{RET}} \tag{2}$$

where K_r^0 is a constant independent of temperature and n is the refraction index. Therefore, from Equation (2), it can be seen that intrinsic fluorescence is mainly influenced by n, K_{nr} and K_{RET}. Based on this point, the changes in intrinsic fluorescence intensity of excimer and monomer should be interpreted in terms of the balance of these three factors: (i) the reduction of the refraction index [41]; (ii) the deactivation of the fluorescence by non-radiative processes due to the increased thermal motions, and (iii) the attenuated radiative energy transfer caused by the decreased the local concentration of chromophore during volume expansion [42]. The detailed mechanism will be mentioned in the next section. In general, the results shown in Figure 2 reveal the sensitivity of the intrinsic fluorescence in the phase separation process of PS/PVME film.

Since the minor emission (monomer) was gradually affected by the adjacent major emission (excimer) in the fluorescence spectra during phase separation so that its intensity change could not reflect the actual conformational transitions. Thus, we only focused our attention on fluorescence intensity of excimer (I_{324}) rather than monomer (I_{283}). As shown in Figure 3, I_{324} first decreases slightly with the increasing temperature and then sharply increases at 368 K. It is noteworthy that the fluorescence intensity, which is proportional to the fluorescence quantum yield, is expected to decrease with increasing temperature because of an enhancement of non-radiative decay rates with increasing thermal energy. Besides, the change in the temperature dependence

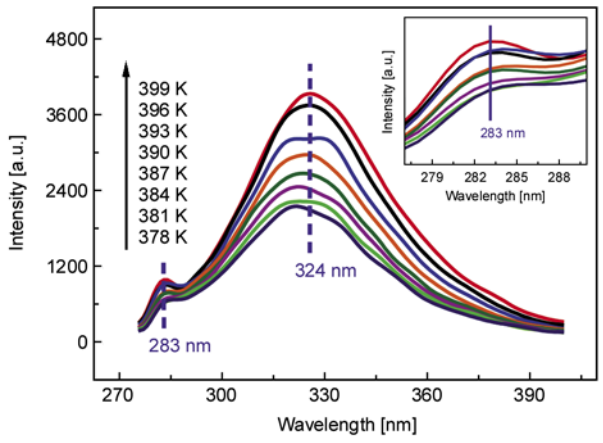

Figure 2. The intrinsic fluorescence spectra of PS/PVME (2/8) film at different temperatures. The inset shows enlargement of emission peak at 283 nm

at T_g is a manifestation of the change in the temperature dependence of polymer density which also affects non-radiative decay processes [43]. It can be seen that a faster decrease in the intrinsic fluorescence intensity appears at $T > T_g$ of PS, although the degree to which the intensity declines is small [43]. Thus, the sharp rise in fluorescence intensity should be taken as the signature of phase separation of PS/PVME. For comprehensive understanding of this behavior, the temperature dependence of excimer to monomer fluorescence intensity ratio (I_{324}/I_{283}) is also taken into account since excited-state monomer and excimer can be interconvertible during aggregation of PS [37–39]. Obviously, the value of I_{324}/I_{283} does not change so much and starts to enhance at above 368 K (see Figure 3). As we know, I_{324}/I_{283} depends upon two major factors [37]: (i) the electronic stability of the excimer complex, as manifested through the radiative and nonradiative fluorescence decay constants of the excimer and monomer which usually are not expected to vary appreciably and (ii) the number of excimer-forming sites [44] including the intramolecular site formed between aromatic rings on adjacent and/or nonadjacent repeat units on the same chain, and the intermolecular site formed between aromatic rings on different polymer chains. Thus, the explanation of variation of I_{324} and I_{324}/I_{283} should now be clear. At $T < 368$ K, the invariant value of I_{324}/I_{283} suggests that almost no conversion between monomer and excimer occurs, and thus the reduction of I_{324} should be attributed to the decrease of excimer fluorescence quantum yield caused by the enhancement of non-radiative decay rate [24] before phase separation. At $T > 368$ K, the aggregation of PS chains during phase separation results in the increase of the number of both intramolecular and intermolecular excimer sites, i.e. an increased probability of remote segment contact on the same chain and clustering of segments on different chains (see inset of Figure 3), leading to the increase of I_{324} and I_{324}/I_{283}. Due to the more distinguishable change of excimer fluorescence intensity during aggregation, only I_{324} will be considered for investigating the phase separation behavior in the following discussion.

In the case of nanoparticle-filled samples, temperature dependence of I_{324} is shown in Figure 4 for the PS/PVME (2/8) film with 2 vol% silica nanoparticles. In comparison with Figure 3, the intrinsic fluorescence spectra for PS/PVME with and without nanoparticles are very similar (see inset of Figure 4), which suggests fluorescence behavior of chromophores on PS chains in blends are not affected by the addition of nanoparticles. However, the inflection point for PS/PVME (2/8) film with 2% silica nanoparticles shifts to a higher temperature (375 K). This phenomenon should be attributed to the change of network structure in the blend caused by interfacial adhesion. Note that PVME molecules (dispersive solubility parameter, $\delta_d = 15.5$ MPa$^{1/2}$, and polar solubility parameter, $\delta_p = 7.1$ MPa$^{1/2}$) are much more polar than PS molecules ($\delta_d = 18.1$ MPa$^{1/2}$ and $\delta_p = 1.1$ MPa$^{1/2}$) [45] so that PVME chains tended to be preferentially absorbed on the nanoparticles surface. On the other hand, due to great thermodynamic work of adhesion between PS

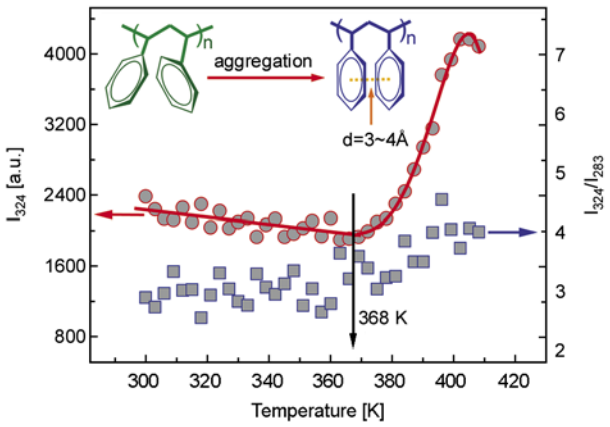

Figure 3. Temperature dependence of excimer fluorescence intensity (I_{324}) and excimer to monomer fluorescence intensity ratio (I_{324}/I_{283}) for the PS/PVME (2/8) film. Inset shows the conformational change of PS during aggregation process

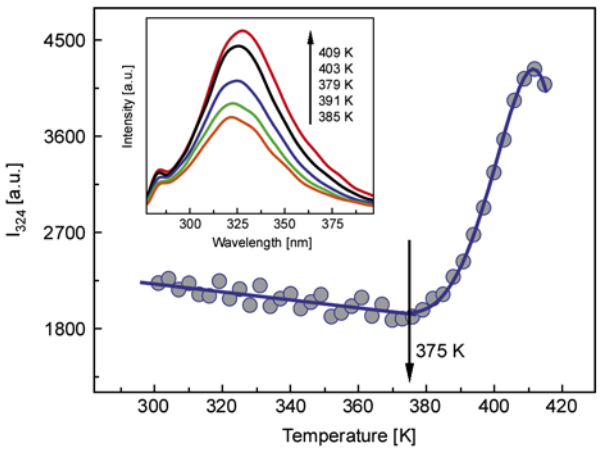

Figure 4. Temperature dependence of I_{324} for PS/PVME (2/8) film with 2 vol% silica nanoparticles. The inset shows the intrinsic fluorescence spectra at different temperatures

and PVME [46], the PS/PVME interface is still relatively stable under the shear forces during mixing so that nanoparticles more likely exist in PVME but not at the interphase between PS and PVME, forming the final core-shell structure which has been confirmed in scanning electron microscopy results obtained by Gharachorlou and Goharpey [46]. When the SD phase separation occurs, the low mobility region absorbed on nanoparticles would act like a network of obstacles for the coarsening of the interfaces and slow down the transition from interpenetrated structure to matrix-disperse [47]. Thus, the interconnected network can remain in its initial state for a longer time, showing a higher phase separation temperature which will be discussed in the following section.

Figure 5 shows the phase separation temperature curve determined by intrinsic fluorescence for PS/PVME blends with and without 2% silica nanoparticles. For each case, the extremum temperature appears at the low PS volume fraction (i.e. $\Phi_c = 0.2$), resulting from the higher molecular weight of one component (i.e. PS) [48]. Besides, as we know, the phase separation of PS/PVME film usually undergoes two different mechanisms, i.e. spinodal decomposition (SD) and nucleation and growth (NG) [33]. This critical PS volume fraction strongly suggests the phase separation of PS/PVME blend (2/8) that we focused on occurs only by SD mechanism since the binodal curve and spinodal curve intersect at Φ_c (shown in Figure 1). Recently, Ginzburg [16] proposed a simple model describing the thermodynamics of two homopolymers (A and B) with spherical nanoparticles (covered with an A-polymer layer). Here, the A-polymer refers to PVME (see inset of Figure 5). From his theory, one can obtain the effective decrease in the spinodal temperature of an upper critical solution temperature (UCST)-type binary blend in the presence of nanoparticles (Equation (3)):

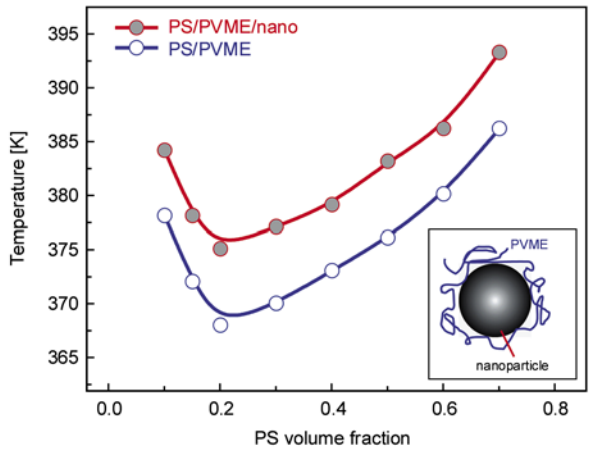

Figure 5. Phase separation temperature curve determined by intrinsic fluorescence for the PS/PVME blends with and without 2% silica nanoparticles The inset shows the schematic representation for spherical nanoparticles covered with PVME chains.

$$\frac{\Delta T_{sp}}{T_{sp}} \approx -\psi \tag{3}$$

where ψ and T_{sp} are the nanoparticle volume fraction and spinodal temperature of the neat binary blend, respectively. From Equation (3), it follows that for a binary blend ($\Phi = 0.2$) with a critical temperature of 368 K, addition of 2 vol% nanoparticles can reduce the spinodal temperature by about 7 K. Naturally, for LCST-type blends, the situation would be the opposite. In our work, addition of 2 vol% fumed silica caused the spinodal temperature to shift from 368 to 375 K for PS/PVME (2/8) blends. Therefore, the model proposed by Ginzburg successfully predicts the interfacial adhesion of nanoparticles in PS/PVME system.

3.2. Kinetics of whole process of phase separation.

To further characterize the interfacial adhesion of silica nanoparticles, the isothermal phase separation was also studied. The intrinsic fluorescence spectra of PS/PVME (2/8) film at 370 K at different times are presented in Figure 6. As expected, the time dependence of I_{324} shows that the intensity of spectra first steeply increases with the temperature increased, and then levels off which indicated the completion of phase separation process (see inset of Figure 6). The similar behavior has also been found in the case of PS/PVME with silica nanoparticles. Hereafter, I_{324} is used to perform a quantitative analysis of the kinetics for PS/PVME with and without nanoparticles.

Taking into account the slight fluorescence difference induced by the different thickness of films, the relative extent of phase separation (α) at time t has been considered. α is defined as Equation (4):

$$\alpha = \frac{I_t - I_0}{I_\infty - I_0} \tag{4}$$

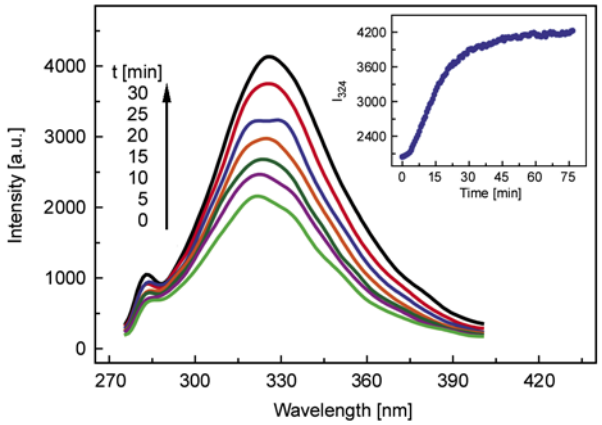

Figure 6. The intrinsic fluorescence spectra of PS/PVME (2/8) film during the isothermal phase separation at 370 K. The inset shows the time dependence of I_{324}

where I_t, I_0 and I_∞ are I_{324} for phase separation at time t, 0 and ∞, respectively. Time dependences of relative extent of phase separation of PS/PVME (2/8) film are shown in Figure 7. It can be seen that, the higher the temperature was, the faster the phase separation occurred, which was characteristic phase separation behavior of LCST polymer blend. The curves for PS/PVME/nanoparticles are similar with Figure 6, which are not shown here.

In order to simplify the quantitative calculation of the phase separation kinetics, we proposed a simple model based on decomposition reaction (see Figure 8), assuming nanoparticles always remains in the PVME phase. When the phase separation takes place, the 'reactant' (A), i.e. PS/PVME or PS/PVME/nanoparticles, would be decomposed into two products, i.e., (B) PS and (C) PVME or PVME/nanoparticles. As far as the 'decomposition reaction' with one 'reactant' is concerned, the evidence in favor of

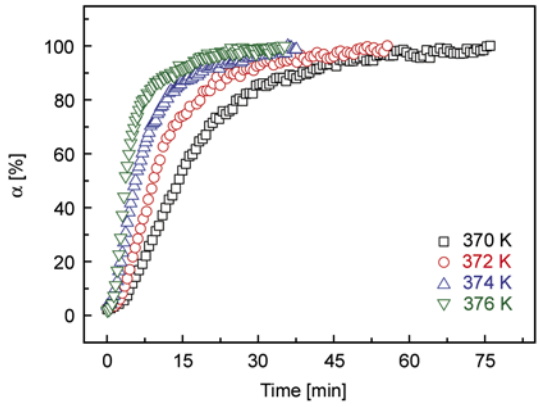

Figure 7. Time dependences of relative extent (α) of phase separation of PS/PVME (2/8) film at various temperatures

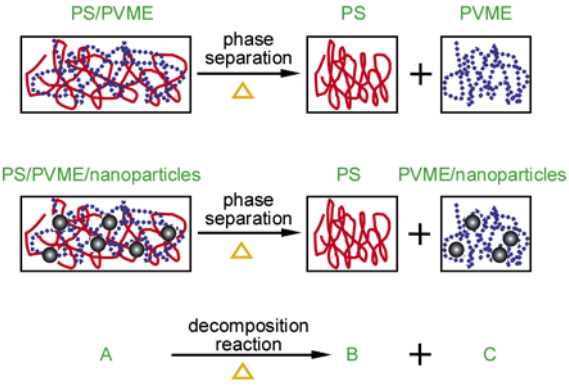

Figure 8. Schematic illustration of phase separation of PS/PVME/nanoparticles

the first order reaction is quite convincing, which means the rate of reaction is directly proportional to the concentration of one of the reactants [49, 50]. As a result, the rate of SD (R_p) can be simply expressed by Equation (5) [51]:

$$R_p = -\frac{d[A]}{dt} = k_p[A] \tag{5}$$

where $[A]$ stands for the weight ratio of un-phase-separated polymer blends to entire polymer blends (i.e. phase-separated part + un-phase-separated part), and k_p is the rate constant of SD. The integrated form of Equation (5) is shown in Equation (6):

$$\ln\frac{[A]_0}{[A]_t} = k_p t \tag{6}$$

where $[A]_0$ and $[A]_t$ are the values of $[A]$ at time 0 and t, respectively. On this basis, the initial SD phase separation rate (R_{p0}) can be obtained by inputting the values of k_p and $[A]_0$ into Equation (5). As expected [52], a linear relationship ($|R| = 0.9958$) is found for neat PS/PVME blend between R_{p0} and thermodynamic driving force (Δf_{SD}), i.e. (see Figure 9). Interestingly, however, in the case of PS/PVME blend with nanoparticles, with the best fit ($|R| = 0.9998$), R_{p0} does not increases linearly not quadratically with Δf_{SD}, which suggests a stronger dependence of phase separation rate on the thermodynamic factor in addition of nanoparticles. Since the interfacial tension changes with the temperature changes [53], this behavior is probably due to the temperature dependence of preferential surface adsorption of silica nanoparticles in the polymer blend at the higher temperature.

On the other hand, since the relative extent of phase separation (α) can be understood as the percent con-

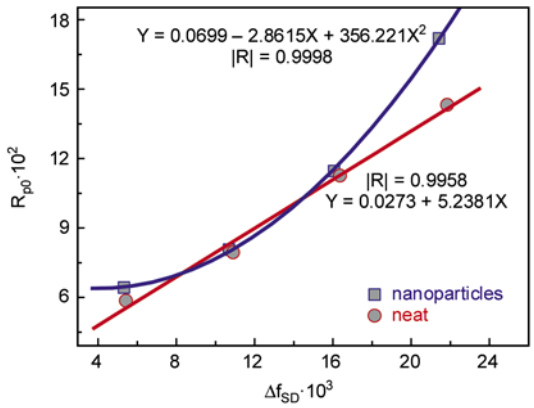

Figure 9. The dependence of SD initial rates on the thermodynamic driving force for the PS/PVME blends with and without 2% silica nanoparticles

version of decomposition reaction at time t, the Equation (6) can be written as shown in Equation (7):

$$\ln\frac{[A]_0}{[A]_t} = \ln\frac{1}{1-\alpha} \tag{7}$$

Therefore, the relationship between α and R_p can be expressed by Equation (8):

$$\ln(1-\alpha) = -k_p t \tag{8}$$

Figure 10 exhibits plots of $\ln(1-\alpha)$ *vs.* time of phase separation for PS/PVME (2/8) film. By using Equation (8), k_p can be easily obtained from the slopes of linear-fit lines in Figure 10 (see Table 1). Similarly, the phase separation rate constants for PS/PVME/nanoparticles were also calculated in this way. As can be seen in Table 1, all the absolute values of correlation coefficients (R) are in the range of 0.97–0.99 (very close to 1), which strongly

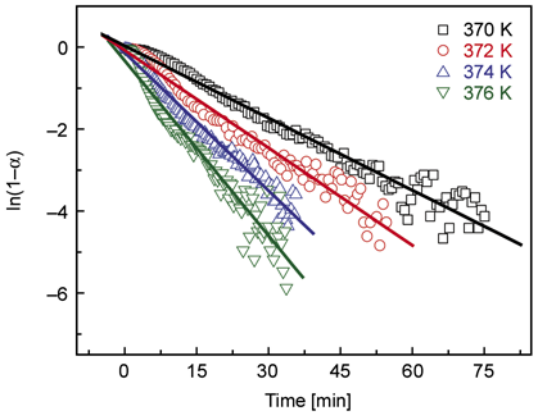

Figure 10. Plots of $\ln(1-\alpha)$ against time of phase separation for PS/PVME (2/8) film

Table 1. Phase separation kinetics parameters of PS/PVME (2/8) film with and without 2 vol% silica nanoparticles determined by intrinsic fluorescence spectroscopy

PS/PVME (2/8)	T [K]	k_P [min^{-1}]	|R|	E_g [kJ/mol]
neat	370	0.05888	0.98221	173.68
	372	0.07957	0.98292	
	374	0.11249	0.98825	
	376	0.14281	0.97171	
nanoparticles	377	0.06448	0.98326	196.61
	379	0.08075	0.98424	
	381	0.11445	0.98649	
	383	0.17125	0.95751	

confirms the above kinetics analysis based on the decomposition reaction assumption is reasonable.

To better describe the adhesion effect of nanoparticles in the polymer blends, apparent activation energy, E_a, of phase separation are obtained by applying Arrhenius equation ($k_p = A\exp(-E_a/RT)$) here. Figure 11 presents the plot of $\ln k_p$ against the reciprocal of temperature for the PS/PVME (2/8) with and without nanoparticles. Obviously, for each case, the rate constant k_p decreases with temperature increases and lnkp ~$1/T$ plot shows a good linear relation. Thus, E_a can be calculated from the slope of lines. As listed in Table 1, the apparent activation energy of the neat PS/PVME blend (E_a = 173.68 kJ/mol) was lower than that of the PS/PVME blend with nanoparticles (E_a = 196.61 kJ/mol). These values are very similar to apparent activation energy of phase separation for PS/PVME (2/8), 194.68 kJ/mol, obtained by resonance light scattering method [55]. It is worthwhile to mention that in the case of SD, the phases are interconnected at the initial stage of phase separation, during which the

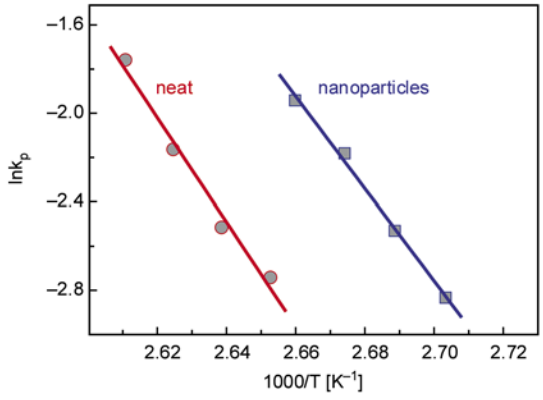

Figure 11. Plot of lnkp film against the reciprocal of temperature for the PS/PVME (2/8) with and without nanoparticles

domains are constant in size. With the time or temperature increases, the phase domains then grow in size while maintaining their connectivity, while in the latter stages the phases break into small spheres and then merge into macrospheres [54]. Note the phase growth is diffusion controlled, thus this apparent activation energy is a key parameter for characterizing the diffusion rate of macromolecular chains in polymer blends. So one can easily understand that the lower its value is, the easier the co-continuous network structure can be formed and transformed into macro-separated phases. This result highly consists with the results shown in Figure 5, clarifying the interfacial adhesion of silica nanoparticles.

4. Conclusions

In this work, the interfacial adhesion of nanoparticles in PS/PVME blends was studied by intrinsic fluorescence method. By monitoring the temperature dependence of excimer fluorescence intensity, it can be seen that the addition of spherical hydrophilic nanoparticles shifted the phase separation temperature to higher temperatures. This behavior was due to the absorption of some PVME chains on nanoparticles surface which assisted the free energy reduction and the stability of the homogeneous phase, slowing down the phase separation dynamics. Furthermore, a simple model based on the decomposition reaction was proposed to perform the quantitative analysis of the SD phase separation kinetics. Compared with neat blend, a stronger dependence of phase separation rate on the thermodynamic driving force was observed in the PS/PVME (2/8) with 2 vol% silica nanoparticles. The results of apparent activation energy strongly confirmed the interfacial adhesion of silica nanoparticles in PS/PVME blends.

Acknowledgements

Financial support from the program of National Natural Science Foundation of China (Grant no. 50673104 and 50673101) and Natural Science Foundation of Guangdong province (Grant no. 7003702) are gratefully acknowledged.

References

[1] Kwei T. K., Nishi T., Roberts R. F.: A study of compatible polymer mixtures. Macromolecules, **7**, 667–674 (1974).
DOI: 10.1021/ma60041a023

[2] Nishi T., Wang T. T., Kwei T. K.: Thermally induced phase separation behavior of compatible polymer mixtures. Macromolecules, **8**, 227–234 (1975).
DOI: 10.1021/ma60044a025

[3] Hashimoto T., Kumaki J., Kawai H.: Time-resolved light scattering studies on kinetics of phase separation and phase dissolution of polymer blends. 1. Kinetics of phase separation of a binary mixture of polystyrene and poly(vinyl methyl ether). Macromolecules, **16**, 641–648 (1983).
DOI: 10.1021/ma00238a030

[4] Snyder H. L., Meakin P., Reich S.: Dynamical aspects of phase separation in polymer blends. Macromolecules, **16**, 757–762 (1983).
DOI: 10.1021/ma00239a011

[5] Hill R. G., Tomlins P. E., Higgins J. S.: Preliminary study of the kinetics of phase separation in high molecular weight poly(methyl methacrylate)/solution-chlorinated polyethylene blends. Macromolecules, **18**, 2555–2560 (1985).
DOI: 10.1021/ma00154a033

[6] Kumaki J., Hashimoto T.: Time-resolved light scattering studies on kinetics of phase separation and phase dissolution of polymer blends. 4. Kinetics of phase dissolution of a binary mixture of polystyrene and poly (vinyl methyl ether). Macromolecules, **19**, 763–768 (1986).
DOI: 10.1021/ma00157a046

[7] Ginzburg V. V., Qiu F., Paniconi M., Peng G., Jasnow D., Balazs A. C.: Simulation of hard particles in a phase-separating binary mixture. Physical Review Letters, **82**, 4026–4029 (1999).
DOI: 10.1103/PhysRevLett.82.4026

[8] Ginzburg V. V., Peng G., Qiu F., Jasnow D., Balazs A. C.: Kinetic model of phase separation in binary mixtures with hard mobile impurities. Physical Review E, **60**, 4352–4359 (1999).
DOI: 10.1103/PhysRevE.60.4352

[9] Balazs A. C., Ginzburg V. V., Qiu F., Peng G., Jasnow D.: Multi-scale model for binary mixtures containing nanoscopic particles. The Journal of Physical Chemistry B, **104**, 3411–3422 (2000).
DOI: 10.1021/jp993356+

[10] Zhu Y-J., Ma Y-Q.: Phase separation of a polymer blend driven by oscillating particles. Physical Review E, **67**, 041503/1–041503/7 (2003).
DOI: 10.1103/PhysRevE.67.041503

[11] Laradji M., MacNevin G.: Phase separation dynamics in binary fluids containing quenched or mobile filler particles. The Journal of Chemical Physics, **119**, 2275–2283 (2003).
DOI: 10.1063/1.1585011

[12] Laradji M.: A Langevin dynamics study of mobile filler particles in phase-separating binary systems. The Journal of Chemical Physics, **120**, 9330–9334 (2004).
DOI: 10.1063/1.1704636

[13] Nesterov A. E., Lipatov Y. S., Horichko V. V., Gritsenko O. T.: Filler effects on the compatibility and phase separation kinetics of poly(vinyl acetate)-poly(methyl methacrylate) mixtures. Polymer, **33**, 619–622 (1992).
DOI: 10.1016/0032-3861(92)90740-N

[14] Nesterov A. E., Lipatov Y. S.: Compatibilizing effect of a filler in binary polymer mixtures. Polymer, **40**, 1347–1349 (1999).
DOI: 10.1016/S0032-3861(98)00277-8

[15] Lipatov Y. S., Nesterov A. E., Ignatova T. D., Nesterov D. A.: Effect of polymer–filler surface interactions on the phase separation in polymer blends. Polymer, **43**, 875–880 (2002).
DOI: 10.1016/S0032-3861(01)00632-2

[16] Ginzburg V. V.: Influence of nanoparticles on miscibility of polymer blends. A simple theory. Macromolecules, **38**, 2362–2367 (2005).
DOI: 10.1021/ma0482821

[17] El-Mabrouk K., Belaiche M., Bousmina M.: Phase separation in PS/PVME thin and thick films. Journal of Colloid and Interface Science, **306**, 354–367 (2007).
DOI: 10.1016/j.jcis.2006.10.051

[18] Wignall G. D., Alamo R. G., Londono J. D., Mandelkern L., Stehling F. C.: Small-angle neutron scattering investigations of liquid-liquid phase separation in heterogeneous linear low-density polyethylene. Macromolecules, **29**, 5332–5335 (1996).
DOI: 10.1021/ma960050h

[19] Jha A., Bhowmick A. K.: Mechanical and dynamic mechanical thermal properties of heat- and oil-resistant thermoplastic elastomeric blends of poly(butylene terephthalate) and acrylate rubber. Journal of Applied Polymer Science, **78**, 1001–1008 (2000).
DOI: 10.1002/1097-4628(20001031)78:5<1001::AID-APP90>3.0.CO;2-G

[20] Swier S., Van Durme K., Van Mele B.: Modulated-temperature differential scanning calorimetry study of temperature-induced mixing and demixing in poly (vinylmethylether)/water. Journal of Polymer Science Part B: Polymer Physics, **41**, 1824–1836 (2003).
DOI: 10.1002/polb.10512

[21] Cabral J. T., Higgins J. S., McLeish T. C. B., Strausser S., Magonov S. N.: Bulk spinodal decomposition studied by atomic force microscopy and light scattering. Macromolecules, **34**, 3748–3756 (2001).
DOI: 10.1021/ma0017743

[22] Klopffer M-H., Bokobza L., Monnerie L.: Structural side effects in the use of a fluorescent probe for monitoring polymer mobility. Macromolecules, **31**, 8291–8296 (1998).
DOI: 10.1021/ma980717v

[23] Olmos D., González-Benito J.: Cure process and reaction-induced phase separation in a diepoxy–diamine/PMMA blend. Monitoring by steady-state fluorescence and FT-IR (near and medium range). Colloid and Polymer Science, **284**, 654–667 (2006).
DOI: 10.1007/s00396-005-1434-y

[24] Corrales T., Peinado C., Bosch P., Catalina F.: Study of secondary relaxations of poly(ethylene terephthalate) by photoluminescence technique. Polymer, **45**, 1545–1554 (2004).
DOI: 10.1016/j.polymer.2003.12.051

[25] Halary J. L., Ubrich J. M., Monnerie L., Yang H., Stein R. S.: Isotope effects on the phase separation in polystyrene-poly(vinylmethylether) blends. Polymer Communications, **26**, 73–76 (1985).

[26] Zhang M. Q.: Intrinsic fluorescence: An effective means to monitor macromolecular chain motions. Express Polymer Letters, **2**, 835 (2008).
DOI: 10.3144/expresspolymlett.2008.97

[27] Tsai F. J., Torkelson J. M.: Phase separation of oligomeric polystyrene-polybutadiene blends as studied by excimer fluorescence. Macromolecules, **21**, 1026–1033 (1988).
DOI: 10.1021/ma00182a031

[28] Clauss B., Salem D. R.: A chain-intrinsic fluorescence study of orientation-strain behavior in uniaxially drawn poly(ethylene terephthalate) film. Macromolecules, **28**, 8328–8333 (1995).
DOI: 10.1021/ma00128a049

[29] Ylitalo D. A., Frank C. W.: The effect of pressure on block copolymer micelle formation: Fluorescence and light scattering studies of poly(styrene-b-ethylene propylene) in heptane. Polymer, **37**, 4969–4978 (1996).
DOI: 10.1016/0032-3861(96)00368-0

[30] Sanz A., Mendicuti F.: Excimers in dilute solutions of *N*-vinyl carbazole/styrene copolymers of different molar compositions. Polymer, **43**, 6123–6130 (2002).
DOI: 10.1016/S0032-3861(02)00584-0

[31] Yang H., Shibayama M., Stein R. S., Shimizu N., Hashimoto T.: Deuteration effects on the miscibility and phase separation kinetics of polymer blends. Macromolecules, **19**, 1667–1674 (1986).
DOI: 10.1021/ma00160a032

[32] Wagler T., Rinaldi P. L., Han C. D., Chun H.: Phase behavior and segmental mobility in binary blends of polystyrene and poly(vinyl methyl ether). Macromolecules, **33**, 1778–1789 (2000).
DOI: 10.1021/ma9909105

[33] Shibayama M., Stein R S., Han C. C.: Study of miscibility and critical phenomena of deuterated polystyrene and hydrogenated poly(vinyl methyl ether) by small-angle neutron scattering. Macromolecules, **18**, 2179–2187 (1985).
DOI: 10.1021/ma00153a020

[34] Vala M. T., Haebig J., Rice S. A.: Experimental study of luminescence and excitation trapping in vinyl polymers, paracyclophanes, and related compounds. The Journal of Chemical Physics, **43**, 886–897 (1965).
DOI: 10.1063/1.1696866

[35] Torkelson J. M., Lipsky S., Tirrell M.: Polystyrene fluorescence: Effects of molecular weight in various solvents. Macromolecules, **14**, 1601–1603 (1981).
DOI: 10.1021/ma50006a094

[36] Torkelson J. M., Lipsky S., Tirrell M., Tirrell D. A.: Fluorescence and absorbance of polystyrene in dilute and semidilute solutions. Macromolecules, **16**, 326–330 (1983).
DOI: 10.1021/ma00236a031

[37] Frank C. W., Harrah L. A.: Excimer formation in vinyl polymers. II. Rigid solutions of poly(2-vinylnaphthalene) and polystyrene. The Journal of Chemical Physics, **61**, 1526–1541 (1974).
DOI: 10.1063/1.1682097

[38] Frank C. W.: Excimer formation in vinyl polymers. III. Fluid and rigid solutions of poly(4-vinylbiphenyl). The Journal of Chemical Physics, **61**, 2015–2022 (1974).
DOI: 10.1063/1.1682204

[39] Frank C. W.: Observation of relaxation processes near the glass transition by means of excimer fluorescence. Macromolecules, **8**, 305–310 (1975).
DOI: 10.1021/ma60045a012

[40] Birks J. B.: Photophysics of aromatics molecules. Wiley, New York (1970).

[41] Beaucage G., Composto R., Stein R. S.: Ellipsometric study of the glass transition and thermal expansion coefficients of thin polymer films. Journal of Polymer Science Part B: Polymer Physics, **31**, 319–326 (1993).
DOI: 10.1002/polb.1993.090310310

[42] Turrión S. G., Olmos D., Ekizoglou N., González-Benito J.: Fluorescence response from anthracene labeled polystyrene to study its thermal transitions. Polymer, **46**, 4023–4031 (2005).
DOI: 10.1016/j.polymer.2005.03.056

[43] Mundra M. K., Ellison C. J., Behling R. E., Torkelson J. M.: Confinement, composition, and spin-coating effects on the glass transition and stress relaxation of thin films of polystyrene and styrene-containing random copolymers: Sensing by intrinsic fluorescence. Polymer, **47**, 7747–7759 (2006).
DOI: 10.1016/j.polymer.2006.08.064

[44] Frank C. W., Gashgari M. A.: Excimer fluorescence as a molecular probe of polymer blend compatibility. 1. Blends of poly(2-vinylnaphthalene) with poly(alkyl methacrylates). Macromolecules, **12**, 163–165 (1979).
DOI: 10.1021/ma60067a038

[45] Yurekli K., Karim A., Amis E. J., Krishnamoorti R.: Phase behavior of PS–PVME nanocomposites. Macromolecules, **37**, 507–515 (2004).
DOI: 10.1021/ma0302098

[46] Gharachorlou A., Goharpey F.: Rheologically determined phase behavior of LCST blends in the presence of spherical nanoparticles. Macromolecules, **41**, 3276–3283 (2008).
DOI: 10.1021/ma7020985

[47] Ginzburg V. V., Qiu F., Paniconi M., Peng G., Jasnow D., Balazs A. C.: Simulation of Hard particles in a phase-separating binary mixture. Physical Review Letters, **82**, 4026–4029 (1999).
DOI: 10.1103/PhysRevLett.82.4026

[48] McMaster L. P.: Aspects of polymer-polymer thermodynamics. Macromolecules, **6**, 760–773 (1973).
DOI: 10.1021/ma60035a024

[49] Shlyapnikov Y. A., Bogaevskaya T. A., Kiryushkin S. G., Monakhova T. V.: Specific features of formation and properties of hydroperoxides of polyolefins. European Polymer Journal, **15**, 737–742 (1979).
DOI: 10.1016/0014-3057(79)90024-7

[50] Zlatkevich L.: A chemiluminescence technique for the evaluation of the thermal oxidative stability of polyethylene. Polymer Degradation and Stability, **19**, 51–60 (1987).
DOI: 10.1016/0141-3910(87)90012-7

[51] Benson S. W.: The foundations of chemical kinetics. McGraw-Hill, New York (1960).

[52] Larbi F. B. C., Halary J. L., Monnerie L.: Kinetics of phase separation in binary mixtures of polystyrene and poly(vinyl methyl ether) as studied by fluorescence emission of labeled polystyrene. Macromolecules, **24**, 867–871 (1991).
DOI: 10.1021/ma00004a009

[53] El Mabrouk K., Bousmina M.: Assessment of morphology in transient and steady state regimes resulting from phase separation in polystyrene/poly(vinyl methyl ether) blend. Rheologica Acta, **45**, 877–889 (2006).
DOI: 10.1007/s00397-005-0076-9

[54] Langer J. S., Bar-on M., Miller H. D.: New computational method in the theory of spinodal decomposition. Physical Review A, **11**, 1417–1429 (1975).
DOI: 10.1103/PhysRevA.11.1417

[55] Yang J., Chen X., Fu R., Luo W-L., Li Y., Zhang M.: Kinetics of phase separation in polymer blends revealed by resonance light scattering spectroscopy. Physical Chemistry Chemical Physics, **12**, 2238–2245 (2010).
DOI: 10.1039/b918069a

eXPRESS Polymer Letters Vol.5, No.9 (2011) 809–818
Available online at www.expresspolymlett.com
DOI: 10.3144/expresspolymlett.2011.79

Effects of graphene oxides on the cure behaviors of a tetrafunctional epoxy resin

S. L. Qiu[1], C. S. Wang[1], Y. T. Wang[1], C. G. Liu[2], X. Y. Chen[1], H. F. Xie[1,], Y. A. Huang[3], R. S. Cheng[1,4]*

[1]Key Laboratory for Mesoscopic Chemistry of Ministry of Education, Department of Polymer Science and Engineering, School of Chemistry and Chemical Engineering, Nanjing University, Nanjing 210093, China
[2]Institute of Chemical Industry of Forest Products, Chinese Academy of Forestry, Key Open Lab of Forest Chemical Engineering, State Forestry Administration, Nanjing 210042, China
[3]School of Material Engineering, Nanjing Institute of Technology, Nanjing 211167, China
[4]College of Material Science and Engineering, South China University of Technology, Guangzhou 510640, China

Received 21 January 2011; accepted in revised form 22 March 2011

Abstract. The influence of graphene oxides (GOs) on the cure behavior and thermal stability of a tetrafunctional tetraglycidyl-4,4'-diaminodiphenylmethane cured with 4,4'-diaminodiphenylsulfone was investigated by using dynamic differential scanning calorimetry (DSC) and thermogravimetric analysis (TGA). The dynamic DSC results showed that the initial reaction temperature and exothermal peak temperature decreased with the increase of GO contents. Furthermore, the addition of GO increased the enthalpy of epoxy cure reaction. Results from activation energy method showed that activation energies of GO/epoxy nanocomposites greatly decreased with the GO content in the latter stage, indicating that GOs significantly hindered the occurrence of vitrification. The oxygen functionalities, such as hydroxyl and carboxyl groups, on the surface of GOs acted as catalysts and facilitated the curing reaction and the catalytic effect increased with the GO contents. TGA results revealed that the addition of GOs decreased the thermal stability of epoxy.

Keywords: *nanocomposites, thermal properties, thermosetting resin, graphene oxide, epoxy resin*

1. Introduction

Epoxy resins are the most important thermosets, widely used as adhesives, coatings, and composite materials due to their low density, good thermal, electrical and mechanical properties. However, some advanced applications need further improvement of multifunctional properties, such as mechanical properties, thermal expansion, thermal and electrical conductivity. Therefore, reinforced fillers, such as carbon black, glass fibers and carbon fibers, have been incorporated into the resins [1].

As carbon-based nanofillers for epoxy nanocomposites, carbon nanotubes (CNTs) and carbon nanofibers (CNFs), which have small dimensions and high aspect ratios, have been received much attention as fillers with potential for use in many applications due to their remarkable physical, chemical, and electrical properties. CNT- and CNF-reinforced epoxy nanocomposites have shown improved mechanical, electrical and thermal properties [2–5]. However, the high cost of CNTs and CNFs and the poor dispersion in the epoxy limits their range of practical applicability.

Currently, graphite oxides, which consists a layered structure of graphene oxide (GOs) sheets and can be completely exfoliated to produce aqueous colloidal suspension of GO sheets by simple sonication in aqueous and organic solvents, have received considerable amount of attention in the area of polymer nanocomposites due to their inexpensive

*Corresponding author, e-mail:hfxie@nju.edu.cn

and feasible substitute for CNTs and CNFs [6–10]. GOs, which have been demonstrated containing many epoxy groups [11], might make an ideal filler for epoxy resin which also contains epoxy groups, on the basis of the principle of dissolution in a similar material structure. Recently, Yang *et al.* [12] prepared GO/epoxy nanocomposites through two-phase extraction. Great improvements in mechanical properties such as compressive failure strength and toughness have been achieved for the chemically converted GO/epoxy resin for a 0.0375 wt% loading of chemically converted GO sheets in epoxy resin by 48.3 and 1185.2%, respectively.

The study of the cure kinetics is of great importance in epoxy curing process. In particular, the study of the cure reactions of epoxy as a function of the processing conditions, from a kinetic point of view, is very important for the analysis and design of processing operations. Differential scanning calorimetry (DSC) may be considered as one of the most interesting techniques for kinetic analysis of cure reactions of thermosetting systems [13–15]. Numerous studies on cure kinetics of epoxy in presence of carbon-based nanofillers have been investigated [16–25]. Recently, Allaoui and El Bounia [16] had reviewed the influence of CNTs on the cure kinetics of epoxy resin. Our previous studies showed that the addition of CNTs could accelerate the cure reaction of epoxy resin, while CNFs had only a negligible effect on the cure kinetics of the epoxy [17, 18]. Abdalla *et al.* [19] investigated the effect of carboxyl and fluorine surface modification of multi-walled carbon nanotubes (MWCNTs) on the cure behavior of epoxy resins with the modified CNTs, and reported that the activation energy and rate constant were not affected by the fluorine modification whereas the resins with carboxylated MWCNTs exhibited an increase in the activation energy and a lower rate constant for the cure reaction. Zhou *et al.* [20–22] studied the effects of MWCNTs and carboxylic functionalization of MWCNTs on the cure reaction of epoxy. They reported that MWCNTs had an accelerating effect in the initial curing stage, whereas in the later curing stage, MWCNTs prevented from the occurrence of vitrification [20]. However, carboxylic functionalization of MWCNTs did not change the autocatalytic cure reaction mechanism of epoxy nanocomposites and had catalytic effect on the curing process [21, 22]. Jana and Zhong [23] found that expanded graphite (EG) did not significantly impede the cure reaction of epoxy. Guo *et al.* [24] reported that at lower concentrations (1 phr) of EG, compared with the curing activation energy (E_α) of the neat epoxy resin, the composite with EG had a lower E_α before the gelation and a higher E_α after the gelation. At higher concentrations of EG, however, in the whole conversion range, the composite with EG showed a higher E_α compared with the neat epoxy resin.

The tetrafunctional epoxy resin tetraglycidyl-4,4'-diaminodiphenylmethane (TGDDM) cured with the aromatic diamine 4,4'-diaminodiphenylsulfone (DDS), is one of the most widely employed matrices for the production of high performance fiber composites in the aircraft and spacecraft industries. The attractive features of this thermosetting resin are its low density combined with high tensile strength and modulus, and a very high glass transition temperature combined with good thermal and chemical resistance [26]. In present work, GO prepared with Hummers method was incorporated into the tetrafunctional epoxy systems as carbon-based nanofiller. Dynamic DSC was used to investigate the influence of GOs on the cure reaction of TGDDM/DDS nanocomposites. Furthermore, the thermal stability and morphology of GO/epoxy nanocomposites were studied.

2. Experimental

2.1. Materials

The epoxy resin used in this study was TGDDM, AG80, with a weight per epoxy equivalent of 120 g/equiv., from Shanghai Synthetic Resin Institute (Shanghai, China). The curing agent was DDS, with a molecular mass of 248.31 and purity >99% according to the supplier, Petroleum and Chemical Factory of Fudan University (Shanghai, China). Natural graphite flakes, supplied by Guyu Graphite Co. Ltd. (Qingdao, China), is 80 mesh, equal to 250 μm.

2.2. Sample preparation

GO was obtained by harsh oxidation of the graphite flakes according to the Hummers method [27]. After purification, the product was put in a vacuum desiccator for a week. The final product was added to ethanol and sonicated until it became clear with no visible particulate matter. The suspension was

then added to TGDDM resin and sonicated for 2 h. Subsequently, the ethanol was evaporated off by heating the mixture on a magnetic stir plate using a Teflon-coated magnetic bar for 3 h at 70°C. Next, the mixture was placed in a vacuum chamber for 12 h at 70°C to ensure that all of ethanol had been removed. Then, the mixture was placed in an oil bath at 120°C and a stoichiometric amount of DDS was slowly added, under continuous mechanical stirring, until a homogeneous mixture was observed which took about 10 min. Several DSC aluminum pans were filled with the reaction mixture. The samples (~10 mg) were then cooled and stored in a freezer until required. The weight fractions of GOs in the TGDDM/DDS system were 1, 2 and 5 wt %, respectively.

2.3. Characterization

The Fourier-transform infrared (FT-IR) spectra of the natural graphite flakes and GO were recorded on a Nicolet iS10 FT-IR spectrometer using the attenuated total reflectance (ATR) technique (Thermo Scientific, USA). The spectrum was scanned 64 times at a resolution of 4 cm^{-1}.

The analyses of the X-ray photoelectron spectra (XPS) were carried out on a ESCALAB 250 X-ray photoelectron spectroscope (Thermo Scientific, USA) equipped with a monochromatic Al K_α (1486.6 eV) source and a pass energy of 20 eV.

A Pyris 1 DSC (PerkinElmer, USA) was used for the dynamic curing experiments and data analysis under an argon flow of 20 ml/min. The dynamic DSC experiments were conducted at heating rates of 2.5, 5, 10, and 20°C/min over a temperature range of 50–300°C. The reaction was considered to be complete when the rate curve leveled off to a baseline. The total area under the exothermal curve, based on the extrapolated baseline at the end of the reaction, was used to calculate the total heat of reaction, ΔH [J/g].

Thermogravimetric analysis (TGA) was completed on a Pyris 1 TGA (Perkin Elmer, USA) with a heating rate of 20°C/min under N_2 atmosphere from 25 to 700°C.

The fracture surfaces of samples were observed at 10 kV with a field emission scanning electron microscopy (FE-SEM, Hitachi S-4800, Japan). The cured samples were fractured under liquid nitrogen, and then the fractured surfaces were vacuum-coated with a thin gold layer.

3. Results and discussion

3.1. Characterization of GOs

The high degree of GO oxidation was confirmed by XPS: the survey spectra for pristine graphite and GO (not shown) yielded C/O atomic ratios of 30.7 and 2.3, respectively. Figure 1 shows the C1s XPS spectra of the pristine graphite and GO. The narrow, asymmetric C1s band characteristic of pristine graphite (a) transforms into a complex band showing three maxima for GO (b), as expected, due to the high percentage of oxygen functionalities. The C1s XPS spectrum of graphene oxide (Figure 1b) clearly indicates a considerable degree of oxidation with three components that correspond to carbon atoms in different functional groups: the non-oxygenated ring C (284.5 eV), the C in C–O bonds (286.6 eV), and the carboxylate carbon (O–C=O, 288.5 eV) [28].

The FT-IR spectra of the pristine graphite and GO are presented in Figure 2. The baselines of FT-IR spectra of conducting materials have a tendency to tilt. Since graphite is a conducting material, the baseline is slanted [15]. From the spectrum of pristine graphite it is obvious that there was a negligible amount of hydroxyl, C=O, or C–O groups in the

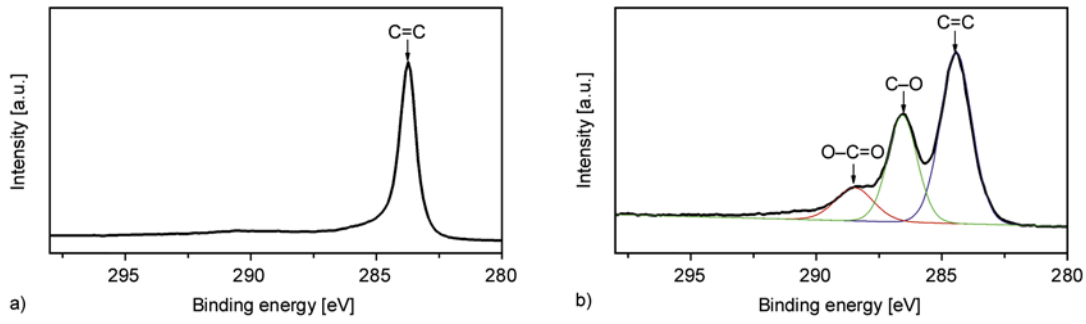

Figure 1. C1s XPS spectra for the pristine graphite (a) and GO (b)

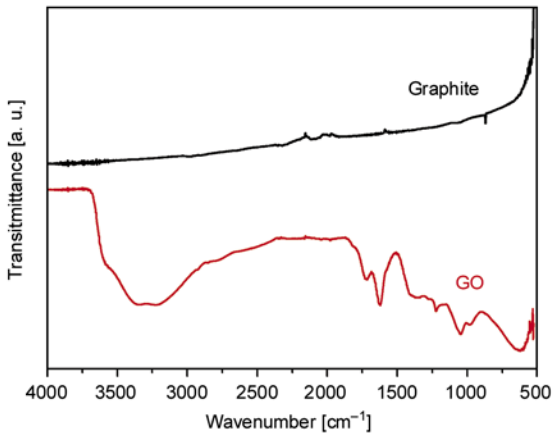

Figure 2. FT-IR spectra for the pristine graphite and GO

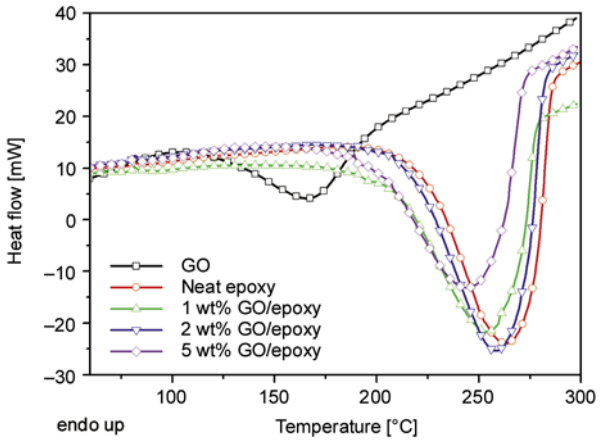

Figure 3. Dynamic DSC curves for neat epoxy and GO/epoxy nanocomposites at a heating rate of 20°C/min

pristine graphite. The most prominent features in the spectrum of GOs are the adsorption bands corresponding to the O–H stretching vibrations at 3428 cm^{-1}, the C=O carbonyl stretching at 1733 cm^{-1}, the phenol C=C ring stretching at 1621 cm^{-1}, the C–O stretching at 1053 cm^{-1}, and the C–OH stretching, presumably from phenols, at 1226 cm^{-1}. Other researchers also observed similar functional groups [11, 28, 29]. Thus, similar to XPS, FTIR spectra provided the evidence of the presence of different types of oxygen functionalities on the GO material, which could affect the cure reaction of the epoxy resin.

3.2. Effects of GOs on the cure reaction

The dynamic DSC curves for the pure GO and GO/TGDDM/DDS nanocomposites at a heating rate of 20°C/min are shown in Figure 3. DSC of GO shows one strong extherthomic peak at 166°C, which was caused by the decomposition of the organic groups on the GO sheets and evolution of H_2O, CO and CO_2 [30]. It is obvious that GO has an accelerating effect on the curing process of TGDDM/DDS nanocomposites with a trend of cure reaction peaks towards lower temperatures. The initial reaction temperature (T_i), exothermal peak temperature (T_p) and ΔH of GO/epoxy nanocomposites at different heating rates are list in Table 1. It can be observed that both T_i and T_p decrease with the increase of GO contents, indicating that the GOs act as catalysts and facilitate the curing reaction and the catalytic effect increases with the GO contents. The enthalpies of GO/epoxy nanocomposites vary with the GO contents, if they are converted to average kilojoules

Table 1. The initial reaction temperature (T_i), exothermal peak temperature (T_p) and total heat of reaction (ΔH) of GO/epoxy nanocomposites at different heating rates

GO [wt%]	Heating rate [°C/min]	T_i [°C]	T_p [°C]	ΔH [J/g]	$\overline{\Delta H}$ [J/g]	$\overline{Q_0}$ [kJ/mol epoxide]
0	2.5	155.4	196.5	629.5	658.6	120.7
	5.0	161.2	213.1	651.9		
	10.0	162.9	234.8	653.5		
	20.0	173.4	262.8	699.5		
1	2.5	120.4	192.3	654.6	654.3	121.2
	5.0	137.6	212.3	645.2		
	10.0	161.8	234.8	628.7		
	20.0	166.3	258.3	688.7		
2	2.5	135.0	189.4	660.0	660.1	123.5
	5.0	137.1	210.8	669.9		
	10.0	142.7	230.8	645.1		
	20.0	161.3	253.4	665.5		
5	2.5	113.3	188.9	620.1	631.3	121.2
	5.0	131.7	203.8	651.9		
	10.0	133.4	225.6	615.0		
	20.0	136.5	244.3	638.0		

per equivalent of epoxide ($\overline{Q_0}$), it can be seen that the addition of GO increases the enthalpy of epoxy cure reaction. Furthermore, it can be also observed that no linear relationship of enthalpies between different contents of GO. The influence of carbon-based nano-fillers on the enthalpies of the epoxy cure reaction is different for different nanocomposites. The addition of CNTs [19, 20, 31] and EG [24] decreased the ΔH of epoxy, whereas CNF had no pronounced effect on the heat of the TGDDM/DDS cure reaction [32] and silanized and polyaniline modified CNFs increased the ΔH of epoxy [33, 34]. It is believed that the addition of hydroxyl-containing compounds (water, alcohols, phenols, acids) considerably promoted the interaction of epoxy compounds with amines and other nucleophilic reagents [35]. In this case, the epoxy ring carbon atom became more sensitive to nucleophilic attack. The epoxy-oligomer curing with amines had an autocatalytic character due to the accumulation of hydroxyl groups during the reaction. According to recent studies [36], GOs have their basal planes decorated mostly with epoxide and hydroxyl groups, in addition to carbonyl and carboxyl groups located presumably at the edges (Lerf-Klinowski model), which agreed well with the results of XPS and FT-IR discussed above. Gao *et al*. [37] proposed that GO contains ketones, 6-membered lactol rings, and tertiary alcohol in addition to epoxide and hydroxyl groups. Therefore, it can be concluded that these different types of oxygen functionalities on the surface of GOs are considered as catalysts to accelerate the cure reaction between epoxide and amine groups.

Figure 4 shows the conversions of reaction (α) as a function of temperature for neat epoxy and GO/epoxy nanocomposites at a heating rate of 20°C/min. It can be observed that all curves show a sigmoidal form, which indicates that the cure reaction of TGDDM/DDS system is autocatalytic in agreement with our previous studies [17, 18]. Consequently, the incorporation of GOs has no influence on the cure reaction mechanism of the TGDDM/DDS system. Notably, from Figure 4, α of GO/epoxy composite increases with the GO contents and is higher than that of neat epoxy. These results further confirm that GOs act as catalysts in the cure reaction of epoxy and the catalytic effect increases with the GO contents.

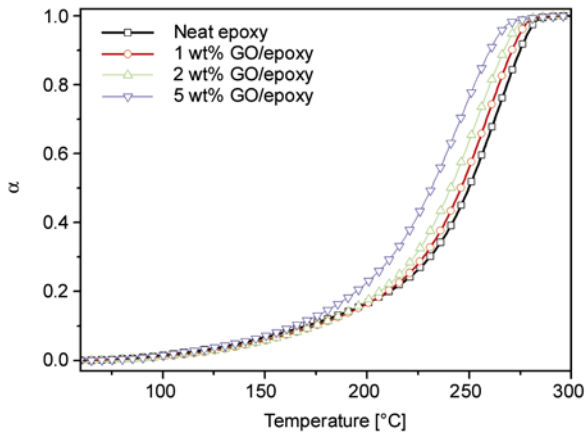

Figure 4. The conversions of reaction (α) as a function of temperature for neat epoxy and GO/epoxy nanocomposites at a heating rate of 20°C/min

3.3. Effects of GOs on the activation energy

To further investigate the effect of GOs on the activation energy of TGDDM/DDS system, kinetic analysis of dynamic DSC results was carried out. During a cure reaction, the reaction rate ($d\alpha/dt$) as a function of time (t) was calculated from the measured heat flow (dH/dt) in dynamic DSC experiments, by Equation (1):

$$\frac{d\alpha}{dt} = \frac{\frac{dH}{dt}}{\Delta H} = k(T)f(\alpha) \tag{1}$$

where T is the temperature, $f(\alpha)$ is the reaction model and $k(T)$ is the rate constant, which follows Arrhenius equation (see Equation (2)):

$$k(T) = A\exp\left(\frac{-E_\alpha}{RT}\right) \tag{2}$$

where A is the pre-exponential factor, E_α is the activation energy and R is the gas constant.

Thus, Equation (1) can be replaced by Equation (3):

$$\frac{d\alpha}{dt} = A\exp\left(\frac{-E_\alpha}{RT}\right)f(\alpha) \tag{3}$$

so that the modified form of Equation (3) is given (see Equation (4)):

$$\ln\left(\frac{d\alpha}{dt}\right) = \ln[Af(\alpha)] - \left(\frac{E_\alpha}{RT}\right) \tag{4}$$

It is expected that the curve of $\ln(d\alpha/dt)$ versus $(1/T)$ would be a straight line with slope E_α/R and an intercept of $\ln[Af(\alpha)]$. The data points for each straight line were obtained from dynamic DSC

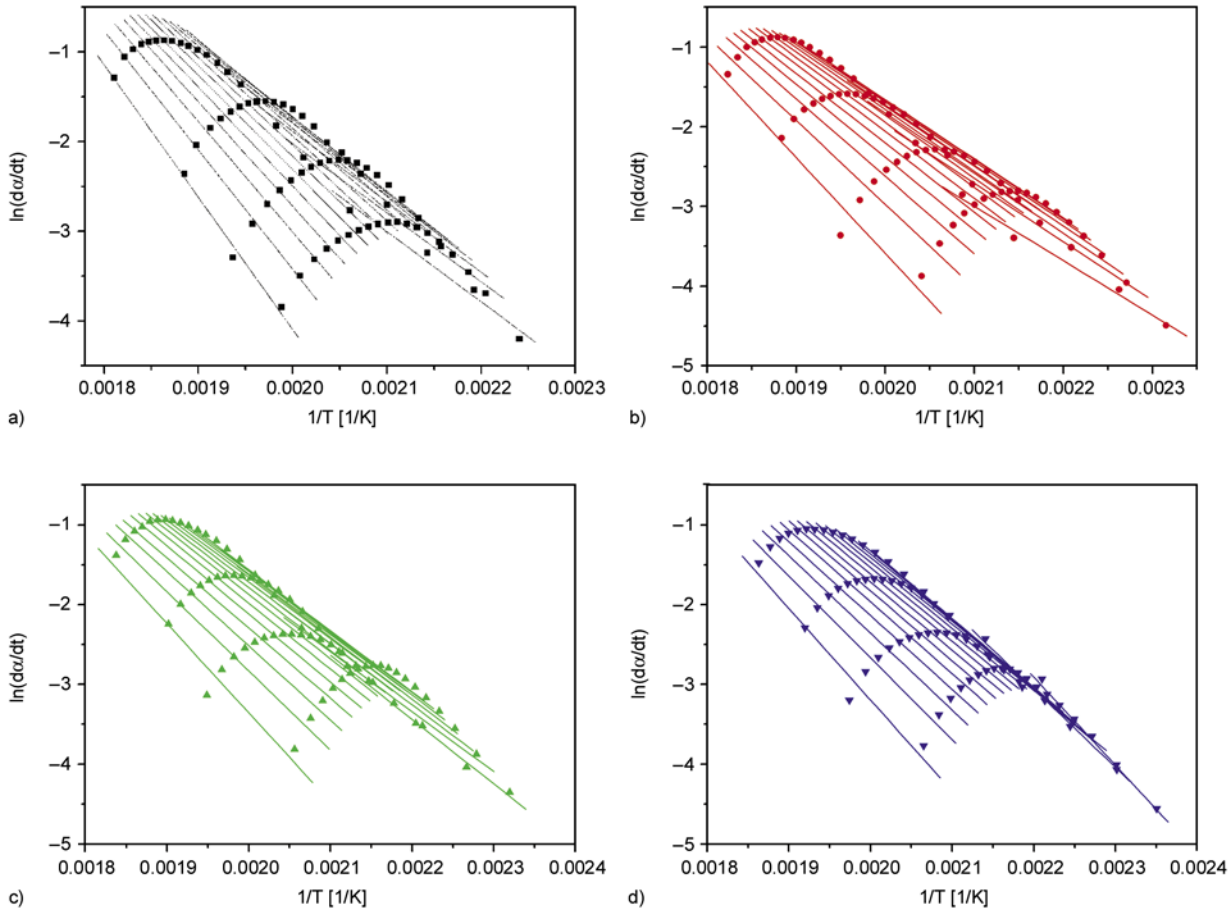

Figure 5. ln(dα/dt) versus 1/T curves for (a) neat epoxy, (b) 1 wt% GO/epoxy, (c) 2 wt% GO/epoxy, (d) 5 wt% GO/epoxy nanocomposites

curves at different heating rates considering same fractional conversion of reaction (α). By repeating the procedure, the values of E_α and ln[$Af(\alpha)$] corresponding to different α were acquired. Figure 5 presents the curves of ln(dα/dt) versus (1/T) for the neat epoxy and the GO/epoxy nanocomposites, respectively. A set of α was considered from the full range of experimental data, i.e. α = 0.05, 0.10, 0.15, …, 0.90 and 0.95. Using linear regression method on each set of data linked to a particular α, the values of E_α and ln[$Af(\alpha)$] were obtained.

Figure 6 shows the curve of E_α versus α for the neat epoxy and the GO/epoxy nanocomposites. From the figures it can be seen that for the neat epoxy increases gradually with during the whole curing process whereas E_α increases significantly when α is higher than 0.55, which can be regarded as gel point of the TGDDM/DDS system [38]. Due to the catalytic effect of hydroxyls on the surface of GOs, the incorporation of GOs greatly decreases the activation energy of the neat epoxy during the whole

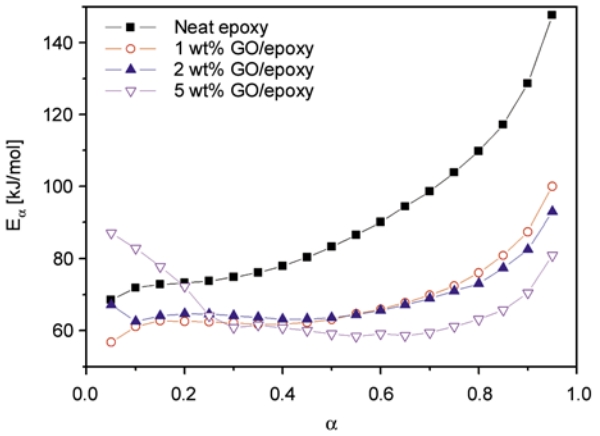

Figure 6. E_α as a function of α for the neat epoxy and GO/epoxy nanocomposites. Straight lines are given only for showing the tendency

curing process except for the initial stage of 5 wt% GO/epoxy nanocomposites (α < 0.2). Furthermore, E_α of GO/epoxy nanocomposites decrease with the increase of GO content when conversion is greater than 0.5, indicating that higher contents of hydroxyl groups accelerate the interaction between the active

reactants in the stage of diffusion control. Namely, the oxygen functionalities of GOs significantly hinder the occurrence of vitrification (diffusion control) of epoxy. In addition, the hindering effect increases with the increase of GO contents due to the increase of hydroxyl groups on the GOs.

3.4. Effects of GOs on the thermal stability

Figure 7a shows the TGA curves of GO and its epoxy nanocomposites, together with their derivative (i.e. the so-called differential thermogravimetric (DTG) curves, shown in Figure 7b). For GO, the main mass loss (~30%) takes place around 200°C and is ascribed to the decomposition of labile oxygen functional groups present in the material. There is also a mass loss (~15%) below 100°C attributed to the removal of adsorbed water and a slower, steady mass loss (~20%) over the whole temperature range above 300°C, which can be assigned to the removal of more stable oxygen functionalities. These results agree well with previous reports in the literature for graphite oxide [28, 29]. The initial decomposition temperature (IDT), which is assumed to the temperature of 5 wt% weight loss, is shown in Table 2. As observed, the addition of GO decreases the IDT of epoxy, which indicates that the existence of GO with oxygen functionalities decreases the thermal stability of epoxy resin, and the IDT of the GO/epoxy nanocomposites decreases the increase of GO contents. Furthermore, it can also be observed that the residues at 580°C increase with the rise of GO contents, because of the more carbon-based nanofillers in the nanocomposites.

As can be seen in the DTG curves (Figure 7b), the thermal degradation of neat epoxy and GO/epoxy nanocomposites are characterized by a single stage, indicating the addition of GOs has no influence on decomposition process. For GO/epoxy nanocomposites, the main mass loss (~30%) around 200°C of GO disappears, suggesting a good interaction between oxygen functional groups and epoxy. Furthermore, the temperatures of maximum rate of degradation for epoxy and its GO nanocomposites remain fairly constant.

Table 2. TGA and DTG results for GO and its epoxy nanocomposites

GO [wt%]	IDT [°C]	T_{max} [°C]	Residue at 580°C [%]
100	46.7	220.0	51.2
0	333.3	404.1	24.4
1	331.1	404.7	22.5
2	322.2	404.4	23.4
5	281.5	405.0	25.3

3.5. Dispersion of GOs in epoxy resin

Because of epoxide groups in the chemical structures, compatibility of GOs with epoxy and dispersion in the matrix were sigifcantly improved. Figure 8 shows the fracture micrographs of several freeze-fractured specimens. Fine dispersion of GO in the epoxy is observed. Some irregular protuberances are observed on the composite surface and furthermore, their number increases with increasing GO content. The length and thickness of these protuberances are in a scale range from hundreds of nanometers to several microns. The uniform dispersion of GOs in the epoxy matrix results in a strong catalytic effect by the hydroxyls on the GOs lowers activation energy and decreases the thermal stability of epoxy.

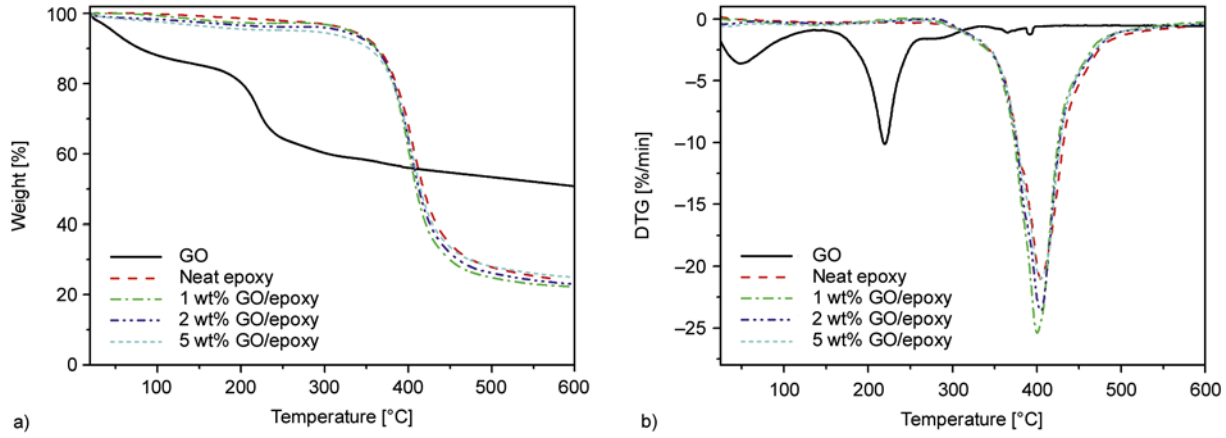

Figure 7. TGA (a) and DTG (b) curves of GOs and GO/epoxy nanocomposites

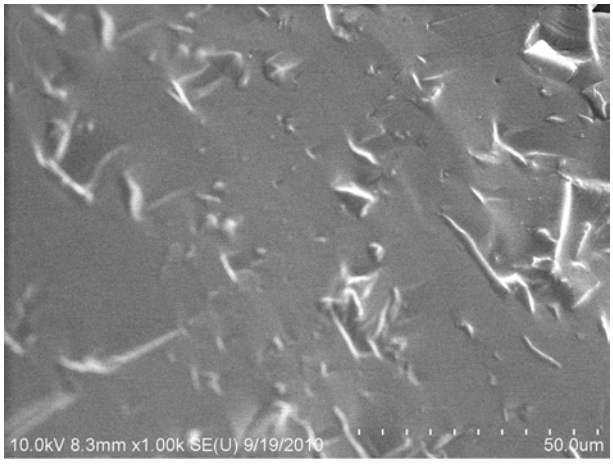

a) 1 wt% GO/epoxy

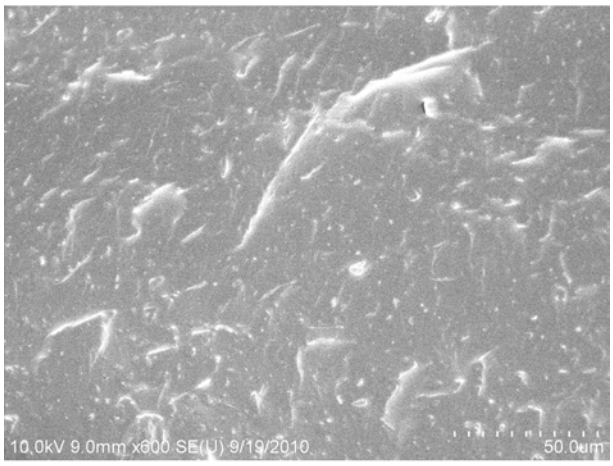

b) 2 wt% GO/epoxy

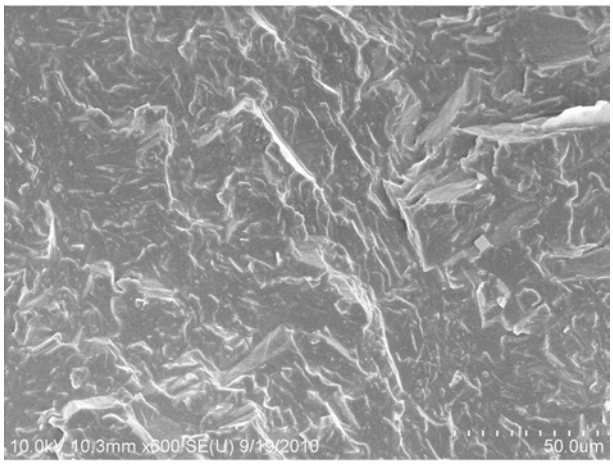

c) 5 wt% GO/epoxy

Figure 8. SEM fracture micrographs of GO/epoxy nanocomposites: (a) 1 wt%, (b) 2 wt% and (c) 5 wt% after quenching in liquid nitrogen

4. Conclusions

The effects of GOs on the cure reaction, thermal stability and morphology of TGDDM/DDS epoxy resin were investigated with dynamic DSC, TGA and SEM. Curing reactions with four different heating rates were analyzed. Furthermore, the functional groups on the surface of GOs were studied with XPS and FT-IR. XPS and FT-IR results showed the presence of different types of oxygen functionalities on the GO. The conversion of cure reaction versus temperature curves in each epoxy system showed the sigmoidal shape, which indicated that the GOs did not change the autocatalytic curing mechanism of TGDDM/DDS system. With the increase of GO content, the initial reaction temperature and exothermal peak temperature decreased. Moreover, the incorporation of GOs increased the enthalpies of the cure reaction. Results on the GO/epoxy systems from the activation energy method indicated that the activation energies were all lower than that of the neat epoxy during the whole curing process, except for the lower conversion of 5 wt% GO/epoxy system ($\alpha < 0.2$). For GO/epoxy nanocomposites, E_α increased with the increase of GO contents in the initial stage of curing process. However, E_α decreased with the increase of GO contents in the latter stage, which indicated that the hindering effect of vitrification for GO/epoxy nanocomposites increased with the increase of GO contents. Therefore, it can be concluded that different types of oxygen functionalities on the surface of the GOs in epoxy significantly catalyzed the cure reaction of the curing process. Furthermore, the catalytic effect increased with the increase of GO contents. The addition of GO decreased the initial decomposition temperature of epoxy, which suggested the existence of GO decreased the thermal stability of epoxy. SEM results showed that GOs was uniformly dispersed in the epoxy due to the existence of epoxide groups on the surface of GOs.

References

[1] Opalički M., Kenny J. M., Nicolais L.: Cure kinetics of neat and carbon-fiber-reinforced TGDDM/DDS epoxy systems. Journal of Applied Polymer Science, **61**, 1025–1037 (1996).
DOI: 10.1002/(SICI)1097-4628(19960808)61:6<1025::AID-APP17>3.0.CO;2-V

[2] Zhou Y. X., Wu P. X., Cheng Z-Y., Ingram J., Jeelani S.: Improvement in electrical, thermal and mechanical properties of epoxy by filling carbon nanotube. Express Polymer Letters, **2**, 40–48 (2008).
DOI: 10.3144/expresspolymlett.2008.6

[3] Romhány G., Szebényi G.: Interlaminar crack propagation in MWCNT/fiber reinforced hybrid composites. Express Polymer Letters, **3**, 145–151 (2009). DOI: 10.3144/expresspolymlett.2009.19

[4] Xie H. F., Liu C. G., Yuan Z. R., Yang H., Wang Z. L., Cheng R. S.: Thermoanalytical studies of high performance epoxy/carbon nanotube composites. Acta Polymerica Sinica, **4**, 332–336 (2008). DOI: 10.3724/SP.J.1105.2008.00332

[5] Spitalsky Z., Tasis D., Papagelis K., Galiotis C.: Carbon nanotube–polymer composites: Chemistry, processing, mechanical and electrical properties. Progress in Polymer Science, **35**, 357–401 (2010). DOI: 10.1016/j.progpolymsci.2009.09.003

[6] Compton O. C., Nguyen S. T.: Graphene oxide, highly reduced graphene oxide, and graphene: Versatile building blocks for carbon-based materials. Small, **6**, 711–723 (2010). DOI: 10.1002/smll.200901934

[7] Dreyer D. R., Park S., Bielawski C. W., Ruoff R. S.: The chemistry of graphene oxide. Chemical Society Reviews, **39**, 228–240 (2010). DOI: 10.1039/b917103g

[8] Zhu Y., Murali S., Cai W., Li X., Suk J. W., Potts J. R., Ruoff R. S.: Graphene and graphene oxide: Synthesis, properties, and applications. Advanced Materials, **22**, 3906–3924 (2010). DOI: 10.1002/adma.201001068

[9] Kim H., Abdala A. A., Macosko C. W.: Graphene/polymer nanocomposites. Macromolecules, **43**, 6515–6530 (2010). DOI: 10.1021/ma100572e

[10] Potts J. R., Dreyer D. R., Bielawski C. W., Ruoff R. S.: Graphene-based polymer nanocomposites. Polymer, **52**, 5–25 (2011). DOI: 10.1016/j.polymer.2010.11.042

[11] Cai W., Piner R. D., Stadermann F. J., Park S., Shaibat M. A., Ishii Y., Yang D., Velamakanni A., An S. J., Stoller M., An J., Chen D., Ruoff R. S.: Synthesis and solid-state NMR structural characterization of ^{13}C-labeled graphite oxide. Science, **321**, 1815–1817 (2008). DOI: 10.1126/science.1162369

[12] Yang H., Shan C., Li F., Zhang Q., Han D., Niu L.: Convenient preparation of tunably loaded chemically converted graphene oxide/epoxy resin nanocomposites from graphene oxide sheets through two-phase extraction. Journal of Materials Chemistry, **19**, 8856–8860 (2009). DOI: 10.1039/b915228h

[13] Menczel J. D., Judovits L., Prime R. B., Bair H. E., Reading M., Swier S.: Differential scanning calorimetry (DSC). in 'Thermal analysis of polymers: Fundamentals and applications' (eds. Menczel J. D., Prime R. B.) Wiley, New Jersey, 130–154 (2009). DOI: 10.1002/9780470423837.ch2

[14] Xie H., Liu B., Sun Q., Yuan Z., Shen J., Cheng R.: The influence of vapor-grown carbon fibers on the cure reaction of epoxy and the curing kinetics of the composites (in Chinese). Acta Polymerica Sinica, **2005**, 891–895 (2005).

[15] Bae J., Jang J., Yoon S-H.: Cure behavior of the liquid-crystalline epoxy/carbon nanotube system and the effect of surface treatment of carbon fillers on cure reaction. Macromolecular Chemistry and Physics, **203**, 2196–2204 (2002). DOI: 10.1002/1521-3935(200211)203:15<2196::AID-MACP2196>3.0.CO;2-U

[16] Allaoui A., El Bounia N.: How carbon nanotubes affect the cure kinetics and glass transition temperature of their epoxy composites? – A review. Express Polymer Letters, **3**, 588–594 (2009). DOI: 10.3144/expresspolymlett.2009.73

[17] Xie H. F., Liu B. H., Yuan Z. R., Shen J. Y., Cheng R. S.: Cure kinetics of carbon nanotube/tetrafunctional epoxy nanocomposites by isothermal differential scanning calorimetry. Journal of Polymer Science Part B: Polymer Physics, **42**, 3701–3712 (2004). DOI: 10.1002/polb.20220

[18] Xie H., Liu B., Sun Q., Yuan Z., Shen J., Cheng R.: Cure kinetic study of carbon nanofibers/epoxy composites by isothermal DSC. Journal of Applied Polymer Science, **96**, 329–335 (2005). DOI: 10.1002/app.21415

[19] Abdalla M., Dean D., Robinson P., Nyairo E.: Cure behavior of epoxy/MWCNT nanocomposites: The effect of nanotube surface modification. Polymer, **49**, 3310–3317 (2008). DOI: 10.1016/j.polymer.2008.05.016

[20] Zhou T., Wang X., Liu X., Xiong D.: Influence of multi-walled carbon nanotubes on the cure behavior of epoxy-imidazole system. Carbon, **47**, 1112–1118 (2009). DOI: 10.1016/j.carbon.2008.12.039

[21] Zhou T., Wang X., Wang T.: Cure reaction of multi-walled carbon nanotubes/diglycidyl ether of bisphenol A/2-ethyl-4-methylimidazole (MWCNTs/DGEBA/EMI-2,4) nanocomposites: Effect of carboxylic functionalization of MWCNTs. Polymer International, **58**, 445–452 (2009). DOI: 10.1002/pi.2558

[22] Zhou T., Wang X., Liu X. H., Lai J. Z.: Effect of silane treatment of carboxylic-functionalized multi-walled carbon nanotubes on the thermal properties of epoxy nanocomposites. Express Polymer Letters, **4**, 217–226 (2010). DOI: 10.3144/expresspolymlett.2010.28

[23] Jana S., Zhong W-H.: Curing characteristics of an epoxy resin in the presence of ball-milled graphite particles. Journal of Materials Science, **44**, 1987–1997 (2009). DOI: 10.1007/s10853-009-3293-2

[24] Guo B., Wan J., Lei Y., Jia D.: Curing behaviour of epoxy resin/graphite composites containing ionic liquid. Journal of Physics D: Applied Physics, **42**, 145307/1–145307/8 (2009).
DOI: 10.1088/0022-3727/42/14/145307

[25] Gerson A. L., Bruck H. A., Hopkins A. R., Segal K. N.: Curing effects of single-wall carbon nanotube reinforcement on mechanical properties of filled epoxy adhesives. Composites Part A: Applied Science and Manufacturing, **41**, 729–736 (2010).
DOI: 10.1016/j.compositesa.2010.02.002

[26] May C. A.: Epoxy resins, chemistry and technology. Marcel Dekker, New York (1988).

[27] Hummers W. S., Offeman R. E.: Preparation of graphitic oxide. Journal of the American Chemical Society, **80**, 1339 (1958).
DOI: 10.1021/ja01539a017

[28] Stankovich S., Dikin D. A., Piner R. D., Kohlhaas K. A., Kleinhammes A., Jia Y. Y., Wu Y., Nguyen S. T., Ruoff R. S.: Synthesis of graphene-based nanosheets via chemical reduction of exfoliated graphite oxide. Carbon, **45**, 1558–1565 (2007).
DOI: 10.1016/j.carbon.2007.02.034

[29] Paredes J. I., Villar-Rodil S., Martínez-Alonso A., Tascón J. M. D.: Graphene oxide dispersions in organic solvents. Langmuir, **24**, 10560–10564 (2008).
DOI: 10.1021/la801744a

[30] Du X., Yu Z-Z., Dasari A., Ma J., Mo M., Meng Y., Mai Y-W.: New method to prepare graphite nanocomposites. Chemistry of Materials, **20**, 2066–2068 (2008).
DOI: 10.1021/cm703285s

[31] Kim S. H., Woo I. L., Park J. M.: Assessment of dispersion in carbon nanotube reinforced composites using differential scanning calorimetry. Carbon, **47**, 2699–2703 (2009).
DOI: 10.1016/j.carbon.2009.05.026

[32] Xie H., Liu B., Yang H., Wang Z., Shen J., Cheng R. S.: Thermal characterization of carbon-nanofiber-reinforced tetraglycidyl-4,4′-diaminodiphenylmethane/4,4′-diaminodiphenylsulfone epoxy composites. Journal of Applied Polymer Science, **100**, 295–298 (2006).
DOI: 10.1002/app.23106

[33] Seyhan A. T., Sun Z., Deitzel J., Tanoglu M., Heider D.: Cure kinetics of vapor grown carbon nanofiber (VGCNF) modified epoxy resin suspensions and fracture toughness of their resulting nanocomposites. Materials Chemistry and Physics, **118**, 234–242 (2009).
DOI: 10.1016/j.matchemphys.2009.07.045

[34] Cai Z-Q., Movva S., Chiou N-R., Guerra D., Hioe Y., Castro J. M., Lee J. L.: Effect of polyaniline surface modification of carbon nanofibers on cure kinetics of epoxy resin. Journal of Applied Polymer Science, **118**, 2328–2335 (2010).
DOI: 10.1002/app.31656

[35] Rozenberg B. A.: Kinetics, thermodynamics and mechanism of reactions of epoxy oligomers with amines. Advances in Polymer Science, **75**, 113–165 (1986).
DOI: 10.1007/BFb0017916

[36] He H., Klinowski J., Forster M., Lerf A.: A new structural model for graphite oxide. Chemical Physics Letters, **287**, 53–56 (1998).
DOI: 10.1016/S0009-2614(98)00144-4

[37] Gao W., Alemany L. B., Ci L., Ajayan P. M.: New insights into the structure and reduction of graphite oxide. Nature Chemistry, **1**, 403–408 (2009).
DOI: 10.1038/nchem.281

[38] Gao J., Shen K., Gao Z. M.: The cure behavior of tetraglycidyl diaminodiphenyl methane with diaminodiphenyl sulfone. Thermochimica Acta, **352–353**, 153–158 (2000).
DOI: 10.1016/S0040-6031(99)00460-8

eXPRESS Polymer Letters Vol.5, No.9 (2011) 819–824
Available online at www.expresspolymlett.com
DOI: 10.3144/expresspolymlett.2011.80

Electric field assisted thermal annealing reorganization of graphene oxide/polystyrene latex films

S. Bittolo Bon[1], *L. Valentini*[1*], *J. M. Kenny*[1,2]

[1]Dipartimento di Ingegneria Civile e Ambientale, Università di Perugia, UdR INSTM, Strada di Pentima 4, 05100 Terni, Italy
[2]Institute of Polymer Science and Technology, CSIC, Juan de la Cierva 3, 28006 Madrid, Spain

Received 4 February 2011; accepted in revised form 25 March 2011

Abstract. Graphene/polymer films were prepared by casting water dispersion of graphene oxide (GO) in the presence of polystyrene (PS) latex particles. The samples were heated up to 180°C and exposed to an external electric voltage during their annealing. We observed that for the GO/PS films deposited before the electric field assisted thermal annealing the polymer latex was embedded in the graphene sheets, while the electric field assisted thermal annealing induces a phase separation with the enrichment of the PS phase above an underlying GO layer. For the films annealed under an external electric field we have also found that as the electric current passes through the GO film, GO could be recovered to reduced GO with decreased resistance.

Keywords: *nanocomposites, coatings, graphene oxide, electrical properties*

1. Introduction

Graphene, one-atom thick two-dimensional molecule made of sp^2 hybridized carbon atoms, is generally prepared by mechanical exfoliation [1], epitaxial growth [2] and chemical methods [3]. Among these methods the most common route toward large quantities of reduced graphene begins with the oxidation of graphite to graphene oxide (GO).

The oxidation of graphite to GO breaks the sp^2 hybridized structure generating defects that increase the distance between adjacent sheets from 0.335 nm in graphite to 0.68 nm for GO powder [4]. This increased spacing reduces interaction between sheets, thus facilitating the delamination of GO into single layer graphene oxide sheets upon exposure to water in a sonication bath. The main disadvantage of this material is that the charge carrier transport (i. e. electrons) observed in nearly ideal graphene are absent in GO, but at the same time the easy processing and the versatile properties of GO make the reduction methods for such material attractive for fundamental research as well as for applications [5].

To date, most work in the area of graphene based polymer nanocomposites has focused on property modification using small amounts of graphene [6]. This emphasis can be partially attributed to the intrinsic properties of the graphene (high mechanical properties, high thermal conductivity, high electrical conductivity, etc.), which result in remarkable property improvements at low graphene concentrations. Notably, nanocomposites with randomly oriented graphene sheets, commonly exhibit isotropic properties.

Among the strategies to disperse graphene onto polymer matrix (i. e. solvent processing, in situ polymerisation and melt processing), latex technology represents a novel method for manufacturing polymer/graphene nanocomposites [7–9].

While composites prepared from aqueous graphene dispersions mixed with polystyrene latex and sub-

*Corresponding author, e-mail: mic@unipg.it

sequent compression molding was accomplished with an increase of the electrical conductivity of several order of magnitude [8] there is no literature so far on the morphological and physical properties of graphene oxide/polystyrene latex films deposited under an electric field assisted thermal annealing treatment.

Here we report on the deposition of graphene oxide/polystyrene composite films by electric field assisted thermal annealing method. It was found that the thermal annealing induces a self-organization of the GO sheets with respect to the polymeric phase and that the application of an external electric field during the thermal treatment leads to the reduction of the GO sheets decreasing their surface resistivity.

2. Experimental part

Graphene oxide (GO) were purchased from Cheaptubes (single layer GO, Cheaptubes, Brattleboro – VT, USA; thickness 0.7–1.2 nm by AFM see Figure 1a). Distillated water dispersion (1 mg/1 ml) was prepared and sonicated (CV33, Bioblock Scientific, Madrid, Spain, 750 W, 60% amplitude) for 1 hr to yield a yellow suspension. GO/polymer samples were prepared by adding 1:1 volume ratio of water polystyrene latex particles dispersion (PS latex S130-1, Agar Scientific, Stansted, England, 10 wt% dispersion in water with surface-bound sulfate groups as stabilizer, average particle diameter 125 nm). Glass slides (2 cm × 2 cm) were used as substrates. The glass surface was first cleaned by the ethanol and then cleansed sequentially with deionized water and finally dried in high purity nitrogen. The glass surface was plasma treated in oxygen atmosphere (10 min., 10 Pa, with the substrate polarized with a radiofrequency plasma enhanced chemical vapour deposition system (PECVD 100, Kenosystec, Milan, Italy) at –300 V to improve its wettability and modified by a thin layer of GO/PS solution which were drop-cast on the plasma treated substrate. After the evaporation of the water a top metal electrodes, which were made up of Al and spaced 1mm, were deposited on the dried composite film by vacuum evaporation (≈$133 \cdot 10^{-4}$ Pa) with an optimized thickness of 60 nm. The samples were heated up to 180°C (heating rate 10°C/min) and exposed for 10 min to a DC electric voltage of 20 V applied between the aluminium electrodes. The samples were then cooled down to room temperature leaving the electric field applied. A similar procedure was then repeated by applying the electric field to the samples at 50°C. The morphology of the prepared samples was characterized by field emission scanning electron microscopy (FESEM) (Supra 25, Carl Zeiss, Oberkochen, Germany). The surface resistance has been measured with four-point probes (4200 SCS, Keithley Instruments, Cleveland-Ohio, USA). GO/PS latex casted films were characterized with UV-Vis measurements (Lambda 35, Perkin-Elmer, San Jose-California, USA); for all samples, a quartz slide was used as the reference. The Fourier transformed infrared spectra (FTIR) (Jasco 615, Jasco Analytical Instruments, Easton-MD, USA) of the deposited film were recorded in transmission mode between 250 and 2500 cm^{-1}. Contact angles were measured with an optical contact angle meter at ambient temperature. Water droplets were dropped carefully onto the surfaces and the contact angle was monitored as a function of time. Raman spectroscopy was carried out using a LabRam (HORIBA Jobin Yvon SRL, Opera Milano, Italy) Raman spectrometer. The laser excitation of the He–Ne laser was 633 nm and the power was kept at 2 mW. The spot size of the laser was about 1–2 μm.

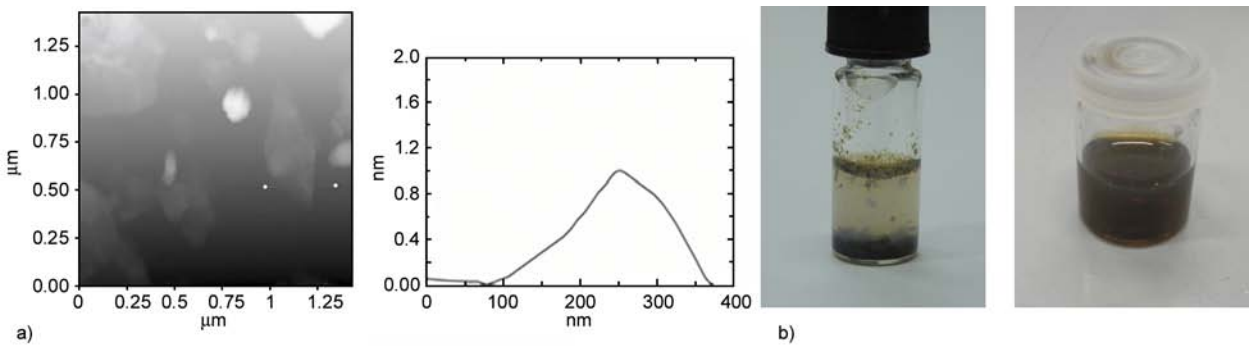

Figure 1. a) AFM image (left panel) and AFM height profile (right panel) of GO flakes. b) Vials containing GO/PS latex dispersion before (left panel) and after sonication (right panel), respectively.

3. Results and discussion

Figure 1b shows the water solution of the vial with before its sonication; it contains visible precipitates while the dark brown dispersion of GO dispersed in PS latex particles contains no visible precipitates after its sonication.

The morphology of neat PS latex and GO/PS latex films, formed after the evaporation of water at 50°C, were imaged by means of FESEM and reported in Figure 2a–b, respectively. It is evident that the polymer latex is embedded in the graphene sheets (Figure 2b). It should be noted that the graphene sheets, in spite of their ultrathin thickness, have very high aspect ratio and are considerably larger with respect to the spherical PS latex particles. It should be noted that the application of an external electric field during the evaporation of water at 50°C did not cause any effect onto the film morphology.

The electric field assisted thermal annealing at 180°C induces a change in the film morphology (Figures 2c) inducing the formation of separated phases as suggested by the cross-section SEM image in Figure 2d and schematized in Figure 2e.

This phenomenon was monitored by contact angle measurements. The contact angle measurements of the GO/PS latex blend evaporated at 50°C with and without electric field show an increase of the wettability with respect to the PS latex samples processed in the same way, this effect being due to the presence of carboxylic functionalities on the GO sheets position at the film/air interface (Table 1). On the contrary the hydrophobic contact angle value measured for electric field assisted thermal annealed GO/PS latex blend at 180°C is similar to that observed for neat PS latex processed with the same conditions (Table 1). This phenomenon could be explained with the enrichment of the polymer phase

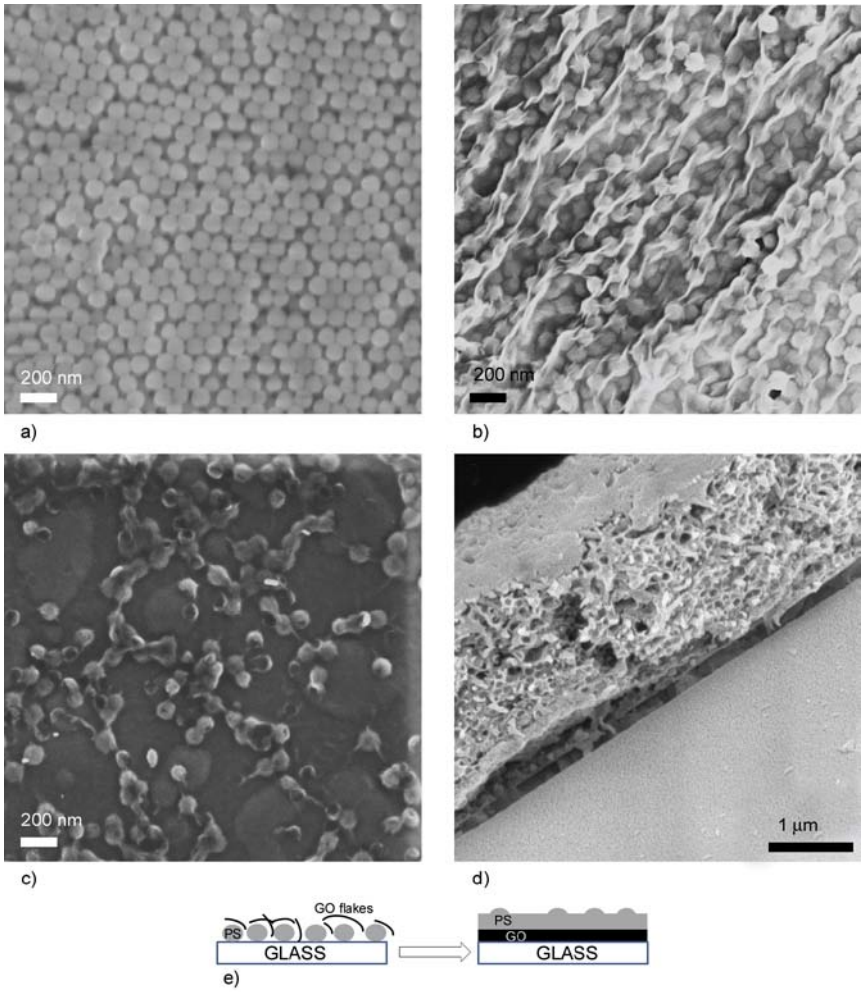

Figure 2. a) FESEM image of neat PS latex film. FESEM images of GO/PS latex film cast at b) 50°C and c) under the application of an external bias of 20 V for 10 min. at 180°C. d) Cross section FESEM image of GO/PS latex film cast at 1800°C under the application of an external bias of 20 V for 10 min. e) Scheme of GO/PS latex film formation before (left) and after (right) electric field assisted thermal annealing, respectively.

Table 1. Contact angle and surface resistivity (R_s) values for the prepared samples at 50°C, 50°C under electric field, 180°C and 180°C under electric field, respectively

Sample	Sample preparation conditions	Contact angle [°]	R_s[a] [Ω/cm^2]
PS latex	50°C	60	$0.2 \cdot 10^9$
PS latex	50°C under electric field	76	–[b]
PS latex	180°C	60	$0.3 \cdot 10^9$
PS latex	180°C under electric field	79	$0.4 \cdot 10^9$
GO/PS latex	50°C	36	$0.1 \cdot 10^9$
GO/PS latex	50°C under electric field	40	$3.7 \cdot 10^8$
GO/PS latex	180°C	70	$0.3 \cdot 10^9$
GO/PS latex	180°C under electric field	78	$9.0 \cdot 10^6$

[a]Four-probe measurements of surface resistance
[b]Surface resistance larger than 10^{11} Ω/cm^2

onto the GO sheets as shown in Figure 2d and proposed in Figure 2e where the thermal annealing induces the formation of PS hydrophobic domains that repel the water at the film/liquid interface.

Along with the thermal annealing effect, it should be noted that only for the GO/PS latex samples treated with the presence of an external electric field, a decrease of the surface resistance was observed (Table 1) being this effect more pronounced for the thermal annealed samples at 180°C.

The high resistance of GO/PS latex films is due to the existence of oxygen-containing groups, which could introduce defects to graphene [5]. It is well known how the deoxygenation could recover the GO conductivity to some extent. For example it has been shown that deoxygenation occurs in GO when it is heated above 200°C resulting in a thermal reduction [10, 11]. In our case the annealing in absence of an external electric field did not produce any significant change on the surface resistivity of our samples. On the contrary the electric field assisted thermal annealing of GO/PS latex film induces a marked decrease of the film surface resistivity. Recently, it has been reported that Joule heat will be generated when applying a large current through a graphene materials-based device [12, 13]. This makes it possible that the reduction of our GO is due to Joule heating.

The chemical changes occurring upon applying an external electric field to our GO sheets can be observed by FTIR spectroscopy in Figure 3. The most characteristic features in the FTIR spectrum of GO are the adsorption bands corresponding to the C=O carbonyl stretching at 1733 cm^{-1} and the O–H

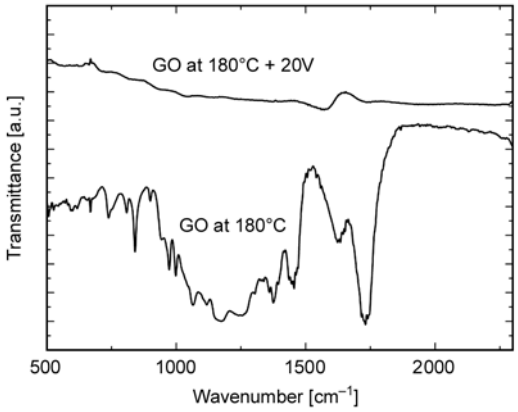

Figure 3. FTIR spectra of GO annealed at 180°C and annealed at 180°C and exposed to an external electric field, respectively

deformation vibration at 1412 cm^{-1} [14, 15]. A broad and intense signal at 1621 cm^{-1} can be assigned to the vibrations of the adsorbed water molecules, but may also contain components from vibrations of un-oxidized graphitic domains. Upon plasma treatment, the C=O stretching vibration at 1733 cm^{-1} and the O–H deformation vibration at 1412 cm^{-1} of the GOP is gradually attenuated.

As demonstrated by the values reported in Table 1 and by the graph of the electric current vs. time recorded on our samples (Figure 4), it is interesting to note that only the application of the electric field during the thermal annealing displays a distinct decrease of the sheet resistance with an increase of the current passing through the film. The electric current decreases with time when we apply the electric field at 50°C. The current signal recorded at the start of the experiment is due to the presence of water that evaporates during the experiment leading to an insulating hybrid interface made of PS latex

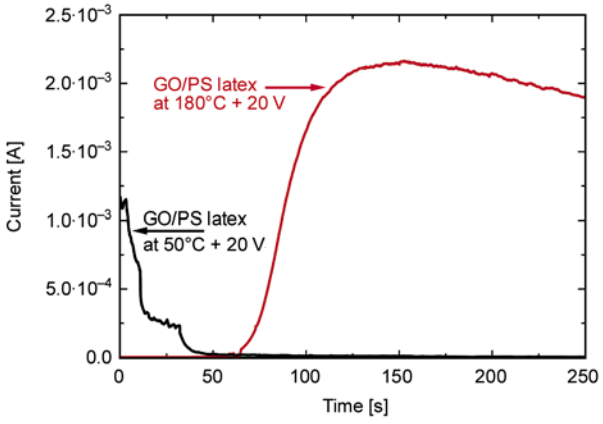

Figure 4. Current vs. time curves of GO/PS latex films under the application of an external bias of 20 V for 10 min. at 50°C and at 180°C, respectively

and GO sheets as reported in Figure 2b. On the contrary the electric current increases when the electric field was applied at 180°C, in this case the medium for the electric current flow is not the water that evaporates instantaneously but leads to the formation of a conductive pathway for the electron flux. The only one component of the hybrid composite able to be conductive is the reduced GO component that has to segregate in a conductive pathway to avoid interruption of the electron charge carrier flow by the presence of intercalated insulating PS latex particles. Accordingly to Figure 2d and Figure 3 this finding suggests that: (i) the thermal annealing segregates the GO between the substrate/polymer interface leading to (ii) a percolation pathway for the electric current induced reduction of the GO film.

The optical absorption in the whole UV-Vis spectral region has been investigated for the GO/PS latex samples (see the supporting information for the UV-Vis spectra of the PS latex samples), as shown in Figure 5. The increase in the absorption for the annealed sample at 180°C is due to the GO sheet aggregation between the substrate/polymer interface; the further decrease of the optical transparency for the electric field assisted thermal annealed sample indicates deoxygenation of GO. The observed increase of the absorption suggests that the flow of the electric current through the GO layer reduces the degree of deoxygenation of GO restoring the degree of aromaticity in the graphene plane [5]. The structural model presented by Eda *et al.* [5] illustrated that the reduction restores sp^2 carbon in GO sheet plane; this reduction leads to a greater connectivity among the original sp^2 domains increasing the optical absorbance and leaving the graphene layer thickness unaltered.

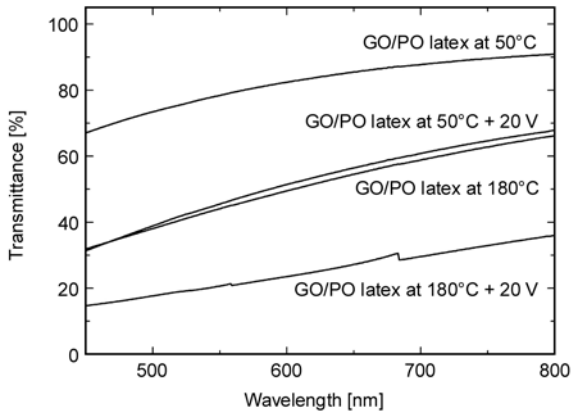

Figure 5. UV-Vis spectra of the prepared samples before and after electric field assisted water evaporation at 50°C and before and after electric field assisted thermal annealing at 180°C, respectively

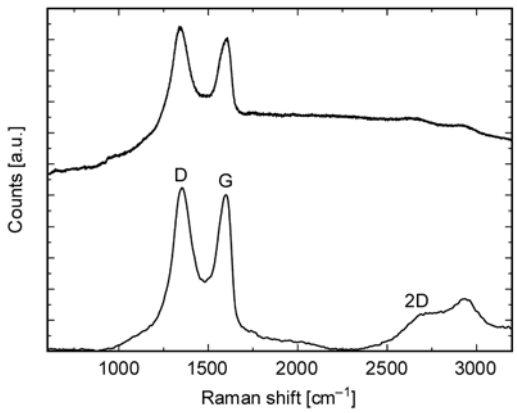

Figure 6. Raman spectra of GO/PS latex film thermal annealed at 180°C without the external electric field (top) and GO/PS latex film thermal annealed at 180°C with the external electric field (bottom), respectively

In order to prove these argumentations Raman analysis was used to provide further insight into the structural changes of the graphene oxide flakes, as shown in Figure 6 [16]. The attenuation of the second-order zone boundary phonon (2D) peak at 2646 cm^{-1} together with a shoulder peak at ~2920 cm^{-1} observed for the GO/PS latex film annealed at 180°C without the external electric field was due to the presence of residual oxygen functional groups [17].

The first-order spectrum of the prepared samples is also characterized by a strong band at ~1590 cm^{-1} (G band) and a band at ~1340 cm^{-1} (D band). From the Raman spectra it is also possible to see that the full width at half maximum of the D band decreases for the GO/PS latex film when it underwent to electric field assisted thermal annealing; specifically, this value varies from 186 cm^{-1} for the GO/PS sample annealed at 180°C without electric field to 149 cm^{-1} after the electric field assisted thermal annealing at 180°C. Accordingly to Yang *et al.* [18] we attribute these findings to the removal of oxygen from the GO sheet.

4. Conclusions

In summary, the graphene oxide/polystyrene composite films have been fabricated by electric field assisted thermal annealing method. It has been reported how the GO sheets can be transported

between the substrate/polymer interface by thermal annealing; the combination of the thermal treatment with the application of an electric current lead to the reduction of the GO sheets decreasing their surface resistivity. Therefore, self organization of this 2D material within a polymer matrix could lead to many exciting functional graphene-based polymer nanocomposites.

Acknowledgements

The work was supported by the Italian Ministry of University and Research thorough the PRIN 2008 project (Grant No. 20089B75ML_001). We are grateful for this support.

References

[1] Novoselov K. S., Geim A. K., Morozov S. V., Jiang D., Zhang Y., Dubonos S. V., Grigorieva I. V., Firsov A. A.: Electric field effect in atomically thin carbon films. Science, **306**, 666–669 (2004).
DOI: 10.1126/science.1102896

[2] Berger C., Song Z., Li X., Wu X., Brown N., Naud C., Mayou D., Li T., Hass J., Marchenkov A. N., Conrad E. H., First P. N., de Heer W. A.: Electronic confinement and coherence in patterned epitaxial graphene. Science, **312**, 1191–1196 (2006).
DOI: 10.1126/science.1125925

[3] Park S., Ruoff R. S.: Chemical methods for the production of graphenes. Nature Nanotechnology, **4**, 217–224 (2009).
DOI: 10.1038/NNANO.2009.58

[4] Bourlinos A. B., Gournis D., Petridis D., Szabó T., Szeri A., Dékány I.: Graphite oxide: Chemical reduction to graphite and surface modification with primary aliphatic amines and amino acids. Langmuir, **19**, 6050–6055 (2003).
DOI: 10.1021/la026525h

[5] Eda G., Chhowalla M.: Chemically derived graphene oxide: Towards large-area thin-film electronics and optoelectronics. Advanced Materials, **22**, 2392–2415 (2010).
DOI: 10.1002/adma.200903689

[6] Stankovich S., Dikin D. A., Dommett G. H. B., Kohlhaas K. M., Zimney E. J., Stach E. A., Piner R. D., Nguyen S. T., Ruoff R. S.: Graphene-based composite materials. Nature, **442**, 282–286 (2006).
DOI: 10.1038/nature04969

[7] Sun S., Cao Y., Feng J., Wu P.: Click chemistry as a route for the immobilization of well-defined polystyrene onto graphene sheets. Journal of Materials Chemistry, **20**, 5605–5607 (2010).
DOI: 10.1039/c0jm01269f

[8] Tkalya E., Ghislandi M., Alekseev A., Koning C., Loos J.: Latex-based concept for the preparation of graphene-based polymer nanocomposites. Journal of Materials Chemistry, **20**, 3035–3039 (2010).
DOI: 10.1039/b922604d

[9] Wissert R., Steurer P., Schopp S., Thomann R., Mülhaupt R.: Graphene nanocomposites prepared from blends of polymer latex with chemically reduced graphite oxide dispersions. Macromolecular Materials and Engineering, **295**, 1107–1115 (2010).
DOI: 10.1002/mame.201000263

[10] Wang X., Zhi L., Müllen K.: Transparent, conductive graphene electrodes for dye-sensitized solar cells. Nano Letters, **8**, 323–327 (2008).
DOI: 10.1021/nl072838r

[11] Becerril H. A., Mao J., Liu Z., Stoltenberg R. M., Bao Z., Chen Y.: Evaluation of solution-processed reduced graphene oxide films as transparent conductors. ACS Nano, **2**, 463–470 (2008).
DOI: 10.1021/nn700375n

[12] Jung I., Dikin D. A., Piner R. D., Ruoff R. S.: Tunable electrical conductivity of individual graphene oxide sheets reduced at 'low' temperatures. Nano Letters, **8**, 4283–4287 (2008).
DOI: 10.1021/nl8019938

[13] Yao P., Chen P., Jiang L., Zhao H., Zhu H., Zhou D., Hu W., Han B-H., Liu M.: Electric current induced reduction of graphene oxide and its application as gap electrodes in organic photoswitching devices. Advanced Materials, **22**, 5008–5012 (2010).
DOI: 10.1002/adma.201002312

[14] Szabó T., Berkesi O., Dékány I.: DRIFT study of deuterium-exchanged graphite oxide. Carbon, **43**, 3186–3189 (2005).
DOI: 10.1016/j.carbon.2005.07.013

[15] Hontoria-Lucas C., López-Peinado A. J., López-Gonzalez J. de D., Rojas-Cervantes M. L., Martín-Aranda R. M.: Study of oxygen-containing groups in a series of graphite oxides: Physical and chemical characterization. Carbon, **33**, 1585–1592 (1995).
DOI: 10.1016/0008-6223(95)00120-3

[16] Ferrari A. C.: Raman spectroscopy of graphene and graphite: Disorder, electron–phonon coupling, doping and nonadiabatic effects. Solid State Communications, **143**, 47–57 (2007).
DOI: 10.1016/j.ssc.2007.03.052

[17] Lazzeri M., Mauri F.: Nonadiabatic Kohn anomaly in a doped graphene monolayer. Physycal Review Letters, **97**, 266407/1–266407/4 (2006).
DOI: 10.1103/PhysRevLett.97.266407

[18] Yang D., Velamakanni A., Bozoklu G., Park S., Stoller M., Piner R. D., Stankovich S., Jung I., Field D. A., Ventrice Jr. C. A., Ruoff R. S.: Chemical analysis of graphene oxide films after heat and chemical treatments by X-ray photoelectron and Micro-Raman spectroscopy. Carbon, **47**, 145–152 (2009).
DOI: 10.1016/j.carbon.2008.09.045

eXPRESS Polymer Letters Vol.5, No.9 (2011) 825–837
Available online at www.expresspolymlett.com
DOI: 10.3144/expresspolymlett.2011.81

Sonochemical-assisted fabrication of biologically active chiral poly(ester-imide)/TiO_2 bionanocomposites derived from L-methionine and L-tyrosine amino acids

S. Mallakpour[1,2*], *F. Zeraatpisheh*[1], *M. R. Sabzalian*[3]

[1]Organic Polymer Chemistry Research Laboratory, Department of Chemistry, Isfahan University of Technology, Isfahan, 84156-83111, I. R. Iran
[2]Nanotechnology and Advanced Materials Institute, Isfahan University of Technology, Isfahan, 84156-83111, I. R. Iran
[3]College of Agriculture, Department of Agronomy and Plant Breeding, Isfahan University of Technology, Isfahan, 84156-83111, I. R. Iran

Received 30 December 2010; accepted in revised form 28 March 2011

Abstract. A new chiral poly(ester-imide) (PEI) was prepared via direct polyesterification of *N,N′*-(pyromellitoyl)-bis-(L-tyrosine dimethyl ester) and *N*-trimellitylimido-L-methionine using tosyl chloride/pyridine/*N,N′*-dimethylformamide system as a condensing agent. The resulting new chiral polymer was obtained in good yield and had good thermal stability as well as good solubility in common organic solvents. After that, PEI/titanium bionanocomposites (PEI/TiO_2 BNCs) were prepared using the modified nanosized TiO_2 via sonochemical reaction that can accelerate hydrolysis, increase collision chance for the reactive system and improve the dispersion of the nanoparticles in polymer matrix. The scanning electron microscopy (SEM), field emission scanning electron microscopy (FE-SEM) and transmission electron microscopy (TEM) results indicated that there is no aggregation of a large quantity of particles. Thermogravimetric analysis (TGA) confirmed that the heat stability of the BNC polymers in the temperature range of 400–800ºC was enhanced by addition of TiO_2 nanoparticles. Furthermore, in vitro toxicity test was employed for assessing the sensitivity of these compounds to microbial degradation. To this purpose, polymer and PEI/TiO_2 BNCs were investigated under soil burial conditions. The results of this study revealed that polymer and its BNCs are biologically active and non-toxic in the natural environment although some antimicrobial properties were found for BNCs.

Keywords: *biocomposites, non-toxic, TiO_2 nanoparticles, thermally stable poly(ester-imide), ultrasonic irradiation*

1. Introduction

The last decade has seen the improvement of an alternative chemistry, which intends to decrease the human impact on the environment. The biopolymers are noticeably involved in this tendency. However, even if much commercial merchandise is attainable, their current properties (mechanical properties and moisture sensitivity) have to be improved to be truly competitive with the petroleum-based products [1]. One of the most promising responses to conquer these weaknesses is designing bionanocomposites (BNC)s consisting of a biopolymer matrix reinforced with nanoparticles having at least one dimension in the nanometer range (1–100 nm) [2]. These hybrid materials combine the advantages of the organic biopolymers (light weight, flexibility, good impact resistance, good processability and biodegradability) and inorganic nanofiller materials (good chemical resistance, high thermal stability, and high brittleness). Thus they create several industrial applications [3–5]. For producing suitable BNCs, it is necessary to

*Corresponding author, e-mail: mallak@cc.iut.ac.ir

disperse the inorganic materials such as nanoparticles in organic matrices. A homogeneous dispersion of the nanoparticles is believed to contribute better to the property enhancement. However, nanoparticles aggregate easily and difficult to disperse them in a solvent or polymer matrix because of their high specific surface area and surface energy. Some technical routes, such as encapsulating polymerization [6], solution intercalation [7], latex precompounding [8], ultrasonic irradiation [9] and the use of different coupling agents [10] were developed for enhancing the dispersion state of nanoparticles in polymer matrix. However, the sonochemical method has been reported to be faster than aforementioned techniques. The main advantage in sonochemical experiments is that it is rather inexpensive. Sonochemistry, the chemical effects of high intensity ultrasound, is a topic of resurging interest for its biological, synthetic and catalytic relevance. Ultrasonic irradiation arisen from acoustic cavitation can produce hot spots with transient temperatures of about 5000 K, and local pressure as high as 500 atm in a very rigorous environment. Hence, the utilization of ultrasound to improve the rate of reaction has become a routine method in scattering, crushing, and activation of particles, as well as initiation of polymerization [9, 11–14].

Among many inorganic nanoparticles, nanosized titanium dioxide (TiO_2) is one of the most encouraging inert, nontoxic, and cheap materials in research because of its versatile functions such as antifouling, antimicrobial, deodorizing and photovoltaic effects [15]. Therefore, it has a widespread range of applications, e.g. in filters, lenses, reflectors, optical adhesives and antireflection films [16–18], optical waveguides [19], photochemical solar cells [20], and TiO_2-based photocatalytic detoxification of air and water for environmental remediation [21–24].

Owing to the escalating performance characteristics demanded on polymers in various fields, use of poly(ester-imide)s (PEI)s because of favorable properties, such as good heat resistance, mechanical strength, electrical insulation and other physical properties are growing steadily. As a matter of fact, PEI is the combination of polyimide and polyester which could have properties of both of them and provides good balance between thermal stability and processability [25–26]. Among the PEIs, chiral ones are important polymers in macromolecular science. In general, the synthesis of optically active synthetic polymers is a subject of special interest because of their applications to chromatographic supports, catalysts and materials with ferroelectric and nonlinear optical properties. The optical activity of the polymer can be tuned by choosing a suitable chiral initiator or by starting from a chiral monomer [27].

In this work, a novel PEI containing L-methionine and L-tyrosine amino acids in the main chain was prepared via direct polycondensation reaction. Then, optically active PEI/TiO_2 BNCs were synthesized through a simple and convenient ultrasonic wave dispersion process of modified nanoparticle with coupling agent. The resulting BNC polymers are characterized by several techniques including Fourier transform infrared spectroscopy (FT-IR), powder X-ray diffraction (XRD), thermogravimetric analysis (TGA) and their morphology were investigated by field emission scanning electron microscopy (FE-SEM), scanning electron microscopy (SEM) and transmission electron microscopy (TEM) analysis.

2. Experimental

2.1. Materials

All chemicals were purchase from Fluka Chemical Co. (Buchs, Switzerland), Aldrich Chemical Co. (Milwaukee, WI), Riedel-deHaen AG (Seelze, Germany) and Merck Chemical Co. *N,N*′-Dimethyformamide (DMF) and pyridine (Py) were dried over barium oxide (BaO) and then were distilled under reduced pressure. The coupling agent (3-aminopropyltriethoxysilane) (KH550), was obtained from Merck Chemical Co. Nanosized TiO_2 powder which contain mostly anatase form with small percentage of rutile form was purchased from Nanosabz Co. with average particle sizes of 30–50 nm. The amino acids were used as obtained without further purification.

2.2. Characterization

Infrared spectra of the samples were recorded at room temperature in the range of 4000–400 cm^{-1}, on (Jasco-680, Japan) spectrophotometer. The spectra of solids were obtained using KBr pellets. The vibrational transition frequencies are reported in wave numbers [cm^{-1}]. Band intensities are assigned as weak (w), medium (m), strong (s) and broad (br).

Proton nuclear magnetic resonance (^{1}H-NMR spectra, 500 MHz) were recorded in *N,N′*-dimethylsulfoxide (DMSO)-d_6 solution using a Bruker (Germany) Avance 500 instrument. Multiplicities of proton resonance were designated as singlet (s) and multiplet (m). Inherent viscosity was measured by a standard procedure with a Cannon-Fenske (Mainz, Germany) routine viscometer. Specific rotation was measured with a Jasco (Osaka, Japan) P-1030 polarimeter at the concentration of 0.5 g/dl at 25ºC. TGA data were taken on STA503 WinTA instrument in a nitrogen atmosphere at a heating rate of 10ºC/min. Elemental analyses were performed by Leco, CHNS-932. The XRD patterns of the polymer and BNC polymers were recorded by employing a Philips X'PERT MPD diffractometer with a copper target at 40 kV and 30 mA and Cu K_α radiation: $\lambda = 1.54$ Å in the range 10–80º at the speed of 0.05º/min. To clarify the nanoscale structure, TEM (CM 120, Philips) was also used, at an accelerating voltage of 100 kV. For TEM, BNCs were suspended in water and a small drop of suspension was deposited on the carbon coated copper grid. SEM measurements of polymer and BNC polymers were carried out on a Philips XLC with backscattered electron detector at voltage of 20 kV. Small pieces of samples were mounted onto stubs using adhesive tapes and sputtered with a gold layer. Surface morphology and sample homogeneity of BNC polymers were characterized using FE-SEM (JSM-6700F, Japan).

2.3. Apparatus

The reaction was occurred on a MISONIX ultrasonic liquid processor, XL-2000 SERIES. Ultrasonic irradiation was carried out with the probe of the ultrasonic horn immersed directly in the mixture solution system with frequency of $2.25 \cdot 10^4$ Hz and 100 W powers.

2.4. Monomer synthesis

N-Trimellitylimido-L-methionine 1 as a diacid and *N,N′*-(pyromellitoyl)-bis-L-tyrosine dimethyl ester 2 as a diphenolic monomer were prepared according to our previous works [28, 29].

2.5. Polymer synthesis

The PEI was prepared by the following procedure and is shown in Figure 1. A solution of Py (0.20 ml) with tosyl chloride (TsCl) (0.29 g; $1.55 \cdot 10^{-3}$ mol) after 30 min stirring at room temperature, was treated with DMF (0.09 ml; $1.22 \cdot 10^{-3}$ mol) for 30 min and the mixture was added dropwise to a solution of diacid (2) (0.10 g; $3.09 \cdot 10^{-4}$ mol) in Py (0.20 ml). The mixture was maintained at room temperature for 30 min and then diol (1) (0.18 g; $3.09 \cdot 10^{-4}$ mol) was added to this mixture and the whole solution was stirred at room temperature for

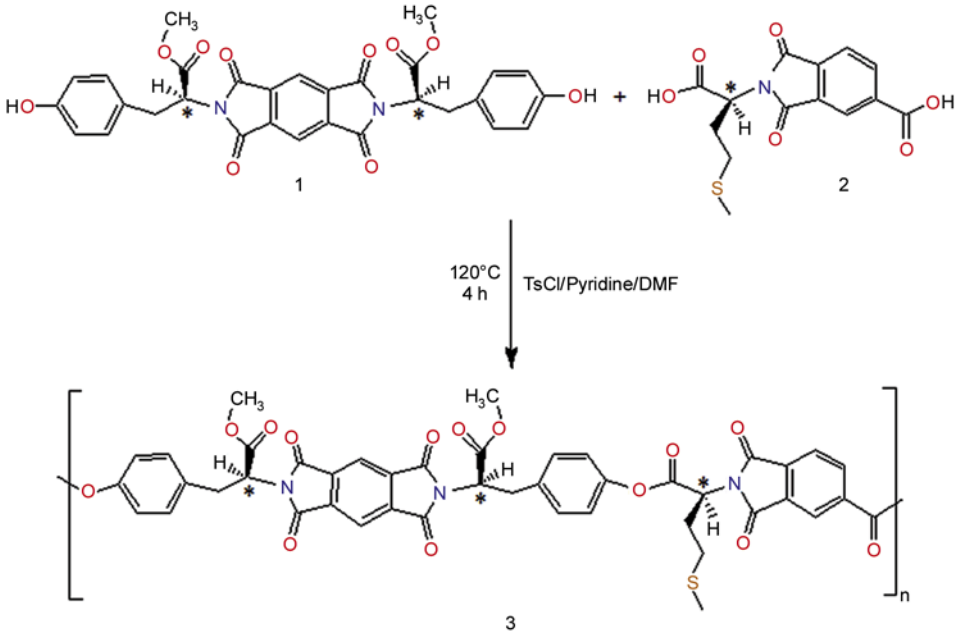

Figure 1. Synthesis of the PEI [3]

30 min and then at 120ºC for 4 h. As the reaction proceeded, the solution became viscous and then the viscous liquid was precipitated in 30 ml of methanol to give 0.24 g pale brown powder PEI (93% yield) and the specific rotation was measured ($[\alpha]_D^{25} = +18$).

FT-IR Peaks (KBr, cm^{-1}): 3433 (w, br), 3035 (w), 3070 (w), 2921 (m), 2852 (w), 1777 (s), 1722 (s), 1508 (m), 1382 (s), 1279 (w), 1245 (m), 1196 (m), 1169 (m), 1112 (w), 1099 (w), 727 (m).

^{1}H-NMR (500 MHz, DMSO-d_6, δ, ppm): 1.96 (s, 3H), 2.28–2.36 (m, 2H), 2.58–2.63 (m, 2H), 3.00–3.54 (m, 4H), 3.67 (s, 6H), 5.31 (m, 4H), 6.85 (s, 2H, Ar–H), 7.09-7.17 (m, 4H, Ar–H), 7.26 (s, 2H, Ar–H), 8.02 (s, 1H, Ar–H) 8.13–8.23 (m, 2H, Ar–H), 8.33(s, 1H, Ar–H), 8.42 (s, 1H, Ar–H).

Elemental analysis: calcd. for ($C_{44}H_{33}N_3O_{14}S$): C, 61.32%; H, 4.09%; N, 4.88%; S, 3.72%. Found: C, 60.20%; H, 4.27%; N, 5.11%; S, 3.96%.

2.6. Preparation of PEI/TiO_2 BNCs through ultrasonic irradiation

TiO_2 nanoparticles were chemically modified using ultrasonic reaction to obtain the KH550-capping TiO_2 particles. Typically, TiO_2 nanoparticles (0.30 g) were added into acetone (10 ml), and 10% weight percentage of KH550 was dissolved in H_2O (10 ml). The mixture was then exposed to high-intensity ultrasound irradiation for 30 min. After that it was centrifuged and dried. PEI was dispersed in 20 ml of absolute ethanol. A uniform colloidal dispersion was obtained after ultrasonication for 15 min at room temperature. The suspension was mixed with the appropriate amount of TiO_2-KH550 powder to produce 5, 10, 15, 20 and 25% W/W based on the PEI content followed by irradiation with high-intensity ultrasonic wave for 4 h at room temperature [30, 31]. After irradiation, the resulting suspension was centrifuged, and the precipitate was washed twice

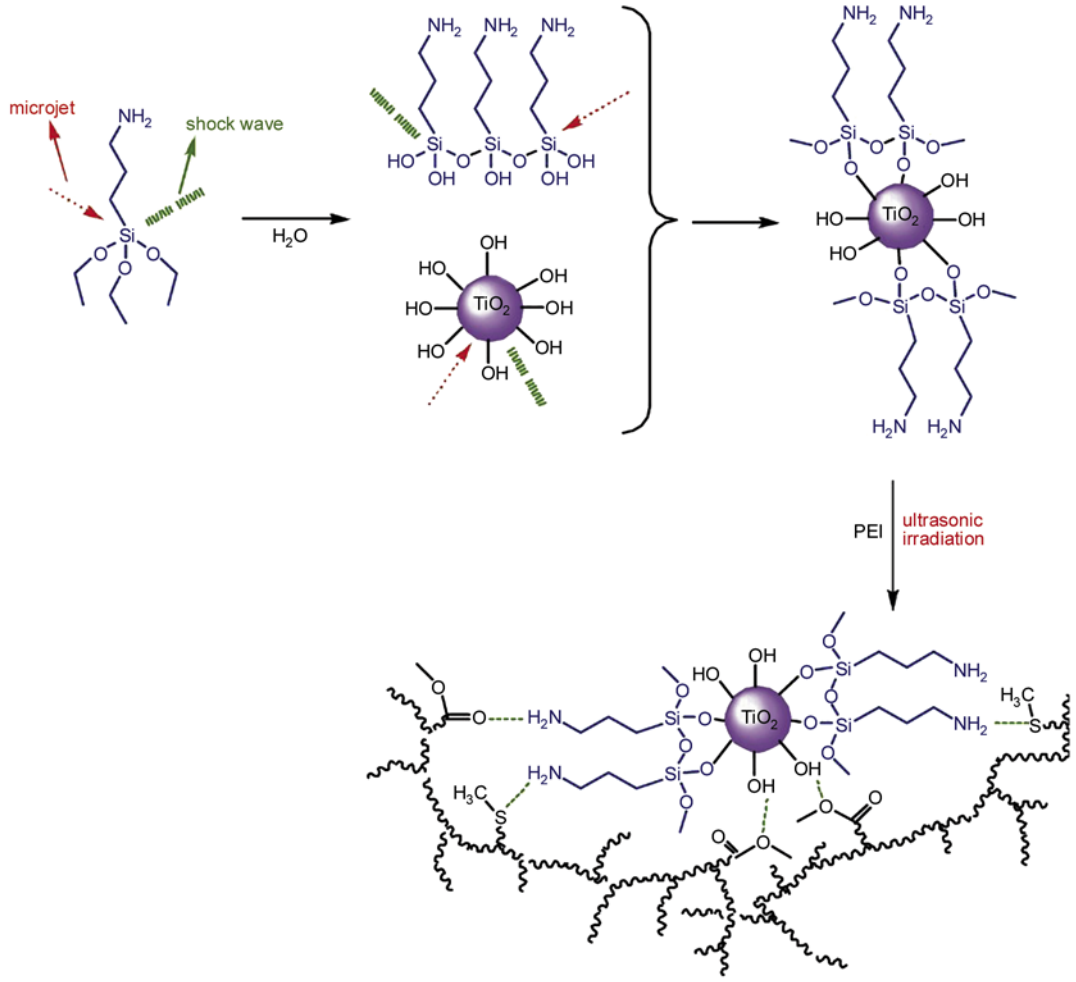

Figure 2. Preparation of PEI/TiO_2 BNCs

with absolute ethanol. The solid was dried in vacuum at room temperature for 8 h and the obtained product was kept for further characterization. The process is described in Figure 2.

2.7. Soil burial test of PEI/TiO_2 BNCs

The bioactivity of the PEI/TiO_2 BNCs was checked during natural soil burial for 3 months. Thirty-mg specimens of diacid, and obtained polymers of PEI and PEI/TiO_2 BNC (10 wt%) were buried in the soil by mixing with 1.5 g clay-loam soil in 1.5 ml plastic vials. Samples were incubated at almost constant temperature of 28°C for three months. The moisture content was maintained at 60–70% of the soil maximum water holding capacity. Also, the vials were capped to avoid water evaporation from the soil surface. After 90 days, the buried specimens were dug out, immersed in distilled water and water extracts of samples were inoculated on Potato Dextrose Agar (PDA) medium by streak culture and soil microbial population as the number of bacterial and fungal colony forming units (CFUs) per 100 µl of water extract was counted. Soil free of any compound and BPA-containing soil were used as negative and positive control, respectively, for comparison.

2.8. Effect of PEI/TiO_2 BNCs on growth of wheat seedlings

Plastic vials with capacity of 1.5 ml were used, each receiving 30 mg of each compound including diacid, obtained polymer and PEI/TiO_2 BNC (10 wt%) in three replications. Vials were incubated at 23–25°C, with a saturated humidity at dark for 3 months. After this period, wheat seeds were pre-germinated on distilled water humidified germination paper, during a period of five days in a germination chamber under controlled conditions (temperature of 25ºC and photoperiod light and dark of 14/10 h). Then, an individual germinated wheat seed was put on the soil in the center of each vial so that rootlet was in contact with soil. Seedlings were grown in a glass box with 80% humidity and observations were made on seedling growth. Plants were harvested 20 days after transplanting. Shoot length was measured using a ruler, and then seedlings were dried at 65ºC for 48 h for total dry matter measurement.

3. Results and discussion

3.1. Polymer synthesis

PEI was synthesized by the direct polycondensation reaction of an equimolar mixture of diol 1 with diacid 2 in a system of TsCl/Py/DMF as condensing agent (Figure 1). For the polycondensation of aromatic diacid and aromatic diol, a vilsmeier adduct was prepared by dissolving TsCl in a mixed solvent of Py and DMF. Polyesterifacation of diacid with aromatic diol was carried by varying the aging time of the initial reaction of TsCl and Py. TsCl was dissolved in Py at room temperature and kept at this temperature for 30 min according to previously reported procedures that the suitable aging time is 30 min [32]. It was determined that a molar ratio of diacid over TsCl equal to 5 and the reaction time of 4 h are required to produce a polymer with better yield and inherent viscosity. Further addition of TsCl did not improve the inherent viscosity of polymer and also caused the diminution of yield. The reaction was also run at 120°C as proposed by Higashi *et al.* [33]. The inherent viscosity of the resulting polymer under optimized condition was 0.41 dl/g and the yield was 93%. The incorporation of chiral units into the polymer backbone was obtained by measuring the specific rotation of polymer which show optical rotation and therefore is optically active ($[\alpha]_D^{25} = +18$). For that reason, this polymer has potential to be used as chiral stationary phase in HPLC for the separation of racemic mixtures. The resulting polymer is readily soluble in many organic solvents such as *N,N*′-dimethylacetamide (DMAc), *N*-methyl-2-pyrrolidone (NMP), DMSO and DMF. This optically active polymer is expected to be used as a biomaterial because of the presence of ester linkages and amino acids in its architecture.

3.2. Polymer characterization

The resulting polymer was characterized by FT-IR, ^{1}H-NMR spectroscopy techniques and elemental analyses. The FT-IR spectrum of PEI (Figure 3, curve c) exhibited characteristic absorptions of imide and ester groups around 1777 and 1722 cm^{-1}, which are related to carbonyls stretching of imide and ester groups, respectively. The peaks at 1382 and 727 cm^{-1} show the presence of the imide heterocy-

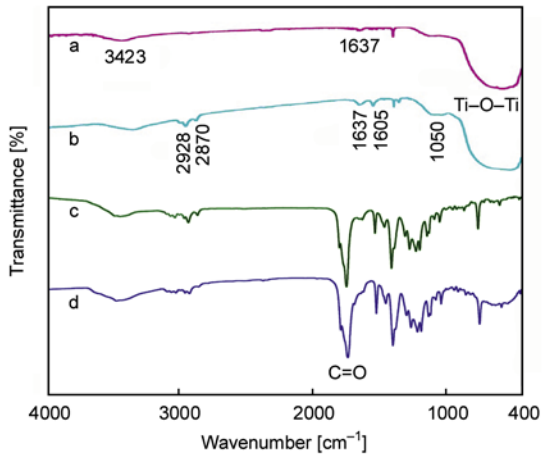

Figure 3. FT-IR spectra of (a) pure TiO_2 nanoparticles, (b) TiO_2 nanoparticles modified by KH550 (c) pure PEI (d) PEI/TiO_2 BNC (10 wt%)

cle in this polymer. The ^{1}H-NMR spectrum (500 MHz) of PEI is shown in Figure 4. In the ^{1}H-NMR spectrum of this polymer, the appearance of the methoxy protons (OCH_3) at 3.67 ppm as single peak indicates the presence of ester groups in the polymers side chain. The protons of the three chiral centers appeared at 5.31 ppm. The resonance of the diastereotopic hydrogens bonded to neighbor carbon of chiral centers appeared in the 2.58–2.63 and 3.00–3.54 ppm. The resonance of aromatic protons appeared in the range of 6.85–8.42 ppm. Elemental analysis values of the resulting polymer are also in good agreement with calculated values of carbon, hydrogen, nitrogen and sulfur in the polymer.

3.2.1. Preparation of PEI/TiO_2 BNCs

Nanoparticles have a strong tendency to agglomerate because of their high surface energy. To break down the nanoparticles agglomerates and improving the dispersivity of nanosized TiO_2 in polymer matrix, in this study, ultrasonic irradiation was employed to synthesize the BNC polymers. However, this approach will be restricted due to the limited interaction between the inorganic materials and the polymeric matrix, compared with the very strong interaction between individual nanoparticles. To attain proper dispersion of nanoparticles within polymer matrix and to yield a better compatibility between the nanoparticles and host polymeric materials, surface-modification is used for producing nanostructural composites.

The sonochemical reaction supplies appropriate reaction temperature to accelerate the hydrolysis of KH550. Furthermore, the microjets and shock waves created by intense ultrasonic waves in solution play a significant role in the combination of hydrolyzed KH550 and TiO_2 sol. In this condition, the collision chance of KH550 anchored onto the

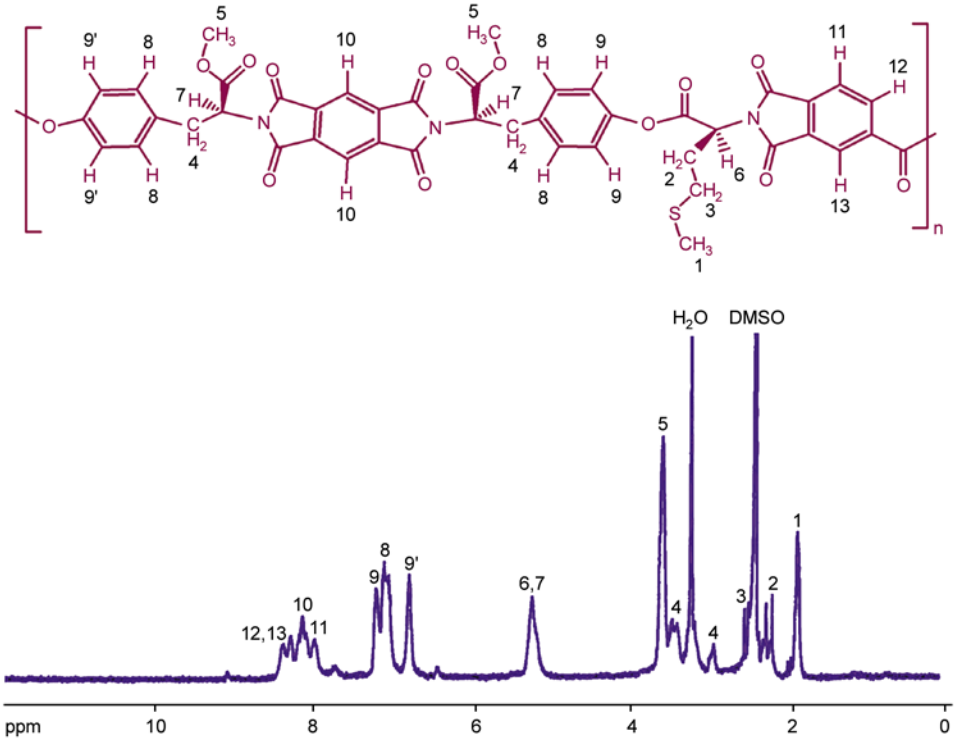

Figure 4. ^{1}H-NMR (500 MHz) spectrum of PEI in DMSO-d_6

surface of TiO_2 sol particles is greatly increased [34]. Silanol groups of KH550 generated by hydrolysis can interact with hydroxyl groups on the TiO_2 surface and form the modification layer with $–NH_2$ groups. Inasmuch the resulting PEI has lots of polar groups such as carbonyl, nitrogen and sulfur; the modified nanoparticles might be dispersed absolutely and will combine with PEI by different connections such as hydrogen bond, and also short-ranged steric and electrical interactions [35]. The details of the fabrication mechanism are displayed in Figure 2. Dispersion of nanoparticles in the polymer matrix can be observed from the photographs of TEM, FE-SEM and SEM.

3.2.2. Infrared study

FT-IR spectroscopy studies yielded useful qualitative information on the PEI/TiO_2 BNCs. Figure 3 shows the infrared spectra of pure TiO_2 nanoparticles (a), KH550-modified-TiO_2 (b), pure PEI (c) and PEI/TiO_2 BNC (10 wt%) (d). In the spectrum of pristine TiO_2, OH stretching band and bending band are observed at 3423 and 1637 cm^{-1}, respectively. The observed broader bands at 3500 and 3422 cm^{-1} were attributed to hydroxyl groups on different sites and some varying interactions between hydroxyl groups on TiO_2, respectively [31]. A broad absorption peak at 500–800 cm^{-1} is assigned to the Ti–O–Ti stretching band. As a result, the presence of KH550 on the surface of TiO_2 was confirmed by the characteristic peaks of CH stretching band at 2870–2928 cm^{-1} in the infrared data of KH550-modified-TiO_2 nanoparticles compared to the infrared data of pure TiO_2. The N–H bending vibration of primary amine is observed around 1605 cm^{-1}. In addition, the broad band around 1050 cm^{-1} corresponded to Si–O–Si bond is observed which indicates the condensation reaction between silanol groups. It is assumed that KH550 is adhering to the nano-TiO_2 particles possibly by coating. FT-IR spectrum of PEI/TiO_2 BNC (10 wt%) is shown in Figure 3d, where the characteristic peaks of pure PEI and TiO_2 are still maintained, it may be proved that the structure of PEI was affected by the presence of TiO_2.

FT-IR spectra of BNC polymers with different amounts of TiO_2 (5, 10, 15, 20, 25 wt%) nanoparticles (Figure 5) shows the intensity of Ti–O–Ti stretching band raise with an increase of TiO_2 nanoparticles content in PEI.

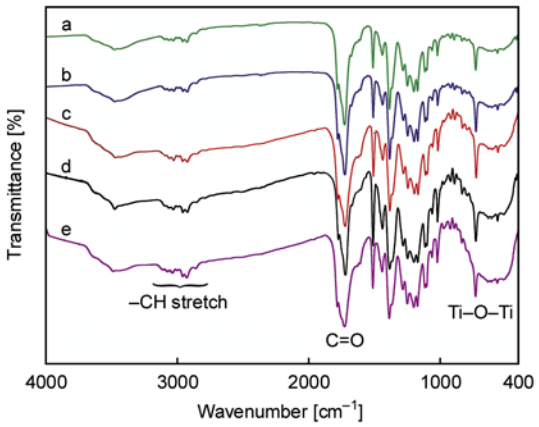

Figure 5. FT-IR spectra of (a) PEI/TiO_2 BNC (5 wt%), (b) PEI/TiO_2 BNC (10 wt%), (c) PEI/TiO_2 BNC (15 wt%), (d) PEI/TiO_2 BNC (20 wt%), (e) PEI/TiO_2 BNC (25 wt%)

3.2.3. X-ray diffraction data

XRD curves of PEI (a), pure TiO_2 (b), PEI/TiO_2 BNC (5 wt%) (c) and PEI/TiO_2 BNC (10 wt%) (d) are shown in Figure 6. The broad peak in the region of 2θ = 10–30° in XRD curve of PEI shows that PEI prepared in the absence of TiO_2 nanoparticles is amorphous. Figure 6 (b) shows anatase and rutile phase for pure TiO_2 nano particles. The XRD patterns of PEI/TiO_2 BNC (c) and (d) show characteristic peaks of anatase and rutile of TiO_2 indicating that the crystallinity form of TiO_2 nanoparticles has

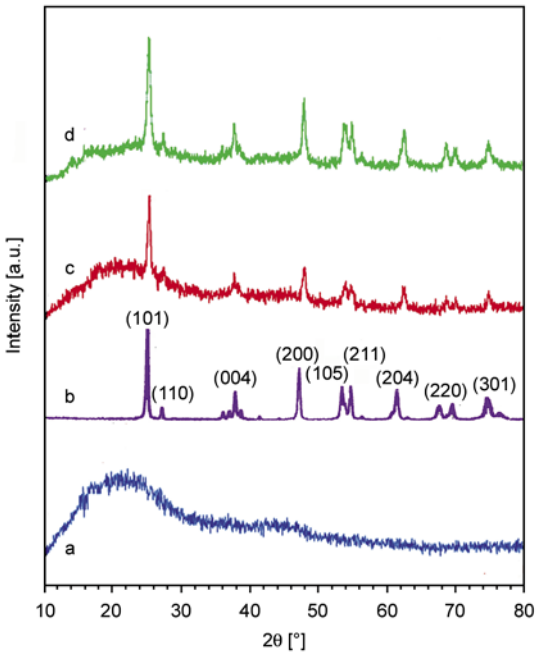

Figure 6. XRD curves of (a) PEI (b) pure TiO_2 nanoparticles (c) PEI/TiO_2 BNC (5 wt%), (d) PEI/TiO_2 BNC (10 wt%)

not been disturbed during the process. Also, the broad weak diffraction peak of PEI still exists, but its intensity decreases. It implies that the composite sample has a more ordered arrangement than the bare polymer owing to the TiO_2.

The average crystalline size of nano-TiO_2, which is determined from the half-width of the diffraction using the Debye–Scherrer equation, is approximately 20 nm for PEI/TiO_2 BNC (10 wt%) and 16 nm for PEI/TiO_2 BNC (5 wt%). Sherrer's Equation (1) is as follows:

$$D = \frac{0.9\lambda}{\beta\cos\theta} \quad (1)$$

where D is the crystallite size, λ is wavelength of the radiation, θ is the Bragg's angle and β is the full width at half maximum [36].

3.2.4. Morphology observation

SEM micrograph (Figure 7) of the PEI containing no TiO_2 nanoparticles is shown in Figure 7a. It has a surface with no evidence of surface topography observed at the magnification used during SEM observations. Representative SEM images of PEI/TiO_2 BNC (5 wt%) (b, c) and PEI/TiO_2 BNC (10 wt%) (d) as well as FE-SEM pictures of PEI/TiO_2 BNC (10 wt%) are exhibited in Figure 8 and presented a homogeneous microstructure and con-

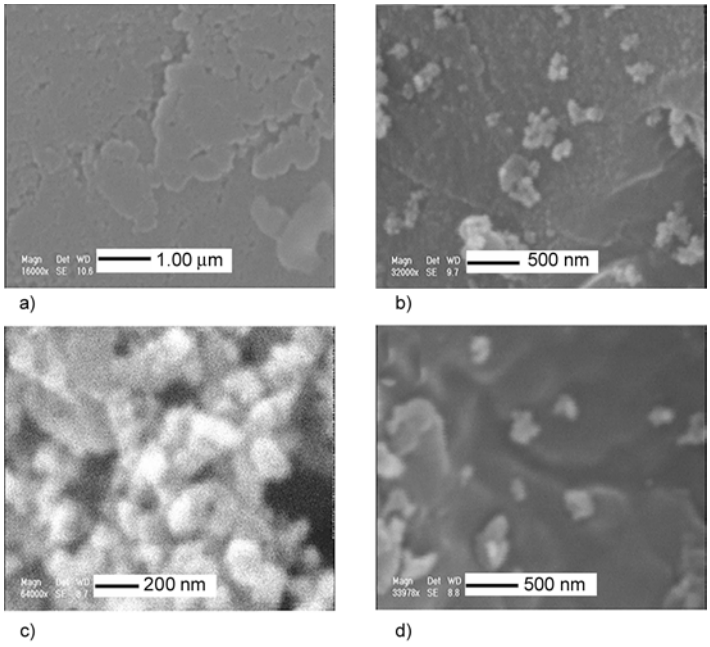

Figure 7. SEM micrographs of pure PEI (a), PEI/TiO_2 BNC (5 wt%) (b, c), PEI/TiO_2 BNC (10 wt%) (d)

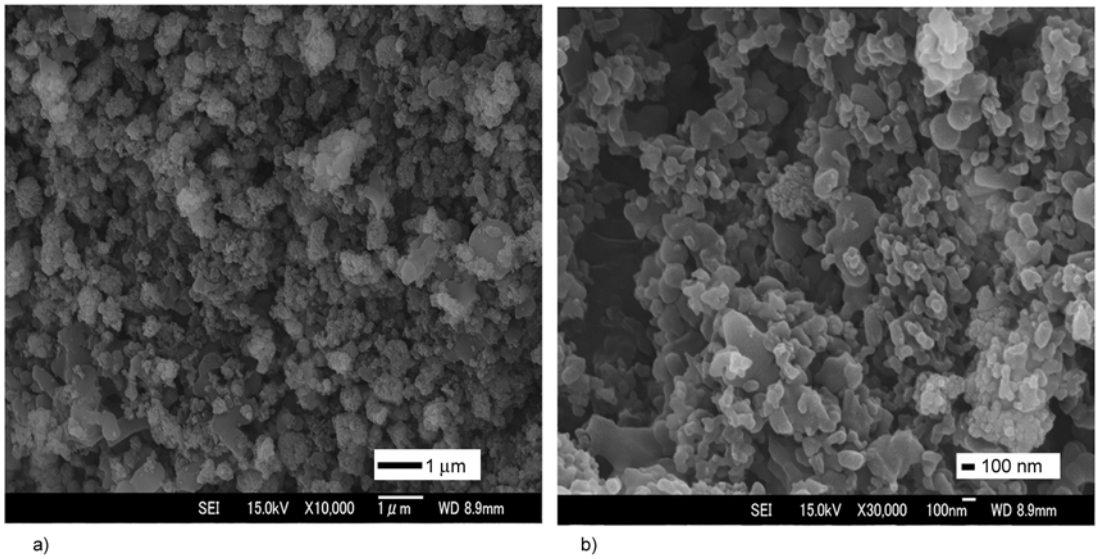

Figure 8. FE-SEM micrographs of PEI/TiO_2 BNC (10 wt%)

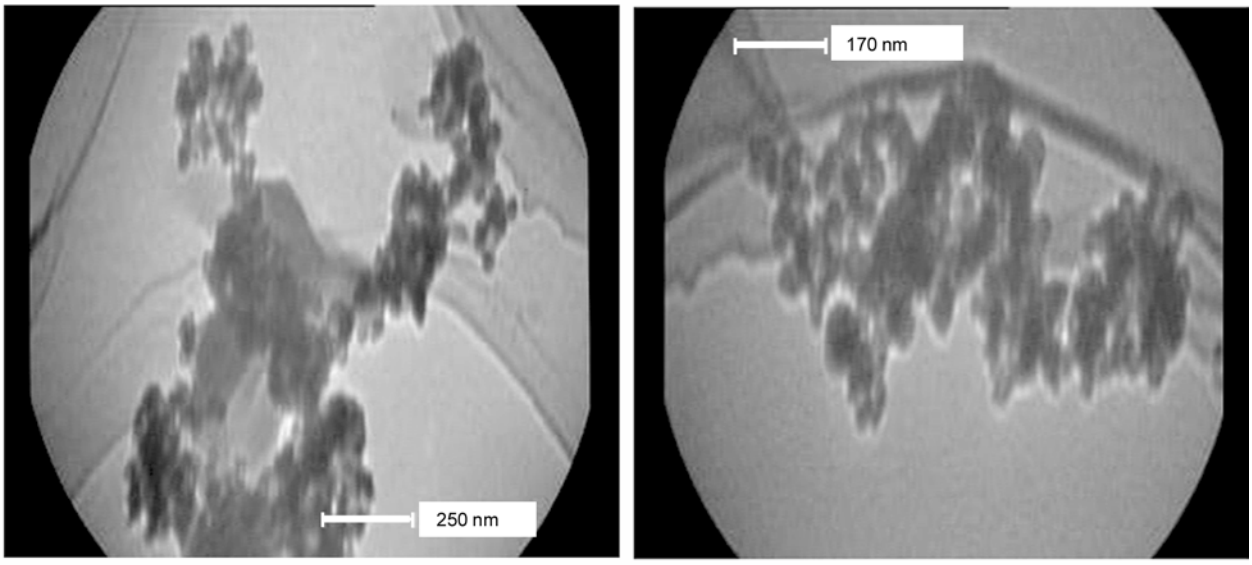

Figure 9. TEM micrographs of PEI/TiO_2 BNC (5 wt%)

firmed that the TiO_2 nanoparticles appear on the PEI surface in nanoscale comparing with surface of pure PEI.

Figure 9 shows the morphology of PEI/TiO_2 BNC (5 wt%) as obtained by TEM micrographs which demonstrated some distinctive domains and dispersion of TiO_2 nanoparticles (about 50 nm) in the PEI matrix.

3.3. Thermal properties

Thermogravimetric analysis was applied to evaluate the thermal properties of the PEI and PEI/TiO_2 BNCs at a heating rate of 10ºC/min, under a nitrogen atmosphere. Figure 10 demonstrates the respective TGA profiles and the corresponding thermoanalysis data, including the temperatures at which 5% (T_5) and 10% (T_{10}) degradation occur. Char yield at 800ºC and also limiting oxygen index (LOI) based on Van Krevelen and Hoftyzer equation (Equation (2)) are summarized in Table 1 [37]:

$$LOI = 17.5 + 0.4\ CR \quad (2)$$

where CR = char yield.

From these data it is clear that the PEI is stable to 300ºC and introduction of inorganic nanoparticles in polymer matrix induced the thermal properties to rise. However, the initial temperature of the bionanocomposites weight loss was not increased considerably with increasing TiO_2 content until at a weight loss of 40%. Increasing in the thermal stabil-

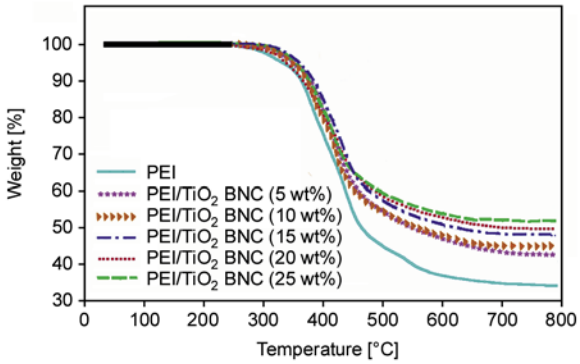

Figure 10. TGA thermograms of PEI and PEI/TiO_2 BNCs under a nitrogen atmosphere at heating rate of 10°C/min

Table 1. Thermal properties of the PEI and PEI/TiO_2 BNCs

Samples	T_5 [°C][a]	T_{10} [°C][b]	Char Yield [%][c]	LOI[d]
PEI	328	360	34	31.1
PEI/TiO_2 BNC (5 wt%)	346	370	43	34.7
PEI/TiO_2 BNC (10 wt%)	347	368	45	35.5
PEI/TiO_2 BNC (15 wt%)	355	378	48	36.7
PEI/TiO_2 BNC (20 wt%)	337	363	49	37.1

[a]Temperature at which 5% weight loss was recorded by TGA at heating rate of 10°C/min under a nitrogen atmosphere.
[b]Temperature at which 10% weight loss was recorded by TGA at heating rate of 10°C/min under a nitrogen atmosphere.
[c]weight percentage of material left undecomposed after TGA analysis at a temperature of 800°C under a nitrogen atmosphere.
[d]Limiting oxygen index (LOI) evaluating char yield at 800°C.

ity may happen as an effect of the high thermal stability of TiO_2 network and the physical crosslink points of the TiO_2 particles, which may restrict the movement of the molecular chain of PEI. Subsequent to addition of TiO_2 nanoparticles with high melting point to the polymer matrix, the TiO_2 particles can serve as a good thermal cover layer, avoiding the direct thermal decomposition of polymer matrix by heat. Also, TiO_2 nanoparticles offer a larger surface area and enhance the effect of thermal cover [38, 30]. The char yield of pure PEI at 800ºC is 34%, whilst those of the bionanocomposites (PEI/TiO_2 BNC 5, 10, 15, 20, 25 wt%) at 800ºC are in the range of 43–52%, and this increases with an increase of TiO_2 nanoparticles content in the PEI. On the basis of LOI values (34–38), all macromolecules can be classified as self-extinguishing BNC polymers.

3.4. Soil burial study

The enzymatic biodegradation of a polymer depends on the microbial populations, the pH-value, temperature, moisture, low glass temperature (high mobility), and low crystallinity. Therefore higher microbial population could be correlated to higher biodegradation. A lower colonial growth of bacteria and fungi was observed from water extract of soil containing PEI/TiO_2 BNC (10 wt%) compared with PEI (Figures 11 and 12). This result may indicate that degradation of PEI should be faster than PEI/TiO_2 BNC (10 wt%) because the former is more attacked by microorganisms. This was confirmed by higher colony count of bacteria and fungi on the media of PEI water extract compared with control soil and soil containing toxic BPA (Table 2). Evidently, this may suggest slight antimicrobial activity of PEI/TiO_2 BNC buried in the soil. Some other experiments also showed that the antimicrobial activity of the nano-TiO_2 composites increases with increasing concentration [39] and higher antimicrobial behavior will reduce biodegradation of the polymer in the soil. It may be recommended that for synthesis of biocompatible polymers, low concentration of TiO_2 must be used.

3.5. Wheat growth bioassay

The total dry matter provides the best indication of an adverse plant response to toxic substances and it

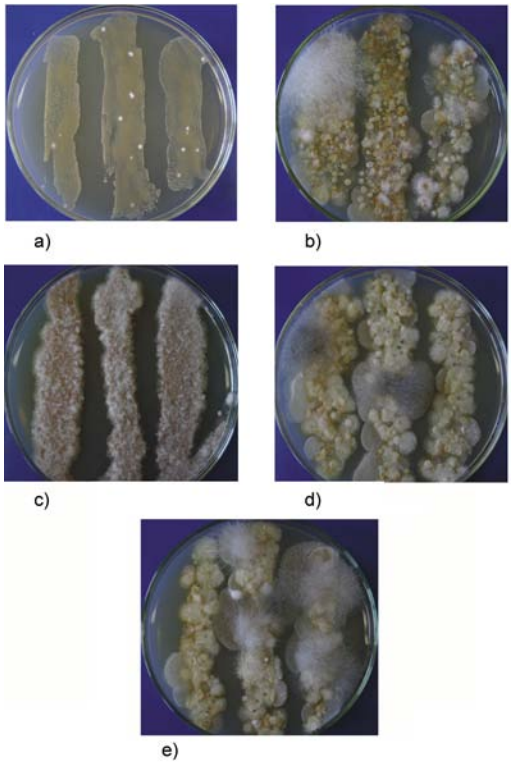

Figure 11. Fungal colonies grown from water extract of the soil containing diacid (c), PEI (d) and PEI/TiO_2 BNC (10 wt%) (e) compared with BPA (a) and control soil (b) on PDA Petri plates

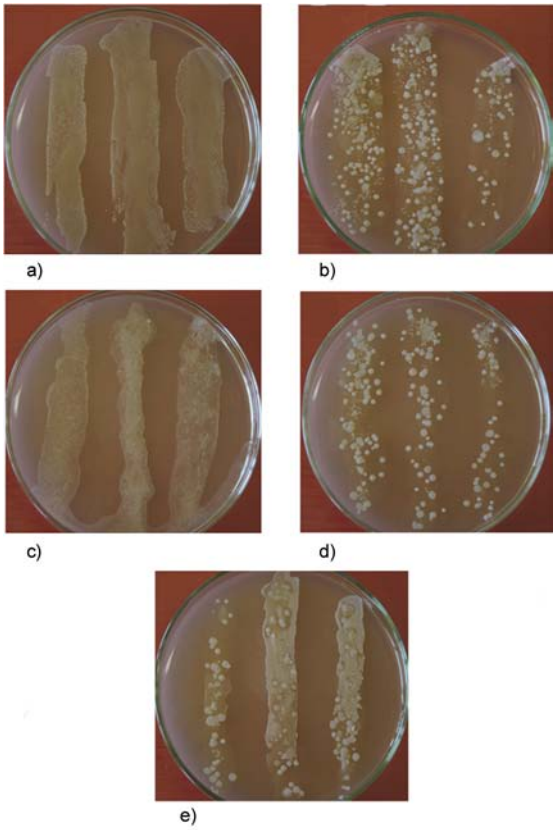

Figure 12. Bacterial colonies grown from water extract of the soil containing diacid (c), PEI (d) and PEI/TiO_2 BNC (10 wt%) (e) compared with BPA (a) and control soil (b) on PDA Petri

Table 2. The number of bacterial and fungal colonies (CFUs) from water extract of soil containing diacid, PEI and PEI/TiO_2 BNC grown on PDA Petri plates compared with control treatments

Compound	Fungal colony forming units (CFUs) [n/100 µl]	Bacterial colony forming units (CFUs) [n/100 µl]
Diacid	193±14.0	0±0
PEI	49±2.5	102±6.6
PEI/TiO_2 BNC (10 wt%)	30±2.5	54±12.5
BPA	2±1.5	0±0
Negative control (soil)	30±2.5	88±28.5

Table 3. Effect of diacid (b), PEI (c) and PEI/TiO_2 BNC (10 wt%) (d) compared with control soil (a) on wheat seedlings height [mm] and seedling dry weight [mg]

Material	Control soil (a)	Diacid (b)	PEI (c)	PEI/TiO_2 BNC (10 %wt) (d)
Seedling height [mm]	188.0	176.0	192.0	162.0
Seedling weight [mg]	23.5	13.5	16.2	14.2

Figure 13. Effect of diacid (b), PEI (c) and PEI/TiO_2 BNC (10 wt%) (d) compared with control soil (a) on survival and growth of wheat seedlings

has been found that wheat is sensitive plant to toxicity of organic wastes in plant growth bioassays. The application of PEI/TiO_2 BNC (10 wt%) in the soil did not present significant negative effects on total dry matter production compared with PEI (Figure 13). However, compared to the control (Table 3), both compounds reduced total dry matter, and shoot length probably due to lower availability of nutritional elements. These results show that both PEI and PEI/TiO_2 BNC (10 wt%) probably have no toxicity for plant growth and are highly compatible with natural ecosystems providing low concentration of TiO_2 in polymer structure.

4. Conclusions

In summary, a new thermally stable and optically active PEI was synthesized by direct step-growth polycondensation of *N,N′*-(pyromellitoyl)-bis-(L-tyrosine dimethyl ester) as an optically active aromatic diol with *N*-trimellitylimido-L-methionine using TsCl/DMF/Py as a condensing agent. Ultrasonic process was applied as a profitable route for the modification of TiO_2 nanoparticles with KH550 followed by synthesis of the PEI/TiO_2 BNCs. TEM analysis showed dispersion of TiO_2 with average particle sizes about 50 nm in the polymer matrix. Also, morphological study of synthesized BNCs exhibited the TiO_2 nanoparticles mostly dispersed homogeneously on the polymer matrix by FE-SEM analysis. According to the LOI values, obtained BNC polymers can be categorized as self-extinguishing materials. FT-IR and XRD data also established that TiO_2 nanoparticles exist in the PEI matrix. The presence of natural amino acids in the PEI combined with bioactive TiO_2 nanoparticles made these BNC polymers capable to be potentially bioactive. To ensure real bioactivity and safe incorporation of these materials in the geochemical life cycle, in vitro soil burial and plant bioassay tests were performed. The results illustrated that synthesized polymers could be probably decomposed by soil microorganisms; however, the addition of TiO_2 resulted in a decrease in the microbial population due to its antimicrobial activity, and high biodegradability of PEI/TiO_2 BNC depends on low concentration of incorporated titanium dioxide.

Acknowledgements

We wish to express our gratitude to the Research Affairs Division Isfahan University of Technology (IUT), Isfahan, for partial financial support. Further financial support from Iran nanotechnology Initiative Council (INIC), National Elite Foundation (NEF) and Center of Excellency in Sensors and Green Chemistry Research (IUT) are gratefully acknowledged. We also extend our thanks to Dr. A. Ashrafi for his valuable discussion.

References

[1] Chivrac F., Pollet E., Avérous L.: Progress in nano-biocomposites based on polysaccharides and nanoclays. Materials Science and Engineering R: Reports, **67**, 1–17 (2009).
DOI: 10.1016/j.mser.2009.09.002

[2] Kumar P., Sandeep K. P., Alavi S., Truong V. D., Gorga R. E.: Preparation and characterization of bionanocomposite films based on soy protein isolate and montmorillonite using melt extrusion. Journal of Food Engineering, **100**, 480–489 (2010).
DOI: 10.1016/j.jfoodeng.2010.04.035

[3] Guan C., Lü C-L., Liu Y-F., Yang B.: Preparation and characterization of high refractive index thin films of TiO_2/epoxy resin nanocomposites. Journal of Applied Polymer Science, **102**, 1631–1636 (2006).
DOI: 10.1002/app.23947

[4] Mallakpour S., Tirgir F., Sabzalian M. R.: Synthesis, characterization and in vitro antimicrobial and biodegradability study of pseudo-poly(amino acid)s derived from *N*,*N*′-(pyromellitoyl)-*bis*-l-tyrosine dimethyl ester as a chiral bioactive diphenolic monomer. Amino Acids, **40**, 611–621 (2011).
DOI: 10.1007/s00726-010-0686-0

[5] Tingaut P., Zimmermann T., Lopez-Suevos F.: Synthesis and characterization of bionanocomposites with tunable properties from poly(lactic acid) and acetylated microfibrillated cellulose. Biomacromolecules, **11**, 455–464 (2010).
DOI: 10.1021/bm901186u

[6] Bourgeat-Lami E., Espiard Ph., Guyot A.: Poly(ethyl acrylate) latexes encapsulating nanoparticles of silica: 1. Functionalization and dispersion of silica. Polymer, **36**, 4385–4389 (1995).
DOI: 10.1016/0032-3861(95)96843-W

[7] Ratna D., Divekar S., Samui A. B., Chakraborty B. C., Banthia A. K.: Poly(ethylene oxide)/clay nanocomposite: Thermomechanical properties and morphology. Polymer, **47**, 4068–4074 (2006).
DOI: 10.1016/j.polymer.2006.02.040

[8] Siengchin S., Karger-Kocsis J., Apostolov A. A., Thomann R.: Polystyrene–fluorohectorite nanocomposites prepared by melt mixing with and without latex precompounding: Structure and mechanical properties. Journal of Applied Polymer Science, **106**, 248–254 (2007).
DOI: 10.1002/app.26474

[9] Wang Q., Xia H., Zhang C.: Preparation of polymer/inorganic nanoparticles composites through ultrasonic irradiation. Journal of Applied Polymer Science, **80**, 1478–1488 (2001).
DOI: 10.1002/app.1239

[10] Xu X., Li B., Lu H., Zhang Z., Wang H.: The interface structure of nano-SiO_2/PA66 composites and its influence on material's mechanical and thermal properties. Applied Surface Science, **254**, 1456–1462 (2007).
DOI: 10.1016/j.apsusc.2007.07.014

[11] Suslick K. S., Hammerton D. A., Cline R. E.: Sonochemical hot spot. Journal of the American Chemical Society, **108**, 5641–5642 (1986).
DOI: 10.1021/ja00278a055

[12] Yu J., Zhou M., Cheng B., Yu H., Zhao X.: Ultrasonic preparation of mesoporous titanium dioxide nanocrystalline photocatalysts and evaluation of photocatalytic activity. Journal of Molecular Catalysis A: Chemical, **227**, 75–80 (2005).
DOI: 10.1016/j.molcata.2004.10.012

[13] Yu J. C., Yu J., Zhang L., Ho W.: Enhancing effects of water content and ultrasonic irradiation on the photocatalytic activity of nano-sized TiO_2 powders. Journal of Photochemistry and Photobiology A: Chemistry, **148**, 263–271 (2002).
DOI: 10.1016/S1010-6030(02)00052-7

[14] Samal S. S., Jeyaraman P., Vishwakarma V.: Sonochemical coating of Ag-TiO_2 nanoparticles on textile fabrics for stain repellency and self-cleaning- The Indian scenario: A review. Journal of Minerals and Materials Characterization and Engineering, **9**, 519–525 (2010).

[15] Chen J-H., Dai C-A., Chen H-J., Chien P-C., Chiu W-Y.: Synthesis of nano-sized TiO_2/poly(AA-*co*-MMA) composites by heterocoagulation and blending with PET. Journal of Colloid and Interface Science, **308**, 81–92 (2007).
DOI: 10.1016/j.jcis.2006.12.066

[16] Olshavsky M. A., Allcock H. R.: Polyphosphazenes with high refractive indices: Synthesis, characterization, and optical properties. Macromolecules, **28**, 6188–6197 (1995).
DOI: 10.1021/ma00122a028

[17] Beecroft L. L., Ober C. K.: Nanocomposite materials for optical applications. Chemistry of Materials, **9**, 1302–1317 (1997).
DOI: 10.1021/cm960441a

[18] Papadimitrakopoulos F., Wisniecki P., Bhagwagar D. E.: Mechanically attrited silicon for high refractive index nanocomposites. Chemistry of Materials, **9**, 2928–2933 (1997).
DOI: 10.1021/cm970278z

[19] Yoshida M., Prasad P. N.: Sol−gel-processed SiO_2/TiO_2/poly(vinylpyrrolidone) composite materials for optical waveguides. Chemistry of Materials, **8**, 235–241 (1996).
DOI: 10.1021/cm950331o

[20] Kran R. K., Srivasatava O. N.: On the synthesis of nanostructured TiO_2 anatase phase and the development of the photoelectrochemical solar cell. International Journal of Hydrogen Energy, **24**, 27–35 (1999). DOI: 10.1016/S0360-3199(98)00009-3

[21] Park H., Choi W.: Effects of TiO_2 surface fluorination on photocatalytic reactions and photoelectrochemical behaviors. Journal of Physical Chemistry B, **108**, 4086–4093 (2004). DOI: 10.1021/jp036735i

[22] Yu J., Xiang Q., Zhou M.: Preparation, characterization and visible-light-driven photocatalytic activity of Fe-doped titania nanorods and first-principles study for electronic structures. Applied Catalysis B: Environmental, **90**, 595–602 (2009). DOI: 10.1016/j.apcatb.2009.04.021

[23] Liu S., Yu J., Jaroniec M.: Tunable photocatalytic selectivity of hollow TiO_2 microspheres composed of anatase polyhedra with exposed {001} facets. Journal of the American Chemical Society, **132**, 11914–11916 (2010). DOI: 10.1021/ja105283s

[24] Minero C., Mariella G., Maurino V., Pelizzetti E.: Photocatalytic transformation of organic compounds in the presence of inorganic anions. 1. Hydroxyl-mediated and direct electron-transfer reactions of phenol on a titanium dioxide−fluoride system. Langmuir, **16**, 2632–2641 (2000). DOI: 10.1021/la9903301

[25] Li C-H., Chen C-C., Chen K-M.: Studies on the synthesis and properties of copolyesterimide. Journal of Applied Polymer Science, **52**, 1751–1757 (1994). DOI: 10.1002/app.1994.070521209

[26] Hsu T-F., Lin Y-C., Lee Y-D.: Synthesis and characterization of novel thermotropic liquid crystalline copoly (ester imide)s. Journal of Polymer Science Part A: Polymer Chemistry, **36**, 1791–1803 (1998). DOI: 10.1002/(SICI)1099-0518(199808)36:11<1791::AID-POLA13>3.0.CO;2-9

[27] Iannelli M., Alupei V., Ritter H.: Selective microwave-accelerated synthesis and polymerization of chiral methacrylamide directly from methacrylic acid and (*R*)-1-phenyl-ethylamine. Tetrahedron, **61**, 1509–1515 (2005). DOI: 10.1016/j.tet.2004.11.068

[28] Mallakpour S., Kolahdoozan M.: Preparation of new poly(amide–imide)s with chiral architectures via direct polyamidation reaction. Journal of Applied Polymer Science, **104**, 1248–1254 (2007). DOI: 10.1002/app.25747

[29] Mallakpour S., Tirgir F., Sabzalian M. R.: Synthesis and structural characterization of novel biologically active and thermally stable poly(ester-imide)s containing different natural amino acids linkages. Journal of Polymer Research, **18**, 373–384 (2011). DOI: 10.1007/s10965-010-9427-z

[30] Chen J., Zhou Y., Nan Q., Ye X., Sun Y., Zhang F., Wang Z.: Preparation and properties of optically active polyurethane/TiO_2 nanocomposites derived from optically pure 1,1′-binaphthyl. European Polymer Journal, **43**, 4151–4159 (2007). DOI: 10.1016/j.eurpolymj.2007.07.006

[31] Chen J., Zhou Y., Nan Q., Sun Y., Ye X., Wang Zh.: Synthesis, characterization and infrared emissivity study of polyurethane/TiO_2 nanocomposites. Applied Surface Science, **253**, 9154–9158 (2007). DOI: 10.1016/j.apsusc.2007.05.046

[32] Higashi F., Ong C-H., Okada Y.: High-molecular-weight copolyesters of dihydroxybenzophenones by 'induced' copolyesterification using TsCl/DMF/Py as a condensing agent. Journal of Polymer Science Part A: Polymer Chemistry, **37**, 3625–3631 (1999). DOI: 10.1002/(SICI)1099-0518(19990915)37:18<3625::AID-POLA10>3.0.CO;2-V

[33] Higashi F., Akiyama N., Takahashi I., Koyama T.: Direct polycondensation of aromatic dicarboxylic acids and bisphenols with tosyl chloride and *N*,*N*-dimethylformamide in pyridine. Journal of Polymer Science: Polymer Chemistry Edition, **22**, 1653–1660 (1984). DOI: 10.1002/pol.1984.170220712

[34] Yao Q., Zhou Y., Sun Y., Ye X.: Synthesis of TiO_2 hybrid molecular imprinted polymer for ethofumesate linked by silane coupling agent. Journal of Inorganic and Organometallic Polymers, **18**, 477–484 (2008). DOI: 10.1007/s10904-008-9227-7

[35] Mallakpour S., Soltanian S.: Studies on syntheses and morphology characteristic of chiral novel poly(ester-imide)/TiO_2 bionanocomposites derived from l-phenylalanine based diacid. Polymer, **51**, 5369–5376 (2010). DOI: 10.1016/j.polymer.2010.09.063

[36] Nakayama N., Hayashi T.: Preparation and characterization of poly(L-lactic acid)/TiO_2 nanoparticle nanocomposite films with high transparency and efficient photodegradability. Polymer Degradation and Stability, **92**, 1255–1264 (2007). DOI: 10.1016/j.polymdegradstab.2007.03.026

[37] Van Krevelen D. W., Hoftyzer P. J.: Properties of polymers. Elsevier, Amsterdam (1976).

[38] Fujimura K., Miyake A.: The effect of specific surface area of TiO_2 on the thermal decomposition of ammonium perchlorate. Journal of Thermal Analysis and Calorimetry, **99**, 27–31 (2010). DOI: 10.1007/s10973-009-0462-0

[39] Chen Y., Yan L., Wang R., Fan H., Zhang Q.: Antimicrobial polyurethane synthetic leather coating with *in-situ* generated Nano-TiO_2. Fibers and Polymers, **11**, 689–694 (2010). DOI: 10.1007/s12221-010-0689-1